eXPRESS Polymer Letters Vol.1, No.2 (2007) 59
Available online at www.expresspolymlett.com
DOI: 10.3144/expresspolymlett.2007.11

Editorial corner – a personal view

Trends in fiber reinforcements – the future belongs to basalt fiber

T. Czigány[*]

Department of Polymer Engineering, Budapest University of Technology and Economics, Műegyetem rkp. 3., H-1111 Budapest, Hungary

Technical advances are very fast in the field of plastics – this is especially true for fiber reinforced composites. Nowadays the typical reinforcement of polymer composites is glass fiber, which exhibits good mechanical properties, high strength, and a relatively low price. In more demanding applications, in order to meet special requirements carbon fiber reinforcement is used but its production is much more expensive. Hybridization of these two fibers is a frequently used solution, which combines the advantages of both fibers (e.g. in the manufacture of wind turbine blades). Due to the ever stricter environmental regulations natural fibers (e.g. flax, hemp, sisal, wood) become more and more popular. These fibers combine acceptable strength with relatively low price and biodegradability.

Taking into account the sharp competition and the growing economic and environmental expectations with respect to the reinforcements used in plastic structures, newer potential reinforcements are studied for applicability in the leading laboratories of the world. Such a new, possible reinforcement is, among others the basalt fiber, made from a volcanic rock found on the surface of the Earth's crust (containing 40–60% SiO_2), and these fibers exhibit a series of excellent properties. In addition to their high modulus and excellent heat resistance, the heat and sound insulating properties and the vibration dampening properties of these fibers are extremely good. Biological stability and chemical resistance are further bonuses. Basalt fibers are typically produced by two technologies. The so-called Junkers technology with centrifugal cylinders is used for manufacturing cheap fibers with 60–100 mm length and 8–10 μm thickness, primarily used as insulating materials in the construction and automotive industries.

For more demanding applications continuous fibers, which can be weaved and spun by textile technologies, are prepared by fiber spinning technologies from the melt – similarly to traditional glass fiber production. These continuous fibers of 10–12 μm diameter can be obtained in the form of rovings containing different numbers of elementary fibers, which exhibit somewhat better strength than glass fibers, but their price is presently 10–20% higher. The application of these very high quality fibers has already been started in both thermoplastic and thermoset matrix composites. Therefore, it can be predicted that basalt fibers may become a future alternative for skin irritating glass fibers and for asbestos fibers already banned because of their carcinogenic properties, not only owing to their excellent properties but also as a result of their continuously dwindling price.

Prof. Dr. T. Czigány
Editor

---

[*]Corresponding author, e-mail: czigany@eik.bme.hu

eXPRESS Polymer Letters Vol.1, No.2 (2007) 60–68
Available online at www.expresspolymlett.com
DOI: 10.3144/expresspolymlett.2007.12

Melting and crystallization of in-situ polymerized cyclic butylene terephthalates with and without organoclay: a modulated DSC study

J. Karger-Kocsis[1]*, *P. P. Shang*[2] , *Z. A. Mohd Ishak*[3], *M. Rösch*[4]

[1]Institut für Verbundwerkstoffe GmbH, Kaiserslautern University of Technology, D-67663 Kaiserslautern, Germany
[2]Eastman Chemical Co., Research Laboratories, PO Box 1972 Kingsport, Tennessee 37662-5150, USA
[3]School of Materials and Mineral Resources Engineering, Engineering Campus, Universiti Sains Malaysia, 14300 Nibong Tebal, Penang, Malaysia
[4]Cyclics Europe GmbH, Naundorfer Str., D-01987 Schwarzheide, Germany

Received 4 November 2006; accepted in revised form 4 January 2007

Abstract. The polymerization of cyclic butylene terephthalate oligomers (CBT) were studied in presence (in 5 wt.%) and absence of an organoclay (Cloisite® 30B) by modulated DSC (MDSC). The organoclay containing samples were produced by dry and melt blending, respectively. The first heating, causing the polymerization of the CBT catalyzed by an organotin compound, was followed by cooling prior to the second heating. The MDSC scans covered the temperature interval between 0 and 260°C. The aim of this protocol was to study the crystallization and melting behavior of the resulting polybutylene terephthalate (pCBT) and its organoclay modified nanocomposites. It was found that the thermal behaviors of the polymerizing and polymerized CBT (pCBT) were strongly affected by the sample preparation. The organoclay suppressed the crystallization of the pCBT produced during the first heating. However, results from the second heating suggest that more perfect crystallites were formed in the organoclay modified pCBT variants. The organoclay also affected the conversion and mean molecular mass of the resulting pCBT which were slightly lower than those of the plain pCBT polymerized under identical conditions.

Keywords: *thermal properties, crystallization and melting, cyclic butylene terephthalate (CBT), modulated DSC, organoclay*

---

1. Introduction

Cyclic butylene terephthalate (CBT) oligomers are now available commercially. The related CBT products of Cyclics (Schenectady, N.Y., USA – www.cyclics.com), when molten and catalyzed, polymerize into linear poly(butylene terephthalate) (PBT). The polymerization time can be set in a broad time interval by suitable catalysts ([1] and references therein). Prior to polymerization the melt viscosity of the CBT (melting temperature >140°C) may be as low as 20 mPas [2–3]. This is a great advantage for liquid composite molding operations where the reinforcement has to be infiltrated, wet-out accordingly (e.g. [4–5]). A further benefit of CBT is that the polymerization can be performed also below the melting temperature of PBT (= 225°C). The industry prefers the isothermal polymerization of CBT at $T = 190°C$. Here the polymerization is followed by the crystallization due to which the solidified product can be removed from the tool without cooling the latter. It is often quoted among further benefits with CBT that its polymerization is athermic (e.g. [1]). In our recent

---

*Corresponding author, e-mail: karger@ivw.uni-kl.de work, adopting the technique of modulated differential scanning calorimetry (MDSC), we have concluded that the athermic feature (thermoneutral) is due to the fact that the exothermic polymerization heat is compensated by the endothermic melting of the various CBT oligomers [6]. However, this interpretation may be wrong. Note that when writing the Gibb's law for the polymerization, i.e. $\Delta G = \Delta H - T\Delta S$, the change in the free energy (ΔG) should be negative. The change in the polymerization enthalpy (ΔH) is marginal as both initial oligomers and resulting polymer chains have the same chemical bonds. On the other hand, the linear chains possess a far greater conformational freedom than the constrained CBT cycles initially. So, the large increment in the entropy term (ΔS) is the driving force for the polymerization - which is thus athermic. As a consequence, it is straightforward to use the term 'entropically driven polymerization' for that of the CBT oligomers.

Nowadays, substantial effort are undertaken to produce polymeric nanocomposites using organophilic modified clays. This development is fuelled by drastic property improvements (e.g. stiffness, strength, heat deflection temperature, barrier properties, flame resistance) which can be achieved even at low organoclay content [7]. PBT-based organoclay containing nanocomposites have already been produced by melt blending and in-situ polymerization (e.g. cited works in Ref. [7]). Few reports are even available in the open literature on the polymerization of CBT or similar cyclic polyesters in presence of organoclays [8–9]. Further information about the feasibility of this approach can be taken from the patent literature (e.g. [10]). On the other hand, the thermal behaviors of the polymerizing and polymerized CBT in presence of organoclays have not been studied by the MDSC technique. So, the aim of the present paper was to study the polymerization, crystallization and melting behaviors of CBT and its polymers (denoted further on as pCBT) in presence of a suitable organoclay using the MDSC technique.

2. Experimental

The CBT used was a one-component ready-to-polymerize grade, viz. XB3-CA4 of Cyclics. It contained as catalyst butyltin chloride dihydroxide. As organoclay a methyl-tallow-bis(2-hydroxyethyl) quaternary ammonium salt modified montmorillonite (Cloisite® 30 B), supplied by Southern Clay Inc. (Gonzalez, TX, USA) was selected. The interlayer spacing of this organoclay was 1.8 nm according to X-ray diffraction results. It is noteworthy that this kind of organoclay was the preferred one in the cited patent [10]. MDSC tests were run on the following CBT and pCBT samples:

- neat CBT (designated as CBT)
- CBT dry blended with 5 wt.% organoclay (designated as CBT + organoclay-dry blend),
- CBT powder melt blended with 5 wt.% organoclay (CBT + organoclay-melt blend), and
- pCBT containing 5 wt.% organoclay after polymerization at $T = 190°C$ for 30 min (designated as pCBT + organoclay)

It has to be emphasized here that CBT has been polymerized to poly(butylene terephthalate), termed as pCBT in this paper, during the first heating run. The reason behind the above 'sampling' was to explore to what extent the structure-property relationships of the pCBT nanocomposites may be affected by the preparation techniques. Note that premixing of nanoparticles with CBT melt appears as a very promising route as the catalyst in the so-called two-component CBT grades can be added separately in a further step.

The melt blended version was produced by mixing the organoclay in the molten CBT ($T = 160°C$) for 5 min prior to quenching the compound to room temperature (*RT*). The resulting materials were powdered in a mortar. Note that the organoclay containing CBT 'dry blend' was 'homogenized' also in the mortar. The organoclay modified pCBT (referred as pCBT + organoclay) was prepared by mixing the organoclay in the CBT melt at $T = 160°C$ for 5 min before polymerizing in an open poly(tetrafluoro ethylene) mold at $T = 190°C$ for 30 min. It was established before that the latter conditions produce fully polymerized pCBT. It is noteworthy that both organoclay and CBT were dried prior to use (at $T = 80°C$ overnight).

MDSC investigations were performed on a TA Instruments-Waters LLC Thermal Advantage for Q-Series equipped with a Q1000 auto-MDSC, connected to a liquid nitrogen cooling system. Scans were recorded from 0 to 260°C. The samples (ca. 6–8 mg) were held at the upper threshold temperature for 5 min. This was followed by cooling and then by a second heating. Both cooling and second heating were performed under the same MDSC conditions as the first heating. The following scanning parameters were set: heating rate of 5°C/min with a modulation of ± 0.531°C/min and a frequency of 40 s under helium flow. The data were analyzed by the Universal Analysis 2000 software package of TA Instruments, Version 4.1D. It has to be emphasized that no efforts were made to study the effects of modulation amplitude, modulation period and heating rate although they may influence the MDSC response markedly.

3. Results and discussion

3.1. CBT (without organoclay)

The MDSC traces registered in the first heating, subsequent cooling and second heating for the (p)CBT are displayed in Figures 1a to c. The order of the deconvoluted MDSC traces from the top to the bottom of all figures is: reversing (R), conventional (C) and non-reversing (NR). Note that the trace C is that one which can be monitored during a conventional DSC measurement. In the NR trace of Figure 1a a broad exothermic peak (T = 100… 150°C) is resolved (enthalpy = 21.5 J/g). This peak is likely due to recrystallization phenomena between the various oligomers (dimer, trimer, tetramer etc.) as quoted later. Note that this peak is superimposed to that of the CBT melting based on the related R and C traces (cf. Figure 1a). The next feature of the NR trace is a small endothermic peak at T = 156°C (enthalpy = 1.4 J/g) that may be linked with the polymerization of CBT to pCBT. In the R and NR traces the onset of crystallization (T = 200°C) followed by melting of the resulting pCBT (T = 226°C) are well resolved. The fact that the crystallization and melting enthalpies are fairly matched is in line with the above assignments. Note that the crystallization is a completely NR process whereas the melting is not – cf. R and NR traces in Figure 1a. The small endothermic peak in the R trace (enthalpy = 1.2 J/g) may be attributed to the presence of some perfect crystals. Figure 1b, displaying the cooling trace, demonstrates that the crystallization is an NR process, in fact. On the R trace in Figure 1b the reverse glass transition (T_g) step is well resolved at T = 40°C. The instability in the R trace (that occurs in all MDSC measurements and marked by a questions mark) is possibly linked with the temperature modulation set. As mentioned earlier the effects of the modulation parameters were not considered in this work. During the second heating (cf. Figure 1c) the pCBT formed exhibits a double melting peak. The related exothermic peak (enthalpy = 37.8 J/g) in the NR trace suggests that this double melting is due to massive recrystallization.

3.2. CBT with organoclay (dry blend)

Figure 2 shows the MDSC traces of the CBT + organoclay-dry blend upon first heating, cooling and second heating, respectively. In trace NR of Figure 2a the peak assigned to the recrystallization of the CBT oligomers at T = 140°C is well detectable. Comparing Figures 2a and 1a two significant effects, caused by the presence of organoclay, can be noticed. First, a double endothermic peak appears in the NR traces (T = 143 and = 155°C) which was practically absent for the plain CBT (cf. Figure 1a). This suggests that the recrystallization of the oligomers and/or the polymerization were affected by the organoclay. This note is based on the fact that the organoclay was well intercalated in the corresponding nanocomposites (not presented here). The intercalation affects the conformational possibilities of the molecules, and thus the related entropy change, irrespective whether it happened with the CBT (most probable) or pCBT. Second, the organoclay hinders the crystallization of the pCBT as hardly any crystallization peak can be found in the NR and C traces for the pCBT formed (cf. Figures 2a and 1a). As a consequence, no melting peak appears in the R, C and NR traces. The finding that the organoclay does not act as nucleant for the pCBT crystallization is quite surprising. It was quoted in the literature that this is the primary effect of most organoclays in semi crystalline systems [11]. As pCBT was formed also in this case (cf. Figures 2b and 2c) which, however did not undergo crystallization, one can claim that the polymerization and crystallization of pCBT are consecutive processes. It is noteworthy that the crystallization of pCBT was reported to be kinetically hindered during fast heating scans [12]. The crystallization peak registered during cooling (cf. Figure 2b) is broader than that of the plain pCBT (cf. Figure 1b). In addition, the overall specific enthalpy values are also smaller. During second melting the double melting peak of the pCBT is still present, however, with additional features. In contrast to plain pCBT, the melting peak at higher temperature is more pronounced for the organoclay

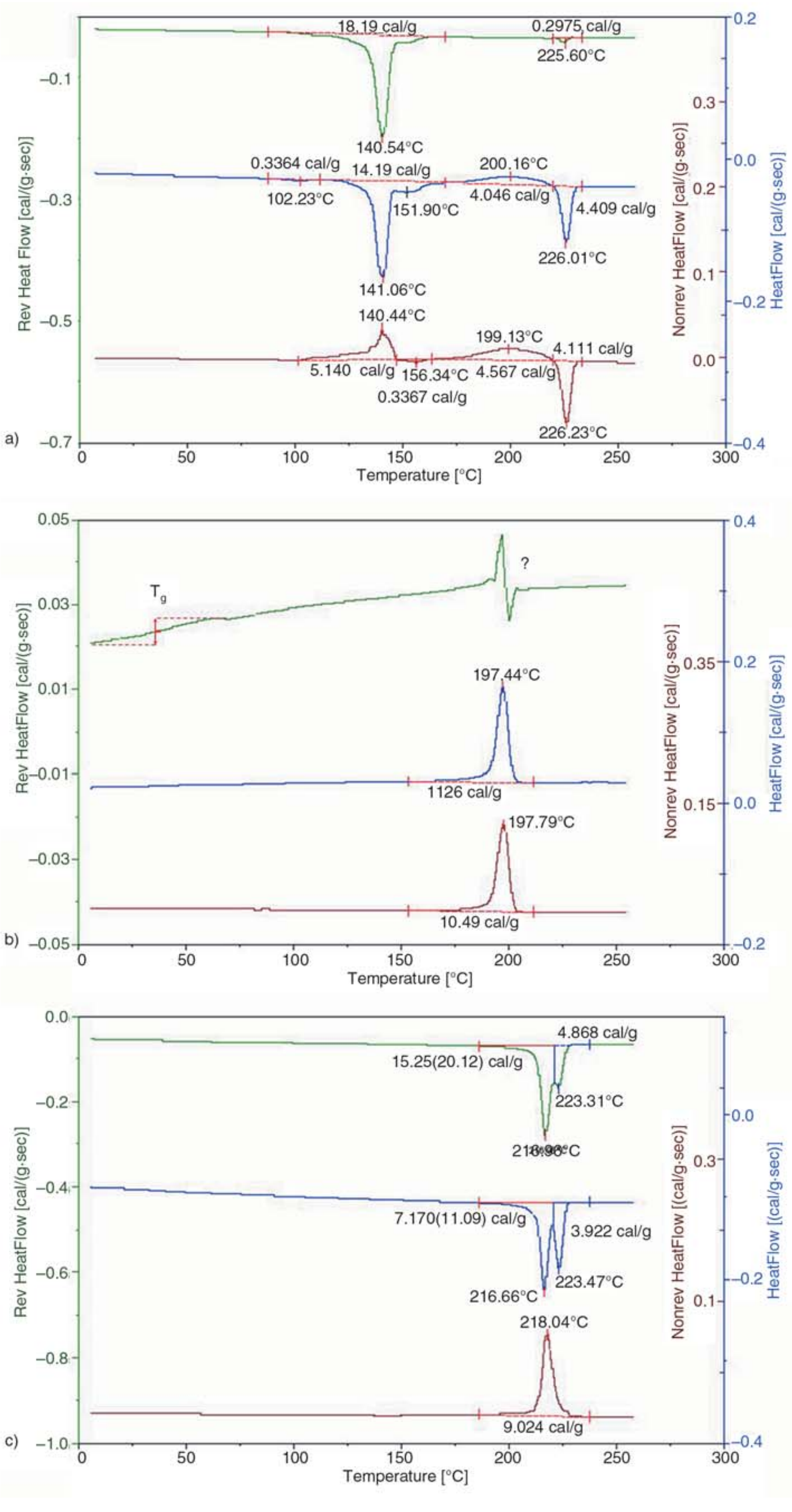

Figure 1. R, C and NR traces monitored during the first heating (a), cooling (b) and second heating (c) for the plain (p)CBT. Notes: The order of the traces is from the top to bottom: R, C and NR, respectively. The related traces show how the peaks were split for the enthalpy determination. To convert cal in J units multiply the former (indicated in the traces) values by 4.184

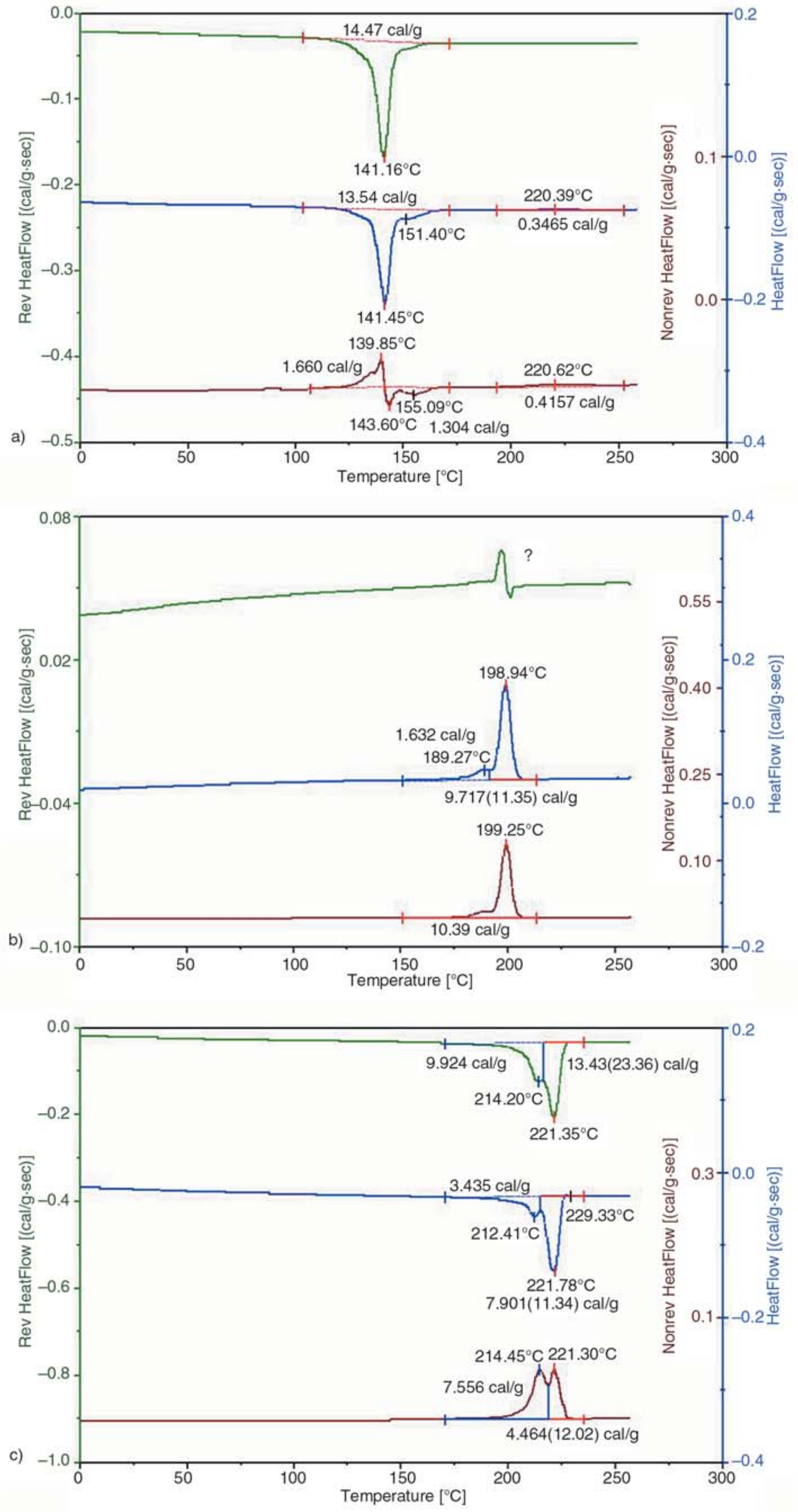

Figure 2. R, C and NR traces monitored during the first heating (a), cooling (b) and second heating (c) for the CBT + organoclay-dry blend. For notes cf. Figure 1

modified version (cf. R and NR traces in Figures 1c and 2c, respectively). This suggests that more perfect crystals were formed which, however, still undergo recrystallization phenomena. The latter is evidenced by the double exothermic peak (which differs again from the plain pCBT) of the NR trace in Figure 2c.

3.3. CBT with organoclay (melt blend)

The first heating scan of the melt blended system shows some further peculiarities (cf. Figure 3a). Both R and C traces display multiple melting peaks, the peak temperature of which is far less than that of the initial CBT (T = 126 instead of 140°C, cf. Figure 1a). The melting in this sample starts already at T = 70°C. The corresponding exothermic peak in the NR trace is very broad and shifted to markedly lower temperature when compared to the plain CBT (cf. Figures 3a and 1a). The possible explanations for this finding are listed below. Melt mixing followed by quenching yielded a far less crystalline CBT version. This becomes more and more crystalline due to recrystallization of the corresponding oligomers. Recrystallization phenomena are reflected by the broad exothermic peak (T = 122°C, enthalpy = 32.2 J/g) in the NR trace (cf. Figure 3a). An alternative explanation is that the cyclic oligomers are partly broken up owing to intercalation with the organoclay. This process may be favored by the –OH groups of the organophilic modifier of the montmorillonite clay used. The resulting compounds may have a lower melting point than the cyclic counterparts. However, it was found that the quenched CBT with yellow/brown color becomes more crystalline and white colored when keeping at sufficient high temperature (but below the melting of the plain CBT). This suggests that the first explanation is the correct one. A similarity with the dry blended version is that the organoclay hampers the crystallization of the pCBT. Note that the crystallization-related exo- and melting-related endothermic peaks in the C and NR traces are practically missing (cf. Figure 3a). This is a similarity with the CBT dry blended with the organoclay (cf. Figure 2a). The peak shapes in the C and NR traces in Figure 3b indicate that the crystallization of pCBT occurs faster and gives more homogeneous crystallites than for the dry blend (cf. Figure 2b). During second heating (cf. Figure 3c) again a double melting peak can be observed in both R and NR traces. Similar to the dry blend (cf. Figure 2c), one can see again the doubling in the recrystallization peak in the NR trace for this melt blended version (cf. Figure 3c).

3.4. pCBT with organoclay (pCBT + organoclay)

In the DSC traces of this pCBT containing 5 wt.% organoclay (recall that this compound was polymerized at T = 190°C for 30 min) one can see only the melting of the pCBT (cf. traces R and C in Figure 4a). Albeit the melting peak is very sharp, the melting takes place via recrystallization. This is indicated by the related exothermic peak in the NR trace in Figure 4a. It is interesting to note that before the onset of this exothermic peak in the NR trace, an endothermic peak appears (T = 222°C; enthalpy = 7.3 J/g). This may be linked with some constraint effects that allow the necessary reorganization only after their release. The MDSC traces registered during cooling (Figure 4b) and second heating (Figure 4c) do not offer new insights in the crystallization and melting processes of the pCBT nanocomposites compared to the plain pCBT [6].

It is noteworthy that to check the intercalation/exfoliation of the organoclay was not the scope of this paper. On the other hand, it is essential to give information on whether or not the incorporation of organoclay affected the conversion of the CBT and the mean molecular mass of the corresponding pCBT. So, gel permeation chromatographic (GPC) tests were performed on pCBT and pCBT + organoclay samples polymerized at identical conditions (T = 190°C, time = 30 min). It was found that both conversion (93 instead of 95%) and mean weight average molecular mass data (91.3 instead of 104 kDa) were reduced slightly by incorporation of the organoclay. It is worth of noting that the organophilic modifier of the clay may strongly influence both conversion and molecular mass characteristics. Using an organophilic montmorillonite with primary amine (viz. octadecylamine) intercalant a conversion of only ca. 70% was reached.

4. Conclusions

Based on this work devoted to study the MDSC response of polymerizing and polymerized cyclic butylene terephtahalate (CBT and pCBT, respec-

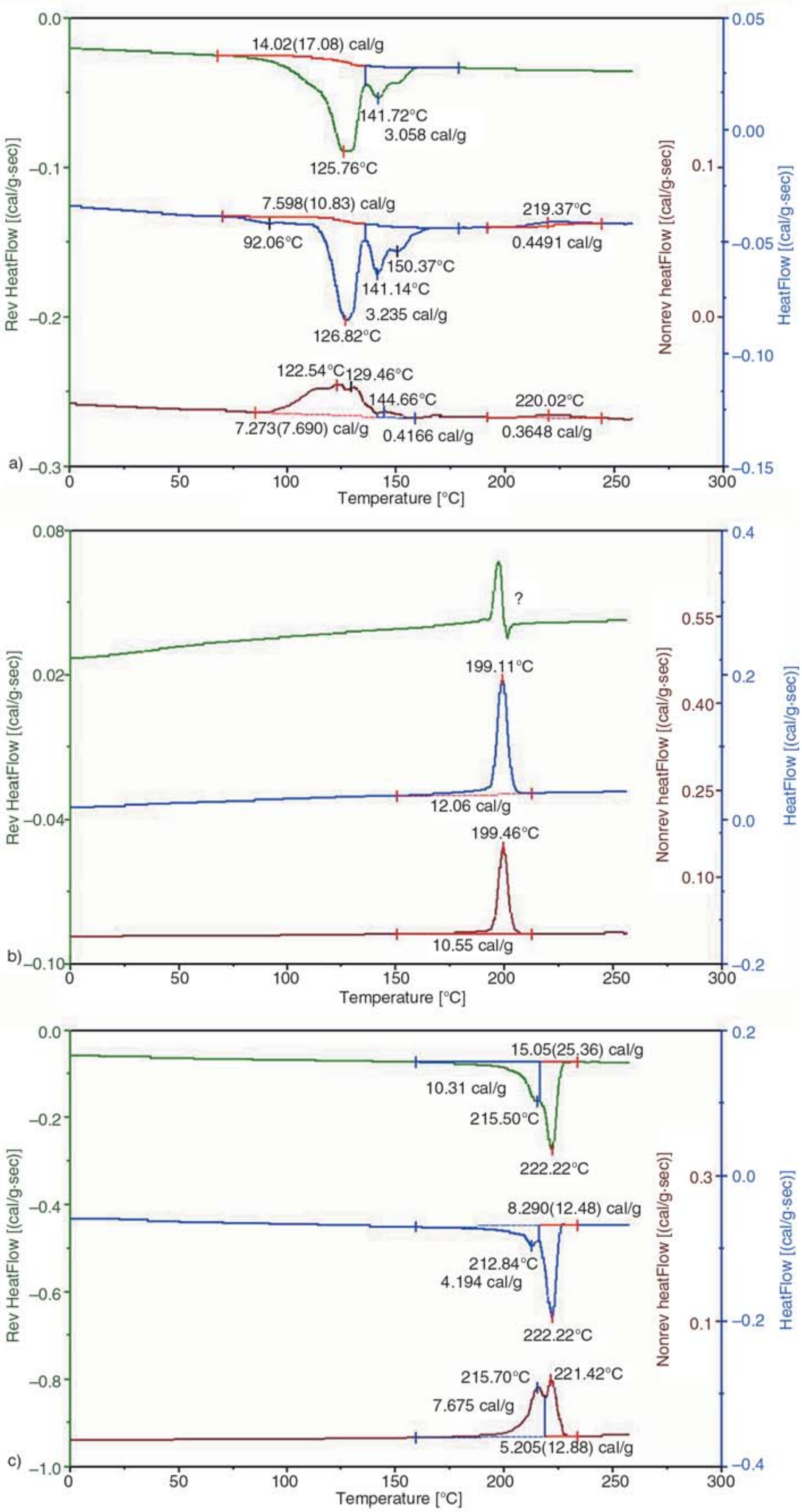

Figure 3. R, C and NR traces monitored during the first heating (a), cooling (b) and second heating (c) for the CBT + organoclay-melt blend. For notes cf. Figure 1

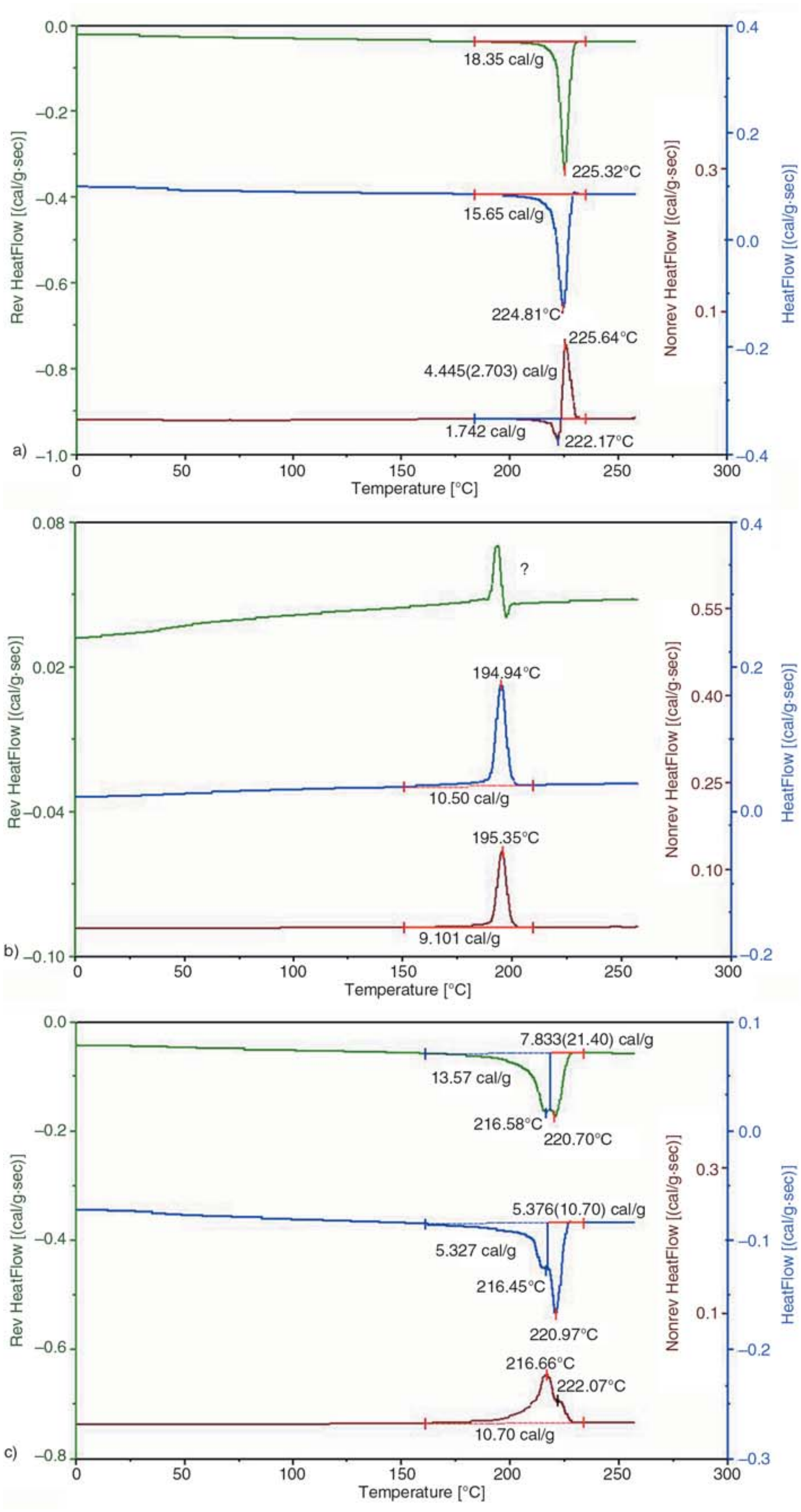

Figure 4. R, C and NR traces monitored during the first heating (a), cooling (b) and second heating (c) for the pCBT + organocaly. For notes cf. Figure 1

tively) in absence and presence of an organoclay (Cloisite® 30B incorporated in 5 wt.%), the following conclusions can be drawn:

- the preparation of the samples influences the crystallization and melting behaviors of the in-situ polymerized pCBT systems. On the other hand, the molecular mass characteristics and conversion are less affected by the organoclay used.
- the organoclay reduces the crystallization ability of the pCBT but likely produce more perfect crystals. As the crystalline structure of pCBT is very complex (e.g. [13]), this aspect has to be checked by X-ray diffractions measurements.
- melt blending with organoclay followed by quenching strongly alter the crystalline morphology of the CBT oligomers that should be clarified also through X-ray diffraction. Nevertheless, melt mixing of nanoparticles (any kind) with uncatalyzed CBT prior to introducing the catalysts may be an interesting route to produce nanocomposites.

Acknowledgements

Z. A. Mohd Ishak is thankful to the Alexander von Humboldt Foundation for his Georg Forster Research Fellowship at the IVW. Parts of this work were supported by the BMBF (Pro-PBT) and DFG (Ka 1202). The authors thank Prof. J. Varga (TU Budapest, Hungary) for his critical remarks to the manuscript.

References

[1] Brunelle D. J.: Synthesis and polymerization of cyclic polyester oligomers. in 'Modern Polyesters' (eds.: Scheirs J. and Long T. E.), Wiley, Chichester, 117–142 (2003).

[2] Tripathy A. R., MacKnight W. J., Kukureka S. N.: In-situ copolymerization of cyclic poly(butylene terephthalate) oligomers and ε-caprolactone. Macromolecules, **37**, 6793–6800 (2004).

[3] Mohd Ishak Z. A., Gatos K. G., Karger-Kocsis J.: On the in-situ polymerization of cyclic butylene terephthalate oligomers: DSC and rheological studies. Polymer Engineering and Science, **46**, 743–750 (2006).

[4] Parton H., Verpoest I.: In-situ polymerization of thermoplastic composites based on cyclic oligomers. Polymer Composites, **26**, 60–65 (2005).

[5] Mohd Ishak Z. A., Leong Y. W., Steeg M., Karger-Kocsis J.: Woven glass fabric composites via in-situ polymerized cyclic butyene terephthalate oligomers. SPE-ANTEC, 186–189 (2006).

[6] Mohd Ishak Z. A., Shang P. P., Karger-Kocsis J.: A modulated DSC study on the in-situ polymerization of cyclic butylene terephtghalate oligomers. Journal of Thermal Analysis and Calorimetry, **84**, 637–641 (2006).

[7] Utracki L. A.: Clay-Containing Polymer Nanocomposites, Vols. 1–2, Rapra Technology, Shawbury (2004).

[8] Tripathy A. R., Burgaz E., Kukureka S. N., MacKnight W. J.: Poly(butylene terephthalate) nanocomposites prepared by in-situ polymerization. Macromolecules, **36**, 8593–8595 (2003).

[9] Lee S-S., Ma Y. T., Rhee H-W., Kim J.: Exfoliation of layered silicate facilitated by ring-opening reaction of cyclic oligomers in PET-clay nanocomposites. Polymer, **46**, 2201–2210 (2005).

[10] Barger M., Walia P., Dion R. P., Paquette M. S., Bank D. H., Lebaron P. C., Read M. D, Oelberg J. D.: Polymerized macrocyclic oligomer nanocomposite compositions. WO 2004/058868, USA (2003).

[11] Karger-Kocsis J., Zhang Z.: Structure-property relationships in nanoparticle/semicrystalline thermoplastic composites. in 'Mechanical Properties of Polymers Based on Nanostructure and Morphology' (eds.: Michler G. H. and Baltá Calleja F. J.), CRC Press, Boca Raton, 553–602 (2005).

[12] Mohd Ishak Z. A., Leong Y. W., Steeg M., Karger-Kocsis J.: Mechanical properties of woven glass fabric reinforced in situ polymerized poly(butylene terephthalate) composites. Composites Science and Technology, **67**, 390–398 (2007).

[13] Parton H., Baets J., Lipnik P., Goderis B., Devaux J., Verpoest I.: Properties of poly(butylene terephthalate) polymerized from cyclic oligomers and its composites. Polymer, **46**, 9871–9880 (2005).

eXPRESS Polymer Letters Vol.1, No.2 (2007) 69–76
Available online at www.expresspolymlett.com
DOI: 10.3144/expresspolymlett.2007.13

Copolymerization of carbon monoxide and styrene catalyzed by resin-supported palladium polymer

J. Guo[*]*, B. Wang, C. Zhu*

Department of Chemical Engineering and Technology, Tianjin University, Tianjin 300072, China

Received 2 November 2006; accepted in revised form 13 January 2007

Abstract. Polyketone was prepared by the copolymerization of carbon monoxide (CO) and styrene (ST) catalyzed by *o*-phenylenediamine resin-supported palladium acetate. Effects of each catalytic system component such as 2,2'-bipyridine, 1,4-quinone and *p*-toluene-sulphonate on the copolymerization were investigated. The resin-supported catalyst and the copolymerization product were characterized by infrared spectroscopy (IR), differential scanning calorimetry (DSC), thermogravimetry (TG), X-ray photoelectron spectroscopy (XPS), scanning electron microscopy (SEM). Results indicated that the resin-supported catalyst has excellent catalytic property. Furthermore, partial catalytic activity was maintained after the catalyst was used for five times.

Keywords: *polymer synthesis, molecular engineering, polyketone, resin, carbon monoxide, styrene*

1. Introduction

Alkene-carbon monoxide alternating copolymers are of considerable interest from different viewpoints [1]. Copolymerization using carbon monoxide for polymer materials avoids environmental pollution and makes great uses of carbon resources as well. Numerous polymer materials can be derived from polyketone by chemical modification of the ketone on the main chain [2]. Besides, the ketone auxochrome group on the main chain also provides polyketone with excellent photo decomposition property [3], and the carbonyl groups in the polyketone can be chemically modified easily to other classes of functional polymers.

In the 1940s, Reppe *et al.* [4] first synthesized copolymer of styrene and carbon monoxide by using $KNi(CN)_4$ as catalyst. However, the catalytic activity was relatively low. In the 1970s, Drent *et al.* [5] from the Holland Shell Laboratory investigated a series of catalyst with high catalytic and low cost, and applied them into the copolymerization of styrene and carbon monoxide. Since then, enormous efforts have been placed on the research of synthesis of polyketone from carbon monoxide and alkene, and more and more kinds of polyketone have been synthesized [6–10]. Currently, in the area of polyketone synthesis, metal catalysts are mostly ruthenium, rhodium, palladium, osmium, yttrium, platinum, etc. Among those metals, palladium has the highest catalytic activity [11]. However, its high cost makes lowering the cost of polyketone synthesis the most important issue.

Due to the high cost of the catalyst, reuse becomes an effective way to reduce the production cost. Here, the cation resin was used to absorb Pd^{2+} in the waste solution of the copolymerization. The waste solution was also condensed and recycled, which increased the catalytic activity of the copolymerization [12–16]. Due to the similarity of the bidentate nitrogen structure in both of the *o*-phenylenediamine and 2,2'-bipyridine, we applied the micro-balls of *o*-phenylenediamine resin-sup-

---

[*] Corresponding author, e-mail: jintang_guo@sina.com

ported palladium acetate in the copolymerization, and investigated the catalytic property and reusability of the catalyst.

2. Experimental

2.1. Raw materials

Palladium acetate (analytical reagent (AR), ACROS Organics, NJ, USA); styrene (AR, Tianjin 1st Chemicals Factory); carbon monoxide (Beijing Hepubei Air Industry Ltd.); *p*-toluene-sulphonic acid (AR, Tianjin Huazhen Special Chemicals Factory); 2,2'-bipyridine (AR, China Medicals Group/Shanghai Chemicals Company); 1,4-quinone (Chemical pure, North China Special Chemicals Development Center); benzene and o-phenylenediamine (AR, Tianjin Kemiou Chemicals Ltd.); methanol (AR, Tianjin 1st Chemicals Factory); ethanol (Industrial pure, Tianjin University Kewei Company); chloride ball (Tianjin Nankai University Resin Factory).

2.2. Purification of raw materials

The analytical reagent styrene was vacuum distilled and stored at low temperature before use. The pure methanol was distilled at normal pressure for further usage. All other materials were used as received.

2.3. Preparation of the resin-supported palladium catalyst

o-phenylenediamine resin was obtained by immersing the chloride ball and o-phenylenediamine in the ethanol for 24 hours. The above obtained *o*-phenylenediamine resin was then immersed in benzene with the palladium acetate, stirred at room temperature, and the *o*-phenylenediamine resin-supported Pd catalyst was obtained.

2.4. Copolymerization

The copolymerization of CO and ST was catalyzed by the resin-supported Pd catalyst Into a 110 ml electromagnetic stirring steeliness autoclave, 2,2'-bipyridine, 1,4-quinone, *p*-toluene-sulphonic acid, and balls of the resin-supported Pd were added to form the catalytic system. Methanol and styrene were then added, and CO flowed in at 2 MPa. The reaction was kept in a 60°C water bath and constant pressure for 2 hrs. When the copolymerization is over, the autoclave was cooled down to room temperature and the unreacted CO was released. Ethanol was used to precipitate the product. The white powder was obtained after washing, filtration, and drying.

2.5. Characterization of the catalyst and copolymer

The palladium ion content in the resin was determined by ICP-9000(N+M) (Inductively-coupled plasma emission spectrometer). The infrared spectrum of the aminated resin and the copolymer were measure by the Bio-Rad FTS 3000 spectrometer in the form of pellets pressed with KBr. Differential scanning calorimetry (DSC) analysis of the polyketone was carried out with a Shimadzu DSC-50 in nitrogen atmosphere (10 ml/min) at the heating rate of 10°C/min. The thermal porperties of the copolymer was studied. Thermogravimetric analysis (TGA) of the polyketone was performed using a Shimadzu TGA-50 under the same conditions as thhose of the DSC analysis. The thermal decomposition property of the copolymer was studied by TGA. X-ray photoelectron spectroscopy (XPS) measurements were used to investigate the surface elements and relative contents of the resin-supported catalyst and the copolymer. It was performed on a Perkin Elmer PHI-1600 spectrometer with Mg Kα (1253.6 eV) radiation and a hemispherical analyzer operating at constant pass energy of 23.5 eV. Spectra were recorded with the X-ray generator operated at 3000 W and the chamber vacuum was 667 nPa. The radiation area was 0.8 mm^2. Al 2*p* (74.00 eV) in Al_2O_3 was used as an internal reference.

3. Results and discussions

3.1. Characterization of the resin-supported catalyst and the copolymer

Small, brown coloredn aminated resin balls were prepared by the reaction of *o*-phenylenediamine and chloride ball in the ethanol solvent. Reaction of the aminated resin balls with palladium acetate in benzene solvent at room temperature for 24 hrs yielded the resin-supported palladium catalyst. Figure 1 shows above described reactions.

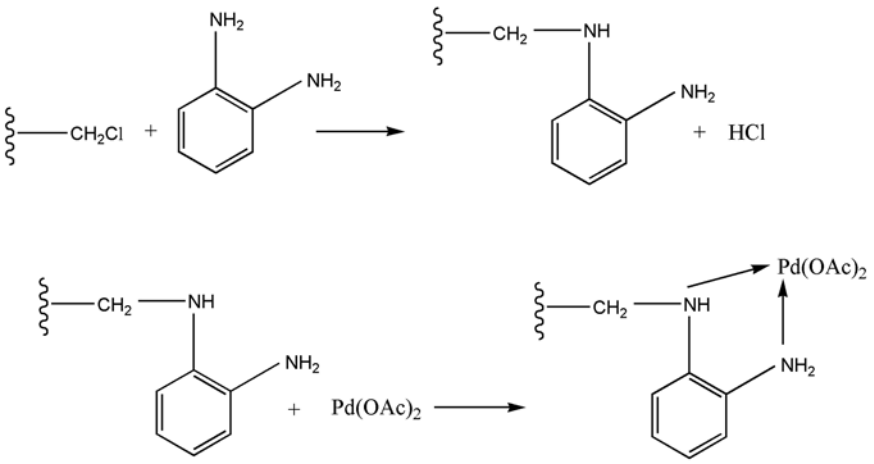

Figure 1. Synthesis route of the resin-supported catalyst

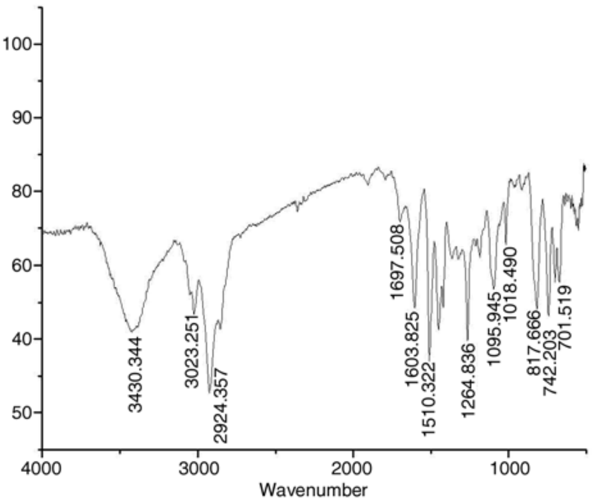

Figure 2. IR of the aminated functional resin

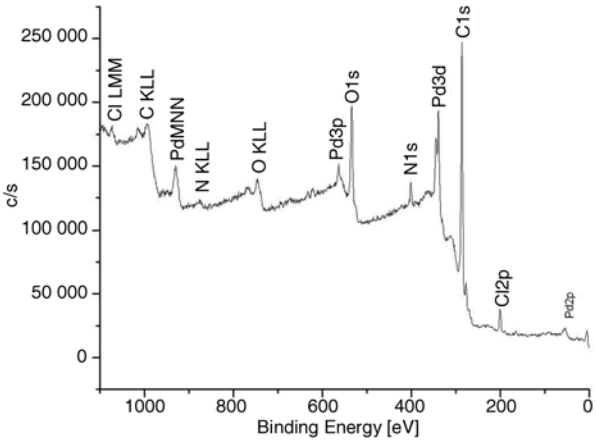

Figure 3. XPS of the resin-supported catalyst

Figure 2 shows the IR spectrum of the aminated resin. Due to the similarity of the characteristic peaks of primary and secondary amines above 3000 cm^{-1}, a broad peak at 3430 cm^{-1} is observed in the spectrum, which is the result of the overlap of primary and secondary amine characteristic peaks. The peak at 1603 cm^{-1} is the bending vibration peak of primary amine; the absorption peak at 1018 cm^{-1} is the stretching vibration peak of C–N; the strong spectrum area at 1510 cm^{-1} is the overlap result of NH_3^+ and the benzene skeletons vibration absorption band. Absorption peaks at 697 cm^{-1} and 750 cm^{-1} are the in-plane bending vibration peaks of =CH on the benzene. This is the characteristic absorption band of singly substituted benzene. There are several absorption peaks from 1453 cm^{-1} to 1600 cm^{-1}, which are caused by the vibration of the benzene skeleton. These are the characteristic absorption bands of the benzene ring. The IR spectrum result revealed that –Cl in the chloride ball was partly substituted by $-NH_3$ of o-phenylenediamine, and corresponding aminated resin was yielded.

Figure 3 shows that the XPS found the existence of palladium and oxygen, which indicated that the palladium acetate was loaded on the resin surface. A tiny amount of chloride was detected, which possibly origins from unreacted chloromethyl. At the same time, XPS and SEM (Table 1) were applied to measure the palladium content in both the whole body and the core of the resin ball. Results showed 2.1 wt% and 0.62 wt% Pd contents, respectively, which quantitatively proved the existence of the Pd at the resin surface.

Table 1. Elements on the surface of resin-supported catalyst by SEM

element	wt%
C K	91.07
N K	Pd L
8.31	0.62
gross	100.0

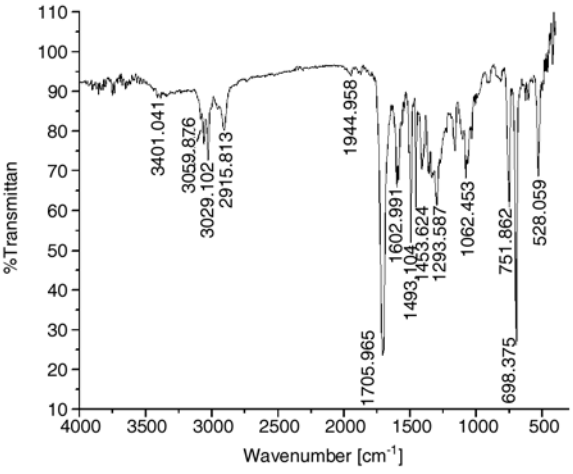

Figure 4. IR of polyketone

White powder was yielded from the copolymerization of CO and ST catalyzed by the resin-supported Pd. Its IR spectrum is shown in Figure 4. It is shown that the product has a strong characteristic absorption peak of ketone at 1703 cm^{-1}. Besides, absorption peaks at 697 cm^{-1} and 750 cm^{-1} were induced by the out-of-plane bending vibration of =CH on the benzene. It is the benzene single substitution characteristic absorption band. There are also several absorption peaks from 1453 cm^{-1} to 1600 cm^{-1}, which were caused by the vibration of the benzene skeleton and it is the benzene characteristic absorption band. All of the above indicated that the copolymer has structure comes from both the carbon monoxide and the styrene.

Figure 5 shows the Differential scanning calorimetric curve of the copolymerization product which was heated at 10°C/min in the nitrogen atmosphere. Its glass temperature (T_g) is 235°C and the melting point is 275°C.

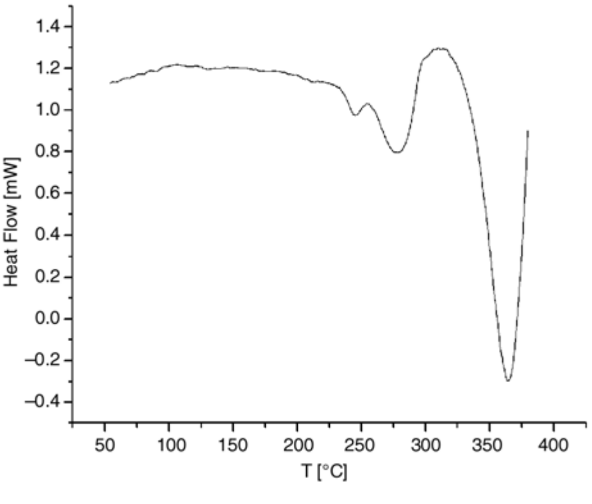

Figure 5. DSC curve of the polyketone

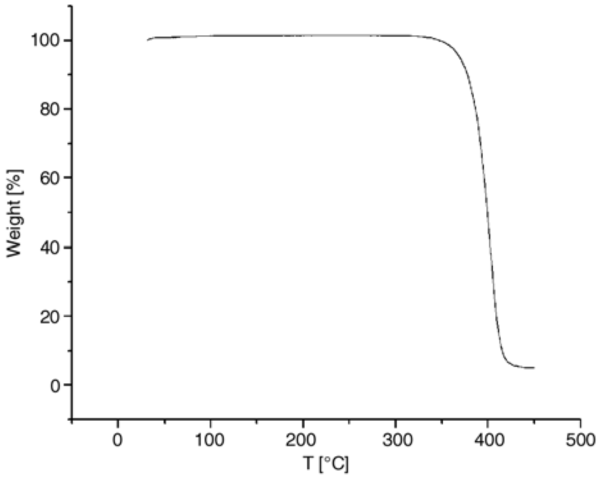

Figure 6. TGA curve of the polyketone

Figure 6 shows the thermogravimetric analysis of the polyketone which was heated at 10°C/min in the nitrogen atmosphere. The initial weight loss temperature is 340°C and the complete weight loss temperature is 420°C.

3.2. Effect of the resin amount on the yield and the catalytic activity

Figure 7 shows the effect of the resin amount on the copolymerization yield. It shows that the resin amount has significant affect on the yield. As the resin amount gradually increases, the yield first increases and then decreases. The maximum yield of 250 mg was obtained when the resin amount was 0.3 g. Compared to the traditional homogeneous catalytic system, the active center of the resin-supported catalyst in the reaction system is randomly

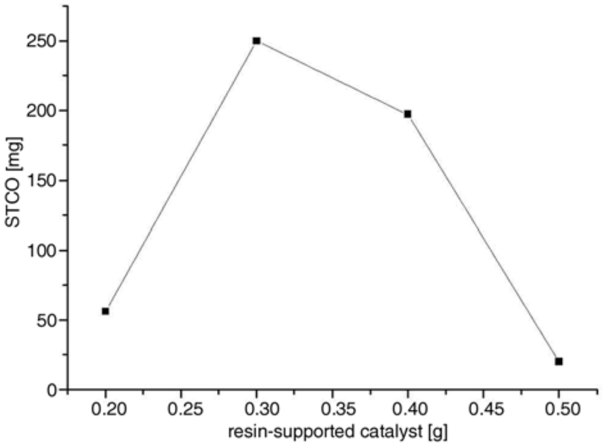

Figure 7. Effect of the amount of the resin-supported catalyst on the yield. Reaction conditions: 2,2'-bipyridine: 1.5·10^{-4} mol; 1,4-quinone: 20·10^{-4} mol; *p*-toluene-sulphonic acid: 1.5·10^{-4} mol; styrene: 15 ml; methanol: 6 ml; CO: 2 MPa; 60°C; 2 h

distributed. When small amount of the resin is used, the effective active center gathered at the resin surface, which results in the absence of the catalytic active center in most reaction area and therefore the yield is low. As the resin amount increases, the resin volume in the autoclave increases. Since the stir is electromagnetic, with the increase of the solid content in the autoclave, the resin was hardly stirred adequately and thus a homogeneous and effective active center can barely be formed. The non-homogeneous distribution of the active center in the reaction system reduces the collision probability of CO and ST. It therefore reduces the catalytic activity of the reaction. The chloride ball resin used in the experiment is micro-reticular resin. SEM measurement showed the existence of Pd in the canal, which increases the difficulty of the catalytic reaction. If the catalytic active center is located in the resin canal, the collision probability of the CO will be dramatically decreased. The alternating copolymerization can hardly be fulfilled and the catalyst activation energy in the canal is extremely low.

3.3. Effect of the 2,2-bipyridine amount on the catalytic activity

In the copolymerization of the CO with ST catalyzed by Pd, the chelating structure of nitrogen ligand with palladium acetate showed excellent catalytic performance. This is one of reasons why the aminated resin was selected to support the palladium acetate. The kind and the amount of the bidentate ligand have considerable effect on the copolymerization, and also directly affect the stability and activity of the catalytic active center [5, 12]. Hence, 2,2’-bipyridine, which has the best chelating effect with Pd, was selected as the bidentate ligand in the catalytic system. The effect of the 2,2’-bipyridine amount on the polyketone yield was studied and the result is shown in Figure 6.

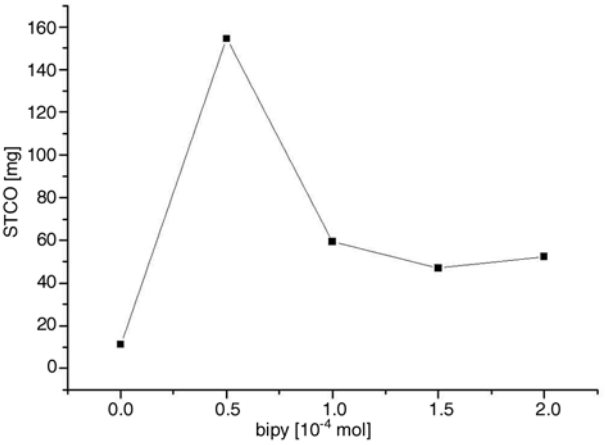

Figure 8. Effect of 2,2’-bipyridine amount on the yield. Reaction conditions were the same as in Figure 7 except that 0.3g resin was used and the 2,2’-bipyridine amount was varied

In Figure 8, it is shown that trivial amount of polyketone was yielded without the ligand addition. It indicates that the *o*-phenylenediamine structure plays the role of the ligand in addition to fixing Pd^{2+}. This assisted the catalytic role of Pd and resulted in small amount of yield. However, the above ligand structure is an insufficient substitution of the bipyridine ligand structure formed with Pd. When small amount of 2,2’-bipyridine was introduced to the system, the yield was dramatically increased, which indicated a more stable mono-chelating Pd–N structure was formed and the catalytic performance was also improved. As the ligand amount continued to increase, excess ligands chelated with Pd or gathered around Pd, which resulted in the formation of the bichelating structure. Though the active center is stable, inducing of the monomer became difficult and the yield decreased. The maximum yield of 154.6 mg was obtained when the ligand amount was $0.5\cdot10^{-4}$ mol.

3.4. Effect of the 1,4-quinone amount on the catalytic activity

In the copolymerization of the CO and ST, 1,4-quinone addition has the following effects: first of all, it acts as an effective anti-copolymerization agent, which prevents the copolymerization of the styrene; secondly, it is also used as a strong oxidizer, which prevents the reduction of the Pd^{2+}. Pd(II)-H can be effectively oxidized to Pd(II)-OMe and becomes the catalytic active center. Hence, opportune amount of the 1,4-quinone improves the reaction catalytic activity.

Figure 9 shows the effect of the 1,4-quinone amount on the catalytic activity. When trivial amount of the 1,4-quinone was applied, the catalyst is prone to decomposition and loses its catalytic activity. The yield was low. When excess amount of the 1,4-quinone was used, the product was white powder but the yield was low. This is due to the insoluble part of the 1,4-quinone, which makes the system non-homogenous and affects the catalytic activity. The maximum yield of 158.8 mg was

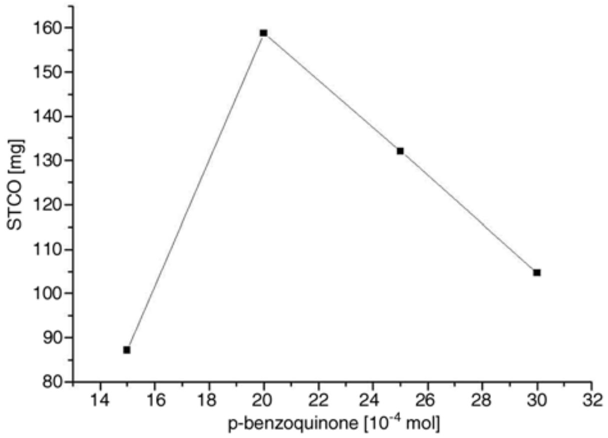

Figure 9. Effect of 1,4-quinone amount on the yield. Reaction conditions were the same as in Figure 7 except that 0.3 g resin was used and the 1,4-quinone amount was varied

obtained when the amount of 1,4-quinone was $20\cdot10^{-4}$ mol.

3.5. Effect of reused times on the catalytic activity

Reusability is an important factor in evaluating the performance of the resin-supported catalyst. 0.3 g resin-supported catalyst was used in the study of its reusability. The effect of the number of reuse on the polyketone yield is shown in Figure 10.

In Figure 10, it is shown that the yield decreased as the number of reuse increases. This indicates the loss of Pd in the resin-supported catalyst. The loss of the catalyst is unavoidable in the application of the resin-supported catalyst. Therefore, the rate of the catalyst loss is a characteristic property of the resin-supported catalyst.

To better understand the Pd loss rate in the resin-supported catalyst, the Pd content in an unused, used once, and used four times resins were measured. Results and corresponding polyketone yields are shown in Table 2.

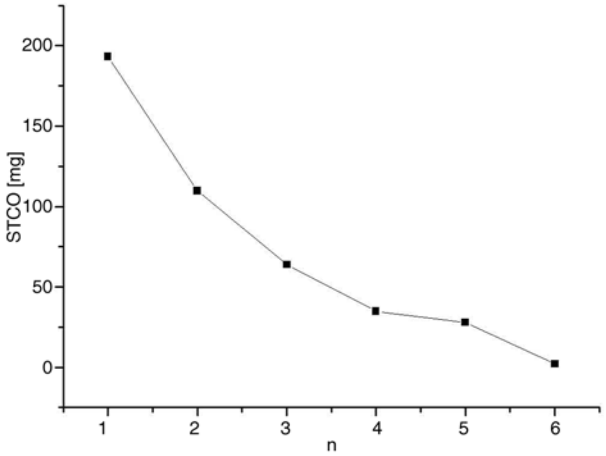

Figure 10. Effect of reused time on the polyketone yield

Table 2. Pd contents in the resin-supported catalyst and the corresponding yield at different numbers of reuse times

reused number	element	result	polyketone yield [mg]
0#	Pd	2.10%	193.2
1#	Pd	1.06%	109.9
4#	Pd	0.15%	27.7

Table 2 shows that the polyketone yield decreases as the Pd reused number increases. 50% Pd was lost after the first use of the resin; 90% or above Pd was lost after the resin had been used for four times. The resin-supported catalyst has less and less catalytic activity. The main factor that affects the loss of catalyst is the chelating ability of Pd with N. The chelating between *o*-phenylenediamine and Pd is a weak force. The palladium acetate loaded on the resin is prone to break and this limits the reuse of this resin-supported catalyst. The key to solve this problem is to select a proper amine compound to form a strong chelating structure with Pd.

3.6. Investigation of the catalytic properties of the dimethylamine resin-supported Pd catalyst

Different aminated resins show significant difference in chelating Pd. Above experiments also showed that the chelating effect of *o*-phenylenediamine with Pd is undesirable, where Pd was lost in reactions. There are two methyls, which are electron-donating groups, in the dimethylamine. Their electron-donating effect increases the density of the electron cloud, which assists the formation of a more stable chelating structure. Hence, *o*-phenylenediamine was substituted by dimethylamine in synthesis of the aminated resin and the resin-supported catalyst. All other reaction conditions were maintained.

However, no product was obtained in the polyketone copolymerization using the dimethylamine resin-supported catalyst. Furthermore, the color of the resin turned from yellow to black. This resin-supported catalyst has no catalytic activity in this experiment.

XPS of the dimethylamine resin-supported catalyst before and after the reaction are shown in Figure 11.

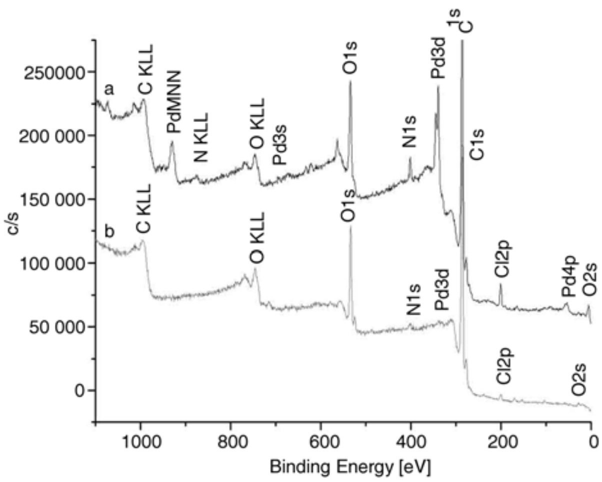

Figure 11. ,XPS of the dimethylamine resin-supported catalyst (a) before use; (b) after use

Comparison of the two XPS results reveals that there are Pd ions loaded on the resin surface before the reaction and small amount of that was left after the reaction. From all of the above results, it is shown that the chelating of N with Pd increases due to the electron-donating effect. However, only when the bidentate ligand was used to chelate with the Pd, can its two active sites be fixed and provide the other two active sites for monomer chelating. Dimethylamine only provides one N to chelate with Pd while the bichelating structure requires two. This is affected by the distribution of the dimethylamine in the resin. When two nitrogen ions are far away from each other, they cannot form chelate with the same Pd. Such structure has no catalytic activity and therefore has no yield. Part of the felled Pd^{2+} ions was oxidized to black Pd metal.

4. Conclusions

o-phenylenediamine resin was used to support the Pd catalyst. The catalytic system was composed of 2,2'-bipyridine, 1,4-quinone, and *p*-toluene-sulphonic acid. The alternating polyketone was prepared using CO and ST with above catalytic system.

Effects of every component in above catalytic system and the reaction time on the catalytic performance were investigated. The maximum yield of 250 mg was obtained with the optimum catalytic system composition of $0.5\cdot 10^{-4}$ mol 2,2'-bipyridine, $20\cdot 10^{-4}$ mol 1,4-quinone, and 0.3 g resin-supported Pd catalyst.

Reusability of the o-phenylenediamine resin-supported Pd catalyst was studies. The catalytic activity of the resin was maintained after five times two-hour reactions.

When *o*-phenylenediamine was substituted by dimethylamine, no catalytic activity was showed in the resin-supported Pd catalyst.

Acknowledgements

This project was financially supported by the National Natural Science Foundation of China (grant no. 20476080).

References

[1] Drent E., Budzelaar P. H.: Palladium-catalyzed alternating copolymerization of alkenes and carbon monoxide. Chemistry Reviews, **96**, 663–681 (1996).

[2] Drent E.: Process for the preparation of polyketones. 0181014 EP (1986).

[3] Jiang Z., Adams S. E., Sen A.: Stereo-and enantioselective alternating copolymerization of α-olefins with carbon monoxide synthesis of chiral. Polymers Macromolecules, **27**, 2694–2700 (1994).

[4] Reppe W., Magin A.: Production of ketonic bodies. 2562393 U.S. (1951).

[5] Drent E., Broekhoven J., Doyle M. J.: Efficient palladium catalysts for the copolymerization of carbon monoxide with olefins to produce perfectly alternating polyketones. Journal of Organometallic Chemistry, **417**, 235–251 (1991).

[6] Luo H. K., Li D. G.: Studies on new palladium(II) catalyst system for copolymerization of CO with ethylene. Journal of Molecular Catalysis A, **171**, 23–31 (2001).

[7] Sen A.: The copolymerization of carbon monoxide. Advances in Polymer Science, **73–74**, 125–144 (1986).

[8] Ittel S. D., Johnson L. K., Brookhart M.: Late-metal catalysts for ethylene homo- and copolymerization. Chemical Reviews, **100**, 1169–1204 (2000).

[9] Peng J. J.: The copolymerization of carbon monoxide with ethane. Petrochemical Technology, **10**, 707–709 (1997).

[10] Barsacchi M., Consiglio G., Medici L., Petrucci G.: Syndiotactic poly(1-oxo-2-phenyltrimethylene):on the mode of the chain growth under palladium catalysis. Angewandte Chemie-International Edition, **30**, 989–991 (1991).

[11] Desjardins S. Y., Cavell K. J., Hoare J. L., Skelton B. W., Sobolev A. N., White A. H., Keim W.: Single component N–O chelated arylnickel(II) complexes as ethene polymerisation and CO/ethene copolymerisation catalysts. Journal of Organometallic Chemistry, **544**, 163–176 (1997).

[12] Wang X. Y., Guo J. T., Xu Y. S., Sun J. W.: Study on the solution copolymerization of carbon monoxide with styrene. Journal of Tianjin University Sience and Technology, **34**, 249–252 (2001).

[13] Feng Y. K., Sun J. W., Zhu Y. B.: Study on the copolymerization of carbon monoxide and styrene by palladium(II)/2,2'-bipyridyl catalyst. Chinese Journal of Catalysis, **17**, 50–54 (1996).

[14] Pisano C., Mezzetti A., Consiglio G.: Selectivity of the carbonylation of styrene by cationic palladium complexes. Organometallics, **11**, 20–22 (1992).

[15] Guo J. T., Wang X. Y., Liu B.: Effect of acid on the copolymerization of carbon monoxide and styrene. Acta Petrolei Sinica (Petroleum Processing Section), **19**, 89–93 (2003).

[16] Guo J. T., Liu B., Li L. Wang X. Y., Sun J. W.: Copolymerization of carbon monoxide and styrene catalyzed by palladium-rare earth catalyst. Chinese Journal of Catalysis, **25**, 231–237 (1999).

eXPRESS Polymer Letters Vol.1, No.2 (2007) 77–83
Available online at www.expresspolymlett.com
DOI: 10.3144/expresspolymlett.2007.14

Mechanical, morphological and rheological properties of polyamide 6/organo-montmorillonite nanocomposites

*W. S. Chow**, *Z. A. Mohd Ishak*

School of Materials and Mineral Resources Engineering, Engineering Campus, Universiti Sains Malaysia, Seri Ampangan, Nibong Tebal 14300 Penang, Malaysia

Received 6 December 2006; accepted in revised form 24 December 2006

Abstract. Polyamide (PA6) nanocomposites containing 4 wt% organo-montmorillonite (OMMT) were melt-compounded followed by injection molding. The mechanical properties of the PA6/OMMT nanocomposites were studied through tensile and flexural tests. The rheological behaviour of the nanocomposites was determined by plate/plate rheological measurements. Attempts were made to trace the rheological parameters that reliably reflect the observed changes in the clay dispersion. X-ray diffraction (XRD) and atomic force microscopy (AFM) were used to characterize the exfoliation and dispersion of the OMMT in the PA6 matrix. The thermal properties of PA6/OMMT nanocomposite were characterized by Dynamic Mechanical Thermal Analysis (DMTA). The tensile modulus and strength of the PA6 was increased in the presence of OMMT. The flexural strength of PA6/OMMT was approximately doubled compared to the tensile strength value. The significant enhancement of both tensile and flexural strength was attributed to the delaminated clay formation. XRD and AFM results revealed the formation of PA6 nanocomposites as the OMMT was successfully exfoliated.

Keywords: *polymer composites, polyamide 6, organo-montmorillonite, nanocomposites*

---

1. Introduction

Polymer nanocomposites offer new technological and economical benefits. The incorporation of nanometer scale reinforcement may dramatically improve selected properties of the related polymer. These nanocomposites exhibit superior properties such as enhanced mechanical properties, reduced permeability, and improved flame retardancy [1]. Polymer layered-silicate nanocomposites are currently prepared in four ways: in-situ polymerization, solution intercalation, melt intercalation and sol-gel technology. Direct polymer melt intercalation is the most attractive because of its low cost, high productivity and compatibility with processing techniques (e.g. extrusion and injection molding) [2].

Numerous researchers described polymer-clay nanocomposites based on polyamide. Nylon 6-clay hybrid exhibits high modulus, high distortion temperature and good barrier properties of gas and water. Kojima *et al.* [3] have reported the synthesis of nylon 6-clay hybrid by montmorillonite intercalated with ε-caprolactam. They found that the silicate layers of nylon 6-clay hybrid were uniformly dispersed in the nylon 6 matrixes. Fornes *et al.* [4] have described the melt compounding of nylon 6/organoclay nanocomposites by using a twin-screw extruder. Tensile modulus and strength were found to increases with increasing concentration of clay. Cho & Paul [5] have reported that the organoclay was well exfoliated into nylon 6 matrix when compounded with twin screw extruder. Liu *et al.* [6] have reported the preparation of polyamide 6-clay nanocomposites/MAHgPP alloys and investigated its mechanical and dynamic mechanical properties and morphologies. The notched impact strength of

---

*Corresponding author, e-mail: shyang@eng.usm.my the alloys increased remarkably while its stiffness and strength still maintained. Chiu *et al.* [7] have studied the effects of maleic anhydride-grafted polyolefin elastomer (POEMA) on the properties of PA6/OMMT by using melt intercalation. González *et al.* [8] have investigated the toughening of PA6/OMMT by blending with maleinized styrene-ethylene/butadiene-styrene copolymer (mSEBS).

X-ray diffraction (XRD) and transmission electron microscopy (TEM) have been adopted as the standard techniques to study the clay (or layered silicates) dispersion in polymers. X-ray diffraction permits the study of intercalation, whereas TEM could provide evidence of intercalation/flocculation and exfoliation/delamination of clay. Atomic force microscopy (AFM) is a further suitable technique to study the microstructure and nanostructure of polymer nanocomposites. Karger-Kocsis *et al.* [9] have studied the morphology and topography of interpenetrating vinylester/epoxy/organoclay by using AFM technique. Chow *et al.* [10] have investigated the blend morphology and clay dispersion in PA6/PP matrix using AFM technique. Rheometers could be used to investigate the clay dispersion in the polymer matrix. The melt-state linear viscoelastic properties for the nanocomposites are typically examined in a constant strain rheometer in either a cone and plate or parallel plate (plate-plate) geometry. According to Krishnamoorti & Yurekli [11] the response of the intercalated and exfoliated nanocomposites to external flow is vital in their processing, but would also provide a systematic study of the response of highly anisotropic layers suspended in a viscoelastic medium. A transition from liquid-like to solid like rheological behaviour for nanocomposites at relatively low silicate loadings (1–2 vol.%) is observed with relatively small differences between intercalated and exfoliated systems.

The present work has devoted to study the effects of 4 wt.% OMMT on the mechanical, rheological and morphological properties of PA6. Thus, it is the aim of the present contribution to report the effect of OMMT in reinforcement and its ability of intercalation/exfoliation in PA6. This study attempts to enhance the tensile and flexural properties of PA6. Further, this paper was aimed at studying the rheological behaviour of PA6/OMMT nanocomposites at both high and low shear rates, and to interpret the rheological characteristics as a function of the morphology of the PA6 nanocomposites.

2. Experimental

2.1. Specimen preparation

The PA6 (Amilan CM 1017) used in this study was a commercial product from Toray Nylon Resin AMILAN, Japan. The melt flow index (MFI at 230°C and 2.16 kg load) and density of PA6 were 35 g/10 min and 1.14 g/cm^3, respectively. Organo-montmorillonite (Nanomer 1.30TC – OMMT) was a commercial product from Nanocor, Inc, USA. This OMMT is a white powder containing montmorillonite (70 wt%) intercalated by octadecylamine (30 wt%).

Melt compounding of the PA6 nanocomposites was done on a counter-rotating twin-screw extruder (Berstoff). The extrusion zone temperature ranged from 220–230°C. Prior to extrusion, PA6 pellets and organo-montmorillonite (OMMT) were dehumidified by using a vacuum oven at 80°C for 8 h. The extrudates were pelletized with a Haake pelletizer. The pellets were injection molded into standard tensile bars using a Niigata AN 50 injection molding machine. Injection molding temperature ranged from 225–240°C. Prior to injection molding, all pellets were dehumidified in a vacuum oven (80°C for 8 h). The tensile test specimens were molded in a Type I mold according to ASTM D638.

2.2. Mechanical studies

Tensile tests were performed on an Instron-5582 machine at 23°C, according to ASTM D638, at a crosshead speed of 50 mm/min. Tensile modulus, tensile strength and elongation at break were evaluated from the stress-strain data. Flexural measurements were carried out according to ASTM D790 using 3-point bending configuration at 3 mm/min deformation rate. The support span was set at 50 mm. Flexural modulus and strength were determined.

2.3. X-ray Diffraction (XRD)

Wide-angle X-ray spectra were recorded with a D 500 diffractometer (Siemens) in step scan mode using Ni-filtered Cu Kα radiation (0.1542 nm wavelength). Powder samples were scanned in reflection, whereas the injection-molded compounds were scanned in transmission in the interval of $2\theta = 2–10°$. The interlayer spacing of the OMMT was derived from the peak position (d_{001}-reflection) in the XRD diffractograms according to the Bragg equation ($\lambda = 2d\sin\theta$).

2.4. Atomic Force Microscopy (AFM)

Specimens were taken from the gauge section of the injection molded dumbbells. Their orientation was transverse to the mold flow direction. The surface of the specimens was first polished prior using further physical etching techniques. As for the physical etching, the polished surface of the specimens was eroded by Ar^+ ion bombardment. This occurred in a secondary neutral mass spectrometer (INA3 of Leybold) working at 500 eV energy. The beam was focused perpendicular to the surface of the specimens. The overall ion dose was $1.9\cdot10^{18}$ Ar^+/cm^2. The surface profile was scanned by AFM (MultiModeTM Scanning Probe Microscope, Digital Instruments) in tapping mode and the related topography image captured.

2.5. Plate/Plate Rheometry

Rheological measurements were made in dynamic mode on a rheometer (ARES rheometer, Rheometric Scientific) equipped with parallel plate geometry (plate diameter: 25 mm) at 230°C. Sheets were compression molded to about 1 mm thickness and punched into disc of 25 mm diameter. Dynamic frequency scan tests were conducted for all samples at a strain sweep of 1% at 230°C. The strain amplitude (1%) was within the linear viscoelastic region as deduced from dynamic strain scan tests performed for PA6 and PA6/OMMT nanocomposites.

2.6. Dynamic Mechanical Thermal Analysis (DMTA)

The storage modulus (E') and the mechanical loss factor ($\tan\delta = E''/E'$) as a function of temperature (T), were assessed by dynamic mechanical thermal analysis (DMTA) using an Eplexor 25N device of Gabo Qualimeter, Germany. DMTA spectra were taken in tension mode at 10 Hz frequency in a broad temperature range ($T = –110…+230°C$).

3. Results and Discussion

3.1. Mechanical properties

Table 1 shows the effect of OMMT on the tensile and flexural properties of PA6 nanocomposites. The tensile modulus and tensile strength of PA6 was improved significantly in the presence of OMMT. The stiffness of the OMMT filled PA6 composites is markedly higher than that of the neat PA6. This maybe attributed to the stiffness and reinforcing effects of the OMMT particles. Either full or partially delaminated clay formation is believed to be responsible for the increment in stiffness of PA6 nanocomposites. Cho & Paul [5] reported that the modulus of PA6 composite containing 5 wt.% of organoclay was substantially increased relative to neat PA6. Reichert *et al.* [12] also showed that the tensile modulus increased as a function of organophilic layered silicates content. Shelley *et al.* [13] considered the possibility that the modulus improvements are due to the constraint of the polymer chains by their interaction with the clay surfaces. According to Huang *et al.* [14], the introduction of the montmorillonite, which has a higher modulus than the organo-soluble polyimide (PI) matrix, leads to an increase in the modulus of the nanocomposite. The tensile modulus of PI increased almost linearly up to 5 wt.% of montmorillonite. However, as the montmorillonite content is further increased, the aggregation of the montmorillonite leads to a leveling off or even slightly decreases in the modulus of the hybrid. The addition of organoclay yields a substantial improvement in stiffness of the composites based on PA6 [4].

Note that the flexural modulus and strength of PA6 was improved significantly in the presence of OMMT. Recall that the OMMT has a plate-like structure irrespective to its degree of exfoliation. Accordingly, the platy OMMT and its silicate layers when exfoliated are aligned in the mold flow direction (MFD), especially in the skin layers. The injection-molding direction is parallel to the long

Table 1. Effects of OMMT on the tensile and flexural properties of PA6

Properties	Unit	PA6	PA6/OMMT
Tensile modulus	GPa	2.3 ± 0.02	3.0 ± 0.02
Tensile strength	MPa	40.1 ± 0.05	68.7 ± 0.10
Elongation at break	%	58.4 ± 0.05	3.5 ± 0.02
Flexural modulus	GPa	2.1 ± 0.02	2.9 ± 0.01
Flexural strength	MPa	94.2 ± 0.10	105.3 ± 0.10

axis of the layered silicates. This forced orientation is a result of the high shear rates during injection molding. This injection molding-induced skin-core morphology causes the observed increase in the flexural strength.

3.2. Morphological properties

3.2.1. X-ray diffraction (XRD)

Figure 1 shows the XRD patterns in the range of 2θ = 2–10° for PA6, OMMT and PA6/OMMT. The XRD spectrum of the OMMT exhibits a broad intense peak at approximately 2θ = 3.25° corresponding to a basal spacing of 2.72 nm. Note that the XRD spectra of PA6/OMMT do not shows a characteristic basal reflection of the OMMT. XRD spectra of the OMMT filled PA6 display a prominent increase in the intensity at lower 2θ values compared with neat PA6. This is due to the fact that the PA6 molecular chain success to intercalate into the inter-gallery of OMMT and further exfoliate the OMMT layered silicates. This reflects that the OMMT used was exfoliated in the PA6 matrix. Wu *et al.* [15] had reported a similar observation in the case of nylon 1012/clay nanocomposites. The absence of the characteristic clay d_{001} peak indicates the exfoliation of the clay platelets in the nylon 1012 matrix.

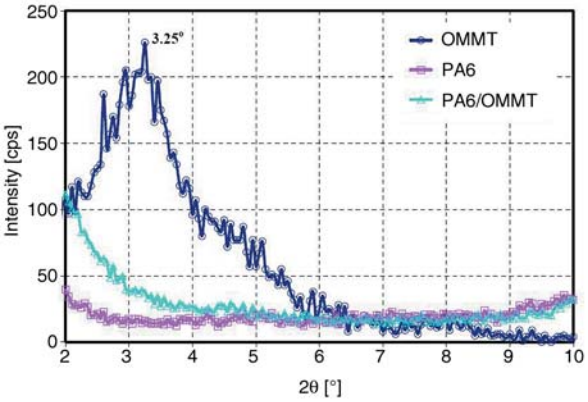

Figure 1. XRD spectra of PA6, OMMT and PA6/OMMT nanocomposites

3.2.2. Atomic force microscopy (AFM)

Figure 2a&b display the AFM surface topography of PA6 and PA6/OMMT after Argon ion bombardment. The great difference in the topography reflects the effect of OMMT. Recall that OMMT would act as nucleant for the γ-phase of PA6 which is likely less resistant to ablation than the α-phase. The white image represents the individual clay layers or layered silicates (i.e. platelet structure shown by the arrow). The average length of the plate-like structure is approximately 0.5 micrometer. Note that the silicate layer of OMMT was exfoliated in the PA6 matrix.

3.3. Rheological properties

A deeper insight into morphology-dependent flow behavior was expected from the rheological measurements performed in the viscoelastic range. The storage modulus (*G'*) resulting from dynamic frequency scans is depicted in Figure 3a. The storage modulus (*G'*) increased monotonically in the covered frequency range when OMMT was introduced to the PA6 nanocomposites. This reflects the strong effects of intercalated/exfoliated clay silicate layers on the viscosity of PA6. Besides, the increasing of the *G'* values of PA6/OMMT compared with the neat PA6 is attributed to the interaction of PA6 and OMMT. The slope values of *G'* for PA6 at 1 rad/s and 100 rad/s is 0.92 and 1.25, respectively. On the other hand, the slope values of *G'* for PA6/OMMT nanocomposites at 1 rad/s and 100 rad/s is 0.89 and 0.96, respectively. According to Li *et al.* [16], changes of *G'* in the viscoelastic range sensitively

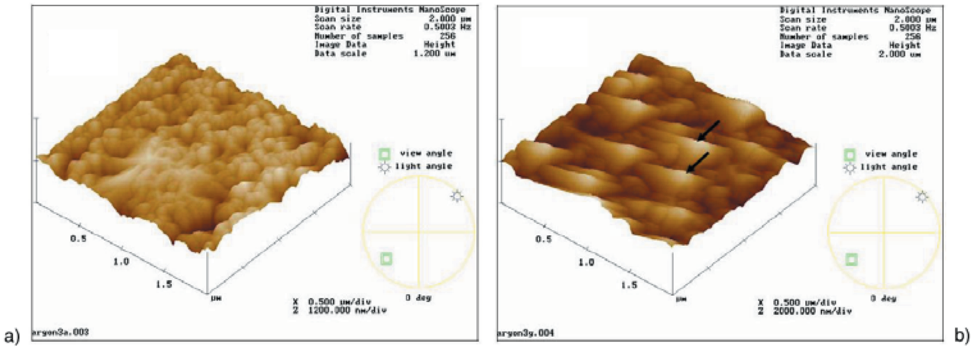

Figure 2. a – AFM surface topography of PA6; b – AFM surface topography of PA6/OMMT nanocomposites

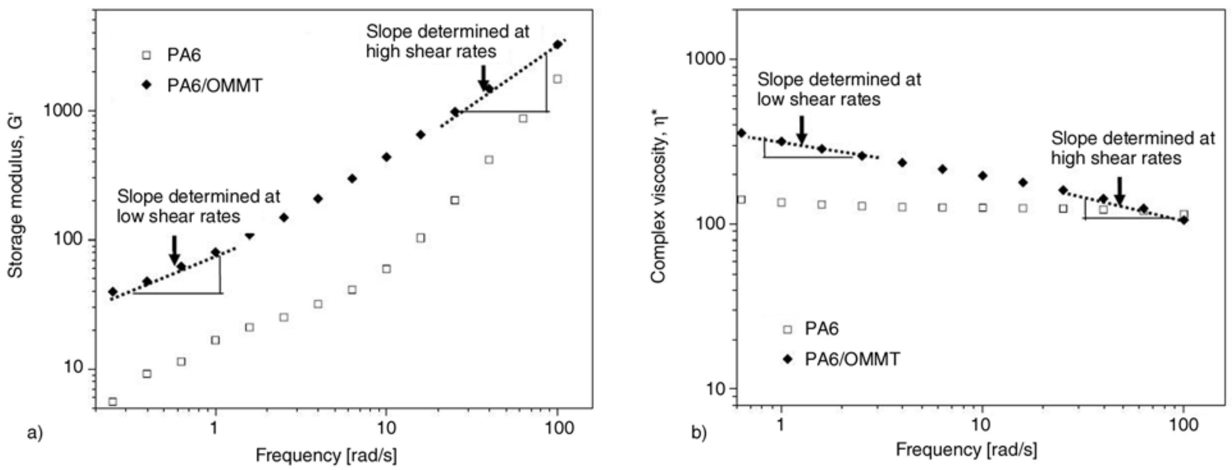

Figure 3. a – Variation in the storage modulus (*G'*) as a function of frequency for PA6 and PA6/OMMT nanocomposites; b – Variation in the complex viscosity (η*) as a function of frequency for PA6 and PA6/OMMT nanocomposites

reflect the effects of clay dispersion. The higher the slope, the less stable the clay is. At lower frequency (at 1 rad/s) the polymer chains are fully relaxed and thus alterations in storage modulus (*G'*) and loss modulus (*G"*) including their slopes are likely linked to the effect of the clay dispersion. This change in slope indicates that the nanocomposites attained a pseudo solid-like behaviour due to the nano-reinforcing effect of the intercalated/exfoliated clay. Similar results were reported by Hoffmann *et al.* [17]. The higher the *G'* moduli and the smaller the slope (at lower frequency), the more pronounced the interaction between the silicate platelets and their tendency to form a three-dimensional superstructure [17]. One can thus concluded that rheological characteristics (*G'* and related slope) in the low frequency viscoelastic range could reflect even small changes in the clay dispersion accordingly.

Figure 3b depicts the course of the complex viscosity (η^*) as a function of frequency for the viscoelastic range assessed by a plate-plate rheometer. Note that the complex viscosity of PA6 increased in the presence of OMMT. The slope values of η^* for PA6 at 1 rad/s and 100 rad/s are –0.04 and –0.13, respectively. However, the slope values of η^* for PA6/OMMT at 1 rad/s and 100 rad/s is –0.46 and –0.29, respectively. According to Boucard *et al.* [18], at low shear rates, the silicate platelets of high aspect ratio are well separated and this strongly increases the viscosity of the melt. On the other hand, at higher shear rates the platelets are oriented in the flow direction which consequently leads to a reduction in the viscosity. One could expect that the higher the viscosity and the higher the negative slope in viscosity-frequency relation are the better is the clay exfoliation. This prediction is due to the fact that intimate clay/polymer interaction is accompanied with strong viscosity increase. However, if the clay layers are well separated from each other (exfoliated stage) then shear thinning is more probable than in case of intercalated tactoids. Recall that shear thinning presumes an alignment of the clay layer in the flow direction which occurs easily in exfoliated stage.

3.4. Thermal analysis

The dynamic storage modulus, as well as the tanδ *versus* temperature traces for the PA6 and PA6/OMMT nanocomposites is shown in Figure 4a&b, respectively. It can be seen that PA6/OMMT nanocomposites exhibits higher storage modulus than PA6 (c.f. Figure 4a). This may again be attributed to the reinforcing effects of the OMMT in PA6 matrix. Figure 4b shows the effect of OMMT on the loss factor (tanδ) for PA6. Two dynamic relaxation peaks were observed at around 56°C and –60°C, which referred to as α and β relaxation peaks of PA6. The α relaxation peak is believed to be related to the breakage of hydrogen bonding between polymer chain which induces long range segmental chain movement in the amorphous area. This is assigned to the glass transition temperature (T_g) of PA6. Note that there is no significant changing in the T_g value of PA6 with the incorporation of OMMT.

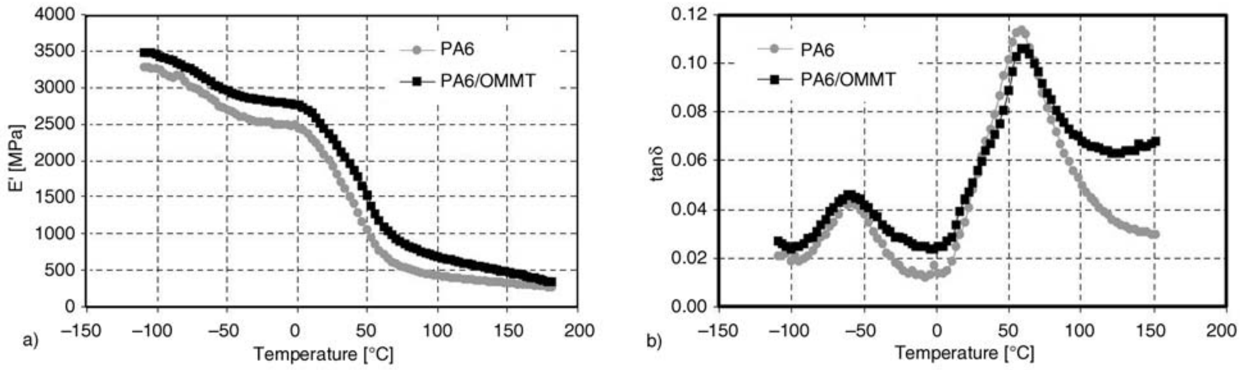

Figure 4. a – *E' vs T* traces for PA6 and PA6/OMMT nanocomposites; b – tanδ *vs T* traces for PA6 and PA6/OMMT nanocomposites

4. Conclusions

Based on this work devoted to study the effects of OMMT on the mechanical, morphological and rheological properties of PA6 nanocomposites, the following conclusions can be drawn:

(a) Modulus and strength of the PA6 was improved significantly in the presence of OMMT attributed to the stiffness, rigidity, reinforcing effects and exfoliation of OMMT.

(b) XRD and AFM techniques could be used to study the morphology of PA6/OMMT nanocomposites. The OMMT was exfoliated in the PA6 matrix. This is attributed to the strong interaction of PA6 and OMMT, and the intercalation capability of PA6 in the silicate layers of OMMT.

(c) Considering the XRD and AFM results of the OMMT dispersion in the PA6 nanocomposites, the following rheological parameters, in the viscoelastic range at low frequency, could be considered as suitable indicators: the storage modulus (*G'*) and its slope, and the complex viscosity (η^*) and its slope. The higher *G'* and the smaller the related slope, as well as the higher η^* and its higher related slope, the better the clay exfoliation is.

Acknowledgments

The authors would like to thank Ministry of Science, Technology and Environment (MOSTE), Malaysia for the IRPA grant and USM Short Term Grant. The authors appreciate the technical support for the AFM, DMTA and rheology tests from Professor Karger-Kocsis (Institute for Composite Materials, Kaiserslautern University of Technology, Germany).

References

[1] Ray S. S., Okamoto M.: Polymer/layered silicate nanocomposites: a review from preparation to processing. Progress in Polymer Science, **28**, 1539–1641 (2003).

[2] Alexandre M., Dubois P.: Polymer-layered silicate nanocomposites: preparation, properties and uses of a new class of materials. Materials Science and Engineering: R: Reports, **28**, 1–63 (2000).

[3] Kojima Y., Usuki A., Kawasumi M., Okada A., Kurauchi T., Kamigaito O.: Synthesis of nylon 6-clay hybrid by montmorillonite intercalated with ε-caprolactam. Journal of Polymer Science Part A-Polymer Chemistry, **31**, 983–986 (1993).

[4] Fornes T. D., Yoon P. J., Keskkula H., Paul D. R.: Nylon 6 nanocomposites: the effect of matrix molecular weight. Polymer, **42**, 9929–9940 (2001).

[5] Cho J. W., Paul D. R.: Nylon 6 nanocomposites by melt compounding. Polymer, **42,** 1083–1094 (2001).

[6] Liu X. H., Wu Q. J., Berglund L. A., Fan J. Q., Qi Z. N.: Polyamide 6-clay nanocomposites/polypropylene-grafted-maleic anhydride alloys. Polymer, **42**, 8235–8239 (2001).

[7] Chiu F. C., Lai S. M., Chen Y. L., Lee T. H.: Investigation on the polyamide 6/organoclay nanocomposites with or without a maleated polyolefin elastomer as a toughener. Polymer, **46**, 11600–11609 (2005).

[8] González I., Eguiazábal J. I., Nazábal J.: Rubber-toughened polyamide 6/clay nanocomposites. Composites Science and Technology, **66**, 1833–1843 (2006).

[9] Karger-Kocsis J., Gryshchuk O., Fröhlich J., Mülhaupt R.: Interpenetrating vinylester/epoxy resins modified with organophilic layered silicates. Composites Science and Technology, **63**, 2045–2054 (2003).

[10] Chow W. S., Mohd Ishak Z. A., Karger-Kocsis J.: Atomic force microscopy study on blend morphology and clay dispersion in polyamide-6/polypropylene/organoclay systems. Journal of Polymer Science Part B-Polymer Physics, **43**, 1198– 1204 (2005).

[11] Krishnamoorti R., Yurekli K.: Rheology of polymer layered silicate nanocomposites. Current Opinion in Colloid and Interface Science, **6**, 464–470 (2001).

[12] Reichert P., Nitz H., Klinke S., Brandsch R., Thomann R., Mülhaupt R.: Poly(propylene)/organoclay nanocomposite formation: Influence of compatibilizer functionality and organoclay modification. Macromolecular Materials Engineering, **275**, 8–17 (2000).

[13] Shelley J. S., Mather P. T., DeVries K. L.: Reinforcement and environmental degradation of nylon-6/clay nanocomposites. Polymer, **42**, 5849–5858 (2001).

[14] Huang J. C., Zhu Z. K., Ma X. D., Qian X. F., Yin J.: Preparation and properties of montmorillonite/organo-soluble polyimide hybrid materials prepared by a one-step approach. Journal of Materials Science, **36**, 871–877 (2001).

[15] Wu Z. G., Zhou C. X., Qi R. R., Zhang H. B.: Synthesis and characterization of nylon 1012/clay nanocomposites. Journal of Applied Polymer Science, **83**, 2403–2410 (2002).

[16] Li J., Zhou C. X., Wang G., Zhao D. L.: Study on kinetics of polymer melt intercalation by a rheological approach. Journal of Applied Polymer Science, **89**, 318–323 (2003).

[17] Hoffmann B., Kressler J., Stöppelmann G., Friedrich C., Kim G. M.: Rheology of nanocomposites based on layered silicates and polyamide-12. Colloid and Polymer Science, **278**, 629–636 (2000).

[18] Boucard S., Duchet J., Gérard J. F., Prele P., Gonzalez S.: Processing of polypropylene-clay hybrids. Macromolecular Symposia, **194**, 241–246 (2003).

eXPRESS Polymer Letters Vol.1, No.2 (2007) 84–91
Available online at www.expresspolymlett.com
DOI: 10.3144/expresspolymlett.2007.15

Relationship between constant strain rate and stress relaxation behavior of polypropylene

P. Nagy[*], *L. M. Vas*

Department of Polymer Engineering, Budapest University of Technology and Economics, H-1111 Budapest, Hungary

Received 5 December 2006; accepted in revised form 19 January 2007

Abstract. A new method based on variable transformation is proposed for the estimation of the constant strain rate tensile test by using a previously introduced concept of viscoelastic response given to the real relaxation stimulus.
The time range of the 'good' fitting is 2.5 to 3 times larger than the best results achieved using linear viscoelastic approximations. The theoretical background of the method was elucidated as well.

Keywords: *mechanical properties, viscoelasticity, stress relaxation, tensile test, polypropylene*

1. Introduction

The mechanical response of real polymers are basically of nonlinear character, therefore their behavior patterns do not meet the idealized (linear) ones, especially in case of large loads. Nevertheless, linear viscoelasticity is often used successfully for describing the real behavior in case of small or moderate loads. The use of thermoplastics in structural applications demands accurate design data that spans appropriate ranges of stress, strain rate, time and temperature. A number of theoretical and experimental studies [1–4] have mainly dealt with the investigation of the relaxation or creep phenomena and in some cases with the relationships between the results of different tests in order to estimate or predict the short and long term behavior of polymers under different conditions. Some researchers use molecular dynamics calculations [5–7] to study the stress-strain behavior but the phenomenological or semi-phenomenological approach is more widespread [9–16]. The stress relaxation behavior of polymer materials has been studied in several theoretical and experimental investigations such as those by Urzumtsev and Maksimov [9], Retting [10], Wortmann and Shultz [13], Andreassen [14], as well as Baeurle *et al.* [15]. Sudduth [2] have dealt with the relationships between creep, stress relaxation and constant strain rate data. Grzywinski and Woodford [3] predicted the creep behavior from constant stress rate tensile experiments.

In accordance with the usual loading modes the most frequently used quasi-static mechanical tests are the constant strain rate tensile, the creep, and the stress relaxation ones. Among them the tensile test lasts for the shortest time and provides an increasing load up to the damage or fracture of the specimen. During the tensile test the specimen, so to say, lives its life to the very end in an accelerated way, consequently this test may give a lot of information about the material and its mechanical behavior for various loading modes. Therefore, it may be expected that from a tensile test the behavior for the medium or long term relaxation or creep and *vice versa* can be predicted. In [10] Retting summarized his method and experimental results on the estimation of the real stress relaxation function as the product of the linear response and a

---

[*]Corresponding author, e-mail: nagy@pt.bme.hu

strain dependent factor. The tensile load curve is estimated as the time integral of the stress relaxation curve in accordance with the linear viscoelastic theory.

In this paper a new method is proposed for the estimation of the real tensile load response by using the viscoelastic response given to the real relaxation stimulus. This method can be considered as the solution of the inverse problem to estimate the (long term) stress relaxation function from the (short term) tensile test. Solving this inverse problem is mathematically somewhat less complicated and facilitates the finding of the proper functions for the direct problem. This method is completely different from the one previously published in [16] where a simple function with three adjustable parameters was used, while here a more sophisticated variable transformation method is elaborated to realize the nonlinear behavior. Variable transformations are successfully used for example in the mathematical formulation of time-temperature correspondence (the WLF Equation) [8].

2. Experimental procedure

Isotactic polypropylene homopolymer (Tipplen H 543 F from TVK, Hungary) having a Melt Flow Index (MFI, 2.16 kg/230°C) of 4 g/10 min was used for the tests. Dumbbell specimens were injection molded according to ISO 294-2 Standard on an Arburg Allrounder 320 C 600-250 injection molding machine of specimen length 148 mm, width 10 mm and thickness 4 mm. Uniaxial tensile stress relaxation tests were performed on a Zwick Z005 tensile testing machine. The tensile force was measured by a 5 kN nominal capacity standard load cell.

Tensile tests were performed on 5 test specimens with crosshead speed of 5 mm/min at room temperature. For the relaxation tests specimens were stretched up to 0.08, 0.16, 0.24, 0.50, 0.75 and 1.00% engineering strains (ε_0) with crosshead speed (v) of 5 mm/min. No necking of specimens was observed in the relaxation tests. Every test was performed on a new specimen. The engineering yield strain was calculated from the crosshead displacement as $\varepsilon_0 = \Delta l/l_0$ where l_0 is the gauge length at time 0 and $l_0 = 110$ mm. On the basis of these considerations the strain rate was $\dot{\varepsilon}_0 = v/l_0 = 0.0455$/min = 4.55%/min in each case. We are aware that there are more precise methods – like strain gages or contactless CCD camera + image processing – for the strain measurements, but in this work we wanted only to demonstrate the applicability of our global approach as a predictive method and for this purpose any measured strain value is suitable.

3. Theoretical background

Figure 1 shows the general scheme of mechanical tests where S is the specimen as a black box system, X is the input stimulus and Y is the response of the specimen. The two latter are time-functions.

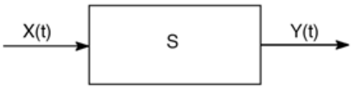

Figure 1. General scheme of mechanical tests [16]

If S is an operator characterizing the material, that is the specimen, the response can be obtained as follows:

$$Y(t) = S[X](t) \tag{1}$$

In Equation (1) input $X(t)$ and output $Y(t)$ signals can be the stress and strain or *vice versa*, and S is an operator characterizing the material. In tensile tests usually the force-time ($F(t)$) and elongation-time ($\Delta l(t)$) curves are recorded instead of stress-strain curves, so it is more natural to make the further calculations in terms of $F(t)$ and $\Delta l(t)$. The relationship between force (F) and stress (σ) and elongation (Δl) and strain (ε) is the following:

$$F(t) = A_0\sigma(t) \tag{2}$$

$$\Delta l(t) = l_0\varepsilon(t) \tag{3}$$

where A_0 and l_0 are the cross-sectional area and gauge length of the unloaded specimen, respectively.

Figure 2 shows the measured and estimated force-time curves, the relations between them and the used notations for a constant strain-rate tensile experiment as well as for a stress relaxation experiment in which a real stimulus (namely, constant strain-rate) is applied. From Equation (1) it follows for the latter:

$$F_1(t) = S[\Delta l_1](t) \tag{4}$$

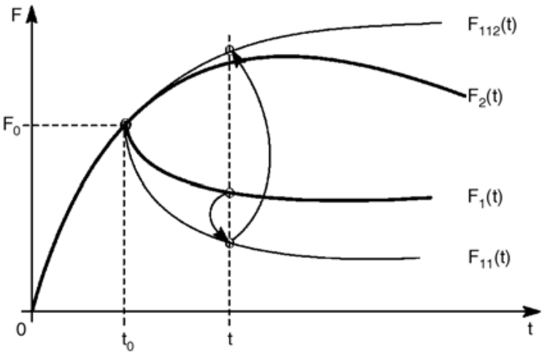

Figure 2. Measured and estimated *force-time* curves. $F_2(t)$: measured force in a tensile test experiment; $F_1(t)$: measured force in a stress relaxation experiment; $F_{11}(t)$: force estimated from $F_1(t)$ in such way that it approximates correctly the derivative of the stress-strain curve ($F_2(t)$) in a possibly wide range; $F_{112}(t)$: force estimated from $F_{11}(t)$; F_0 and t_0: force and time, respectively, at the beginning of the stress relaxation experiment

Similar expressions represent the relationship between $F_1(t)$ and $F_{11}(t)$, $F_{112}(t)$ and $F_{11}(t)$ and $F_2(t)$ and $\Delta l_2(t)$:

$$F_{11}(t) = S_1[F_1](t) \rightarrow$$
$$F_{112}(t) = S_2[F_{11}](t) \approx F_2(t) = S[\Delta l_2](t) \tag{5}$$

where S_1 is a nonlinear estimating operator and S_2 is a linear estimating operator (see [16] for details). The linear mapping operator S_2 can be represented by the following recursive equation:

$$F_{112}(t) = F_{112}(t–t_0) + F_{11}(t) \tag{6}$$

The unknown operator S_1: $F_1 \rightarrow F_{11}$ is to be chosen so that estimation $F_{112}(t)$ provides an acceptable accuracy in a given time range. It is obvious that F_1 and F_{11} are similar to each other regarding the fact that they both must have the properties of a stress relaxation function (Figure 2). First of all, the initial values are identical:

$$F_{11}(t_0) = F_1(t_0) = F_0 \tag{7}$$

They must be monotonously decreasing that is:

$$\frac{\mathrm{d}F_1}{\mathrm{d}t} < 0, \frac{\mathrm{d}F_{11}}{\mathrm{d}t} < 0, t > t_0 \tag{8}$$

and specially:

$$\dot{F}_0 = \frac{\mathrm{d}F_{11}}{\mathrm{d}t}(+t_0) < \dot{F}_{10} = \frac{\mathrm{d}F_1}{\mathrm{d}t}(+t_0) < 0 \tag{9}$$

At the same time they must be convex from below:

$$\frac{\mathrm{d}^2 F_{11}}{\mathrm{d}t^2} > 0, \frac{\mathrm{d}^2 F_1}{\mathrm{d}t^2} > 0, t > t_0 \tag{10}$$

as well as finally they – in normal cases – have to tend to a nonnegative finite value ($F_{1\infty}$, F_∞):

$$F_1(t) \rightarrow F_{1\infty} \geq 0, t \rightarrow \infty$$
$$F_{11}(t) \rightarrow F_\infty \geq 0, t \rightarrow \infty \tag{11}$$

where

$$0 \leq F_\infty < F_{1\infty} < F_0 \tag{12}$$

On the basis of Equation (10) F_1 and F_{11} are twice continuously differentiable the set of which is denoted by $C_2 = C_2(t_0,\infty)$. Let us denote the set of the functions meeting the condition formulated above – except for Equation (9) – by $C_2^* = C_2^*(t_0,\infty) \subset C_2$. In this case operator S_1 can be given as a mapping as follows:

$$S_1 : C_2^*(t_0,\infty) \rightarrow C_2^*(t_0,\infty) \tag{13}$$

and it can be represented for example by an integral using Equation (5) and (7):

$$F_{11}(t) = S_1[F_1](t) = F_0 - \int_{t_0}^{t} G(t,u,f_1(u))\mathrm{d}f_1(u) \tag{14}$$

where G is a core-function characterizing the nonlinearity of the material and

$$f_1(t) = F_1(t_0) – F_1(t) = F_0 – F_1(t) \tag{15}$$

In a special case applied in this paper as an example, if G is explicitly independent of variables t and u operator S_{11} can be simply represented by a function (g) in the following form:

$$F_{11}(t) = F_1(t) – g(f_1(t))$$
$$g(f_1) = \int_0^{f_1} G(x)\mathrm{d}x \tag{16}$$

which must meet the requirements Equation (7)–(12) from which the following conditions for function $g(f_1) \geq 0$ can be derived for $t \geq t_0$:

$$F_{11}(t_0) = F_{11}(t_0) – g(f_1(t_0)) = F_1(t_0) = F_0 \Rightarrow$$
$$g(0) = 0 \tag{17}$$

$$\frac{\mathrm{d}F_{11}}{\mathrm{d}t} = -\frac{\mathrm{d}g}{\mathrm{d}f_1}\left(-\frac{\mathrm{d}F_1}{\mathrm{d}t}\right) < 0 \Rightarrow \frac{\mathrm{d}g}{\mathrm{d}f_1} > 0 \tag{18}$$

$$\dot{F}_0 = \frac{\mathrm{d}F_{11}}{\mathrm{d}t}(+t_0) = \left.\frac{\mathrm{d}g}{\mathrm{d}f_1}\right|_{+t_0} \left.\frac{\mathrm{d}F_1}{\mathrm{d}t}\right|_{+t_0} < \dot{F}_{10} < 0$$

$$\Rightarrow \left.\frac{\mathrm{d}g}{\mathrm{d}f_1}\right|_{+t_0} > 1 \tag{19}$$

$$\frac{\mathrm{d}^2F_{11}}{\mathrm{d}t^2} = \frac{\mathrm{d}^2g}{\mathrm{d}f_1^2}\left(\frac{\mathrm{d}F_1}{\mathrm{d}t}\right)^2 + \frac{\mathrm{d}g}{\mathrm{d}f_1}\frac{\mathrm{d}^2F_1}{\mathrm{d}t^2} > 0 \Rightarrow$$

$$-\frac{\mathrm{d}^2g}{\mathrm{d}f_1^2} < \frac{\mathrm{d}g}{\mathrm{d}f_1}\frac{\frac{\mathrm{d}^2F_1}{\mathrm{d}t^2}}{\left(\frac{\mathrm{d}F_1}{\mathrm{d}t}\right)^2} \tag{20}$$

$F_{11}(t) = F_0 - g(F_0 - F_1(t)) \rightarrow F_0 - g(F_0 - F_{1\infty}) =$
$F_\infty \geq 0,\ t \rightarrow \infty \Rightarrow$
$0 < F_0 - F_{1\infty} < g(F_0 - F_{1\infty}) = F_0 - F_\infty < F_0$ (21)

It is notable that inequality (20) is trivially fulfilled if

$$\frac{\mathrm{d}^2g}{\mathrm{d}f_1^2} > 0 \tag{22}$$

In [16] a special $g(t)$ function was used. Another possibility of describing operator S_1 is the application of variable transformations for example in the following form:

$F_{11}(t) = S_1[F_1](t) =$
$F_0 - b[F_0 - F_1(t_0 + (t - t_0)a(t))]$ (23)

where – to a certain degree similarly to the WLF Equation [5, 6] – $a(t) \geq 0$ is a kind of delay-function and b is a constant. Introducing the following notation:

$$h(t) = t_0 - (t - t_0)a(t) \tag{24}$$

let us suppose that

$$h(t) \rightarrow \infty \Rightarrow,\ t \rightarrow \infty \tag{25}$$

On the basis of Equation (11) and (25) the value of b can be obtained easily:

$$b = \frac{F_0 - F_\infty}{F_0 - F_{1\infty}} > 1 \tag{26}$$

and applying Equation (8)–(10) provides some other information about function $a(t)$:

$$\frac{\mathrm{d}F_{11}}{\mathrm{d}t} = -b\left(-\frac{\mathrm{d}F_1}{\mathrm{d}h}\right)\frac{\mathrm{d}h}{\mathrm{d}t} < 0 \Rightarrow$$

$$\frac{\mathrm{d}h}{\mathrm{d}t} = a(t) + (t - t_0)\frac{\mathrm{d}a}{\mathrm{d}t} > 0 \Rightarrow$$

$$\frac{\mathrm{d}a}{\mathrm{d}t} > -\frac{a(t)}{t - t_0} \tag{27}$$

$$\frac{\mathrm{d}F_{11}}{\mathrm{d}t}(+t_0) < \frac{\mathrm{d}F_1}{\mathrm{d}t}(+t_0) < 0 \Rightarrow$$

$$\left.\frac{\mathrm{d}h}{\mathrm{d}t}\right|_{+t_0} > \frac{1}{b} \Rightarrow a(t_0) > \frac{1}{b} \tag{28}$$

$$\frac{\mathrm{d}^2F_{11}}{\mathrm{d}t^2} = b\frac{\mathrm{d}^2F_1}{\mathrm{d}h^2}\left[\frac{\mathrm{d}h}{\mathrm{d}t}\right]^2 + b\frac{\mathrm{d}F_1}{\mathrm{d}t}\frac{\mathrm{d}^2h}{\mathrm{d}t^2} > 0 \Rightarrow$$

$$\frac{\mathrm{d}^2h}{\mathrm{d}t^2} > -\left[\frac{\mathrm{d}h}{\mathrm{d}t}\right]^2 \frac{\frac{\mathrm{d}^2F_1}{\mathrm{d}h^2}}{\frac{\mathrm{d}F_1}{\mathrm{d}h}} > 0 \tag{29}$$

In case of linear viscoelasticity S_1 is the identical operator hence $g(f_1) \equiv f_1$ in Equation (16) and $a = 1$, $b = 1$ in Equation (23).

It is obvious that a stress relaxation response function of a Standard-Solid model (F_{SS}) [5] fulfils conditions for F_1 or F_{11} therefore $F_{SS} \in C_2^*$ that is why it can be well applied as a simple test function for both F_1 and F_{11} ($t \geq t_0$):

$$F_1(t) = F_{1\infty} + (F_0 - F_{1\infty})\mathrm{e}^{-\frac{t-t_0}{\tau_1}}$$
$$F_{11}(t) = F_\infty + (F_0 - F_\infty)\mathrm{e}^{-\frac{t-t_0}{\tau_2}} \tag{30}$$

where in accordance with Equation (9) $\tau_2 < \tau_1$.

The mapping (g) according to Equation (16) can be calculated easily by expressing t from $F_1(t)$ and substituting that into $F_{11}(t)$:

$$F_{11}(t) = F_\infty + (F_0 - F_\infty)\left[\frac{F_1(t) - F_{1\infty}}{F_0 - F_{1\infty}}\right]^{\frac{\tau_1}{\tau_2}} =$$
$$F_0 - (F_0 - F_\infty)\left(1 - \left[1 - \frac{F_0 - F_1(t)}{F_0 - F_{1\infty}}\right]^{\frac{\tau_1}{\tau_2}}\right) \tag{31}$$

from which function g can be determined:

$$g(f_1) = (F_0 - F_\infty)\left(1 - \left[1 - \frac{f_1(t)}{F_0 - F_{1\infty}}\right]^{\frac{\tau_1}{\tau_2}}\right) \tag{32}$$

According to Equation (33) function g is nonlinear if $\tau_2 \neq \tau_1$.

The mapping according to Equation (23) can be tested similarly. If $a = \tau_1/\tau_2$ then Equation (23) produces the mapping between the F_1 and F_{11} of exponential form (30):

$$F_{11}(t) = S_1[F_1](t) =$$
$$F_0 - \frac{F_0 - F_\infty}{F_0 - F_{1\infty}}\left[F_0 - F_1\left(t_0 - (t - t_0)\frac{\tau_1}{\tau_2}\right)\right] \quad (33)$$

In case of simple exponential relaxation functions mapping 'g' according to Equation (32) much more complicated than that of function 'a' which is a constant.

It is well known that the real relaxation functions can be well approximated the response of a generalized Standard Solid model [5] which is a sum of exponential functions such as according to Equation (30):

$$F_1(t) = F_{1\infty} + (F_0 - F_{1\infty})\sum_{i=1}^{n}\alpha_i\, e^{-\frac{t-t_0}{\tau_{1i}}}$$
$$F_{11}(t) = F_\infty + (F_0 - F_\infty)\sum_{i=1}^{n}\alpha_i\, e^{-\frac{t-t_0}{\tau_{2i}}} \quad (34)$$

where n is the number of the Maxwell branches in the model and α_i ($i = 1, \ldots, n$) are weighting factors:

$$\sum_{i=1}^{n}\alpha_i = 1 \quad (35)$$

It is easy to see that Equation (33) realizes a correct mapping between functions according to Equation (34) as well if $a = \tau_1/\tau_2$ by transforming the parameters as follows:

$$F_{1\infty} \rightarrow F_\infty$$
$$\tau_{1i} \rightarrow \tau_{2i} = \tau_{1i}/a$$
$$\alpha_i \rightarrow \alpha_i \quad (36)$$

Unfortunately, this is not true for mapping Equation (31) because instead of the form according to Equation (34) it gives another form such as (using 'a' instead of τ_1/τ_2):

$$F_{11}(t) = F_\infty + (F_0 - F_\infty)\left[\sum_{i=1}^{n}\alpha_i\, e^{-\frac{t-t_0}{\tau_{1i}}}\right]^a \quad (37)$$

On the basis of all these considerations and the fact that the real relaxation curves can be well approximated by the functions of type according to Equation (34) it may be supposed that mapping Equation (33) can be used for transforming the results of relaxation measurements as well.

4. Fitting of the observations

For the estimation of $F_2(t)$, the force-time curve of a tensile test, we start from $F_1(t)$, the measured force-time curve of the stress relaxation experiment (see Figure 2). First we perform a transformation of time, t:

$$t' = h(t) \quad (38)$$

where $h(t)$ is a function to be determined. This function should make the following mapping of the time axis:

$$h:[0,t_s) \mapsto [0, \infty) \quad (39)$$

where t_s is the time corresponding to the yield or ultimate elongation in the tensile test. Figure 3 shows the general appearance of $h(t)$.

In the next step we calculate from $F_1(t)$ a transformed force-time curve, $F_1(t') = F_1(h(t))$.

$F_{11}(t)$ can be calculated according to Equation (23) in the following manner:

$$F_{11}(t) = F_0 - b\,[F_0 - F_1(h(t))] \quad (40)$$

In the last step $F_{112}(t)$, the estimate of the tensile load-time curve ($F_2(t)$) is calculated from $F_{11}(t)$ according to the recursive formula of Equation (6). The parameters of the mapping function $h(t)$ as well as b are estimated by fitting $F_{112}(t)$ to $F_2(t)$. Because the resulting equations are usually non-lin-

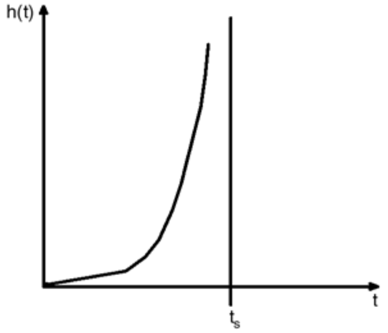

Figure 3. General appearance of $h(t)$

ear for the parameters, numerical procedures should be used.

We have tested the performance of our model by some simple functions that satisfy Equation (39):

$$h1(t) = t_0 + a(t_s - t_0)\left[\frac{t - t_0}{t_s - t}\right]^c \tag{41}$$

$$h2(t) = t_0 + a(t - t_0)^k \exp\left(\frac{c}{t_s - t}\right) \tag{42}$$

$$h3(t) = t_0 + a\frac{(t_s - t_0)(t - t_0)}{t_s - t}\left(1 + \frac{t_s - t_0}{t_1 - t_0}\right)^c \tag{43}$$

$$h4(t) = t_0 + \left[\tan\left(\frac{t - t_0}{t_s - t_0}\right)\right]^c \tag{44}$$

where t_0 is the time corresponding to the beginning of the stress relaxation experiment (Figure 2), t_s is the time corresponding to the yield or ultimate elongation in the tensile test, and a, c, k, and t_1 are adjustable parameters. Figure 4 to 7 summarizes the results for $h1(t)$ to $h4(t)$.

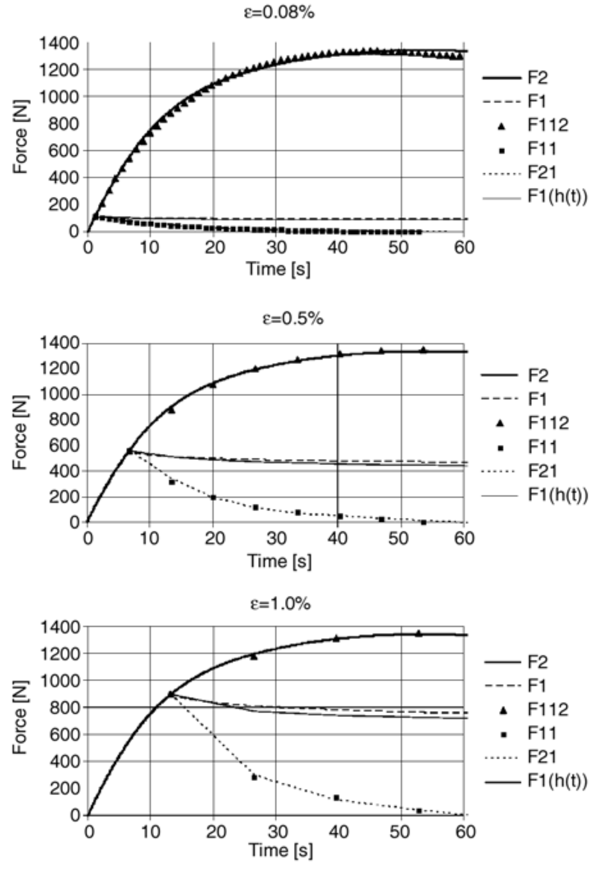

Figure 4. Measured and estimated force-time curves for 3 different initial strains. $h(t) = h1(t)$

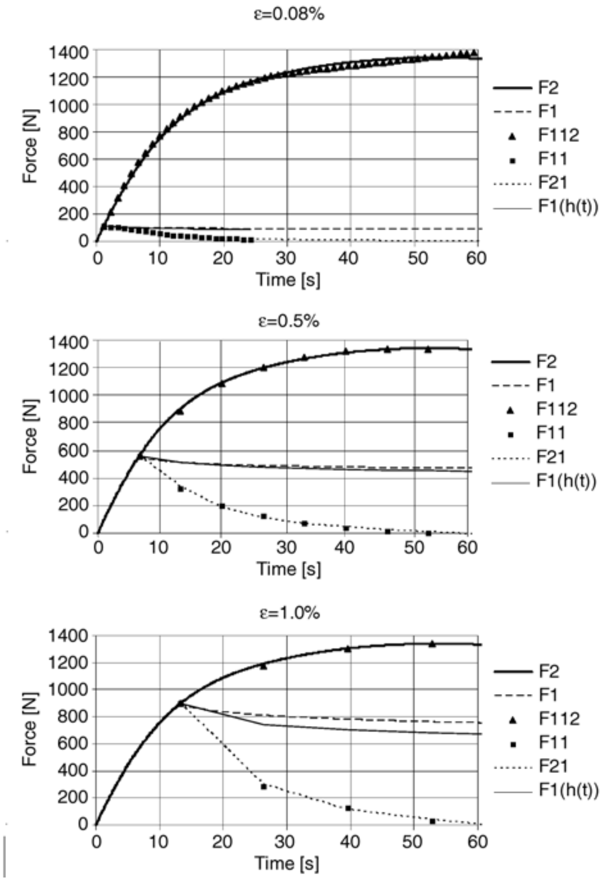

Figure 5. Measured and estimated force-time curves for 3 different initial strains. $h(t) = h2(t)$

5. Discussion

As it can be seen from Figure 4–7 there is a fair agreement between the force-time curve (F_2) measured in constant strain rate tensile test and its nonlinear viscoelastic approximation, F_{112}, in a relatively wide time and initial strain (ε) range, concerning the duration of a tensile test. The time range (between 50 and 60 s for the $h(t)$-s tested) of the 'good' fitting is 2.5 to 3 times larger than the best results found for linear viscoelastic approximations (20–22 s, see [16]). Table 1 summarizes the goodness of approximation calculated in the time range tested as

$$R^2 = 1 - \frac{\sum (y_i - \hat{y}_i)^2}{\sum (y_i - \bar{y}_i)^2} \tag{45}$$

where y_i is the i-th measured value, $\hat{y}$ is its approximation and is the mean of the measured values. The best results for all initial strain (ε) ranges were achieved by $h2(t)$, an exponential function.

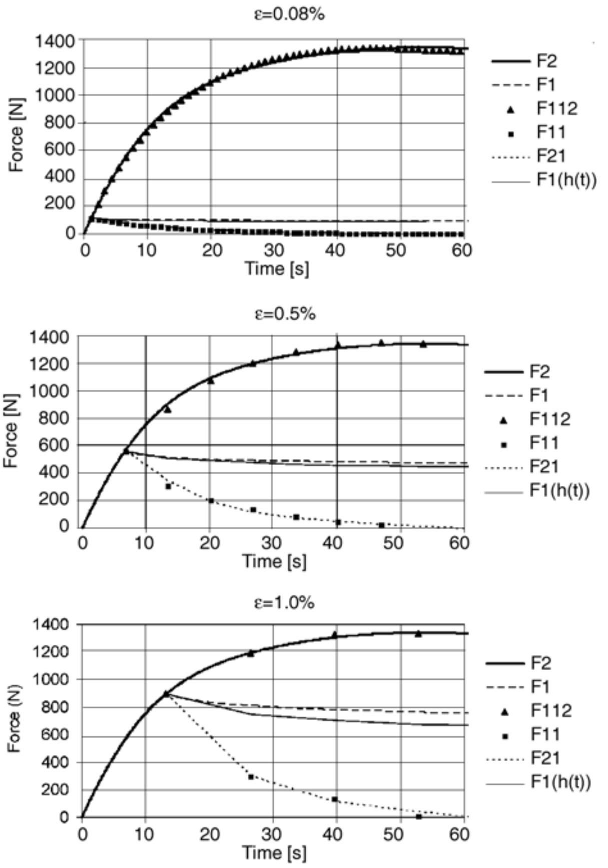

Figure 6. Measured and estimated force-time curves for 3 different initial strains. $h(t) = h3(t)$

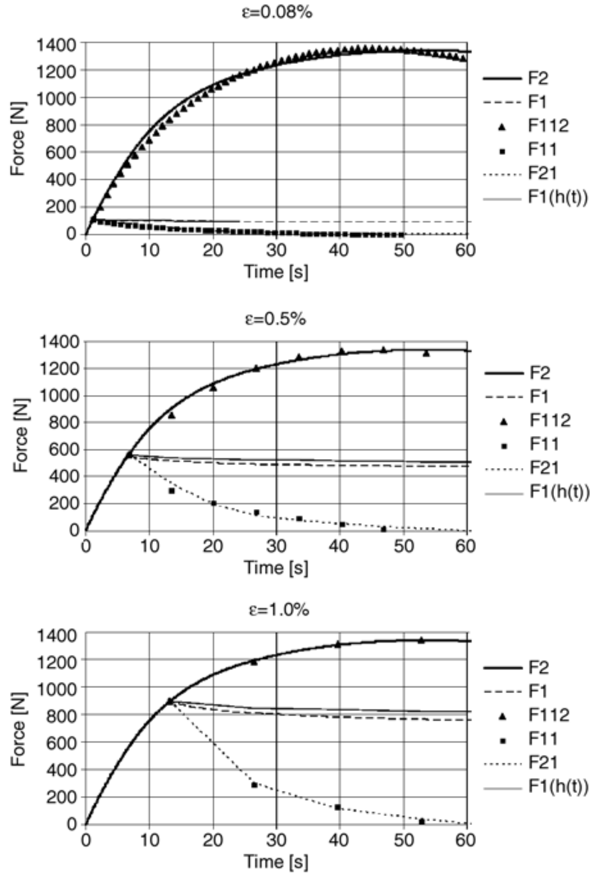

Figure 7. Measured and estimated force-time curves for 3 different initial strains. $h(t) = h4(t)$

Table 1. Goodness of fit (R^2) values for the four h(t) functions

Initial strain (ε) [%]	h1(t)	h2(t)	h3(t)	h4(t)
0.08	0.9984	0.9994	0.992	0.9932
0.5	0.9676	0.9952	0.9693	0.9280
1.0	0.9892	0.9739	0.9627	0.9919

6. Conclusions

We have shown that the force-time curve of the constant strain rate tensile test can be modeled using the results of the stress relaxation experiment for a semicrystalline polypropylene material. Good results were achieved by using variable transformation as the mapping operation, especially in the case of an exponential function, $h2(t)$. In our next paper we will show how the inverse problem – modeling of the stress relaxation function from the measured constant strain rate tensile test – can be solved.

Acknowledgements

The authors would like to thank the OTKA Contract No. T049069 for the support of this research.

References

[1] Sudduth R. D.: Development of a simplified relationship between uniaxial creep, stress relaxation, and constant strain-rate results for viscoelastic polymeric materials. Journal of Applied Polymer Science, **82**, 527–540 (2001).

[2] Sudduth R. D.: Comparison of the viscous and elastic components of two ABS materials with creep, stress relaxation and constant strain rate measurements using the universal viscoelastic model. Journal of Applied Polymer Science, **90**, 1298–1318 (2003).

[3] Grzywinski G. G., Woodford D. A.: Creep analysis of thermoplastics using stress relaxation data. Polymer Engineering and Science, **35**, 1931–1937 (1995).

[4] Karger-Kocsis J., Czigány T., Moskala E. J.: Deformation rate dependence of the essential and non-essential work of fracture parameters in an amorphous copolyester. Polymer, **39**, 3939–3944 (1998).

[5] Baeurle S. A., Usami T., Gusev A. A.: A new multiscale approach for the prediction of mechanical properties of polymer-based nanomaterials. Polymer, **47**, 8604–8617 (2006).

[6] Aoyagi T., Honda T., Doi M.: Microstructural study of mechanical properties of the ABA triblock copolymer using self-consistent field and molecular dynamics. Journal of Chemical Physics, **117**, 8153–8161 (2002).

[7] Terzis A. F., Theodorou D. N., Stroeks A.: Entanglement network of the polypropylene/polyamide interface. 3. Deformation to fracture. Macromolecules, **35**, 508– 521 (2002).

[8] Ferry J. D.: Viscoelastic properties of polymers. Wiley and Sons, New York (1980).

[9] Urzumtsev Yu. S., Maksimov R. D.: Deformation of Plastics, Prognostics on the Basis of Similarity Principles (in Hungarian). Műszaki Könyvkiadó, Budapest (1982).

[10] Retting W.: Mechanik der Kunststoffe. Hanser Verlag, München (1992).

[11] Drozdov A. D., Agarwal S., Gupta R. K.: Linear thermo-viscoelasticity of isotactic polypropylene. Computational Materials Science, **29**, 195–213 (2004).

[12] Drozdov A. D., Gupta R. K.: Non-linear viscoelasticity and viscoplasticity of isotactic polypropylene. International Journal of Engineering Science, **41**, 2335–2361 (2003)

[13] Wortmann F. J., Shultz K. V.: Stress relaxation and time/temperature superposition of polypropylene fibres. Polymer, **36**, 315–321 (1995).

[14] Andreassen E.: Stress relaxation of polypropylene fibres with various morphologies. Polymer, **40**, 3909–3918 (1999).

[15] Baeurle S. A., Hotta A., Gusev A. A.: A new semi-phenomenological approach to predict the stress relaxation behavior of thermoplastic elastomers. Polymer, **46**, 4344–4354 (2005).

[16] Vas L. M., Nagy P.: Investigating the time dependent behavior of thermoplastic polymers under tensile load. Macromolecular Symposia, **239**, 176–181 (2006).

eXPRESS Polymer Letters Vol.1, No.2 (2007) 92–97
Available online at www.expresspolymlett.com
DOI: 10.3144/expresspolymlett.2007.16

On the sensitivity of dimensional stability of high density polyethylene on heating rate

A. Zehtabeyazdi[1], *S. M. Zebarjad*[1*], *S. A. Sajjadi*[1], *J. Abolfazli Esfahani*[2]

[1]Department of Materials Engineering, Engineering Faculty, Ferdowsi University of Mashhad, Mashhad, Iran, P. O. Box 91775-1111.
[2]Department of Mechanical Engineering, Engineering Faculty, Ferdowsi University of Mashhad, Mashhad, Iran, P. O. Box 91775-1111.

Received 27 November 2006; accepted in revised form 13 January 2007

Abstract. Although high density polyethylene (HDPE) is one of the most widely used industrial polymers, its application compared to its potential has been limited because of its low dimensional stability particularly at high temperature. Dilatometry test is considered as a method for examining thermal dimensional stability (TDS) of the material. In spite of the importance of simulation of TDS of HDPE during dilatometry test it has not been paid attention by other investigators. Thus the main goal of this research is concentrated on simulation of TDS of HDPE. Also it has been tried to validate the simulation results and practical experiments. For this purpose the standard dilatometry test was done on the HDPE specimens. Secant coefficient of linear thermal expansion was computed from the test. Then by considering boundary conditions and material properties, dilatometry test has been simulated at different heating rates and the thermal strain versus temperature was calculated. The results showed that the simulation results and practical experiments were very close together.

Keywords: *thermal properties, simulation, dilatometry, HDPE, coefficient of linear thermal expansion*

1. Introduction

High density polyethylene (HDPE) is the most widely used polyolefin polymers because of its moderate strength, low cost, excellent processability and high chemical resistance [1]. It can be used in many applications such as automotive, transportation, packing, petrochemical and oil industries. For example nowadays the use of HDPE pipes in petrochemical, oil and gas industries is very common [2]. Although HDPE parts are present in all industries its application has been constrained because of its low dimensional stability particularly at high temperature. Like other thermoplastic polymers it can not tolerate high temperature for a long time. According to literature there are two main methods to evaluate its tolerance at high temperature, the so called dimensional and thermal stability [3–7].

Dimensional stability of a material can be dictated by its coefficient of thermal expansion (CTE). There are two expressions of this quantity which first is volume (α_v) and the latter is linear (α_L) coefficient of thermal expansion. For isotropic materials $\alpha_v = 3\alpha_L$ approximately. Coefficient of linear thermal expansion (CLTE) is a material property that is indicative of material expansion upon heating. [8]. There are two familiar methods to determine CTE of the material. In fact the exact definition depends on the range of studied temperature. If it is achieved at a specific temperature it can be called true coefficient of thermal expansion or α_t. But sometimes it is preferred to measure ther-

---

[*]Corresponding author, e-mail: zebarjad@um.ac.ir

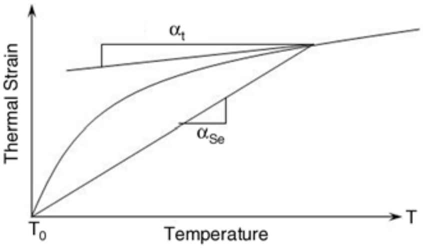

Figure 1. True and Secant coefficient of thermal expansion

mal expansion over a temperature range which is called secant coefficient of thermal expansion (SCTE) or α_{se}. The true coefficient is related to the slope of the length versus temperature, while the secant coefficient is determined by the slope of the chord between two points on the curve (Figure 1).

The magnitude of CTE based on true and secant can be obtained using Equation (1) and (2), respectively [9]:

$$\alpha_{se} = \frac{L - L_0}{L_0(T - T_0)} \tag{1}$$

$$\alpha_t = \frac{\mathrm{d}L}{L\mathrm{d}T} \tag{2}$$

where L is the length at T, T_0 is the initial temperature (25°C in this work) and L_0 is the length at T_0 (zero thermal strain). Also, Thermal strain due to length change can be calculated using Equation (3):

$$\varepsilon_{th} = \alpha_{se}(T - T_0) \tag{3}$$

CTE can be calculated using both theoretical and experimental methods. There are many papers concentrating on the calculation of thermal expansion using theoretical methods [10–12]. For example Garai [11] found a correlation between heat capacity and volume coefficient of thermal expansion of highly symmetrical monatomic arrangements for some metals. Furthermore, thermal expansion coefficient of crystalline polymers has been predicted by Kardos *et al.* [10]. The approach was based on the assumption that a crystalline polymer can be descirbed as a multi-ply laminated composite. The results of their calculations showed a good agreement between theoretical and experimental data of an isotropic sheet of quenched HDPE.

Like theoretical methods there are many studies focused on CTE of polymers experimentally [13–20]. The base of almost all papers was dependency of length change on temperature. Simha *et al.* [16] evaluated thermal expansivities at low temperature on a series of polymer blends over the whole range of composition from pure polyethylene to pure polypropylene. Brillhart *et al.* [17] studied the thermal expansion of a kind of polyamide using wide-angle x-ray scattering (WAXS) method from 25°C to 325°C. Jayanna and Subramanyam [18] examined thermal expansion of irradiated polyethylene from 10 to 340 K by using the three-terminal capacitance technique and it was found that the CTE was constant at radiation varies from 10 to 110 K and decreased as radiation increased up to 340 K.

In spite of importance of heating rate on dimensional stability and SCTE of HDPE, there are a few papers concentrated on it. Therefore, in this paper it is tried to elucidate the role of both heating rate and temperature on dimensional stability and SCTE of HDPE. Also, it will be an attempt to simulate of system to clarify the dependency of SCTE on both heating rate and temperature.

2. Experiments

2.1. Sample preparation

In order to evaluate the thermal expansion behavior of HDPE, one of polymer by the trade name of Eltex B4020 from Solvay Polyolefins, Rosignano, (Italy) was used. The details of the used polymer are summarized in Table 1. The samples were produced using an OIMA-85 ECO 3080 injection molding machine c/o Interplast, Scandicci (FI), Italy. The temperature was increased progressively along the apparatus from 160 up to 200°C. Then the standard samples were performed by cutting the injected samples to get the final size of about 18×4×4 mm. Since during cutting, the sample surfaces became a little bit rough thus just to reduce experimental errors the surface of all samples were polished by using wet grinding method. The polishing was continued to achieve a surface roughness of about 10 micron. It is worth noting to avoid increasing temperature the polishing was done under cooling water system.

Table 1. Specification of used HDPE

Melting Temperature [°C]	Crystallization Temperature [°C]	Crystallinity Index	Grade
129	117	56%	Injection

2.2. Dilatometry test

Dilatometery test is the simplest way to predict dimensional stability of materials [9]. The dilatometry apparatus was Dima_85ECO3080. The machine was equipped with cooling circulation system. To find out the role of heating rate on change in length, the samples were heated from room temperature up to 70°C at different heating rates i.e. 2, 5, 10, 20, 30, 40 and 60°C/min. The change in length corresponding to each temperature was measured directly. Three samples for each material were tested. All samples were taken away after reaching to room temperature. Then SCTE and thermal strain were calculated for each heating rate by Equation (1) and (3), respectively.

2.3. Simulation

The main goal of using simulation method was to predict the sensitivity of dimensional stability of HDPE on heating rate. To do so the following objects were investigated.

- Effect of heating rate on temperature gradient.
- Effect of heating rate on strain gradients.
- Variation of displacements and thermal strains versus temperature using experimental data.

The used thermo physical properties are shown in Table 2. In the current study SCTE was taken into account as a function of 1) Temperature and 2) both temperature and hearting rate. It is worth noting that the originality of the current study is paying attention to both temperature and heating rate, simultaneously. Furthermore, dependency of SCTE on temperature gradient was neglected because of low temperature gradient.

Simulation was done using finite element method. Just for getting the most stable results the different element divisions were tried. The optimum results were obtained using the following divisions.

Length (*X* direction) = Height (*Y* direction) = 5 elements and width (*Z* direction) = 20 elements. Hence the used total elements are 500 elements. Initial and boundary conditions were applied on the HDPE model according to the push rode dilatometry. The conditions are shown in Figure 2 schematically.

Table 2. Thermo-physical properties of HDPE as a function of temperature

T [°C]	0	50	100	150
K [W/m^2 °C]	0.44	0.38	0.32	0.25
C_P [J/kg °C]	1640	2050	2860	–
E [MPa]	2500	1350	350	–
ρ [kg/m^3]	–	940–960	–	–

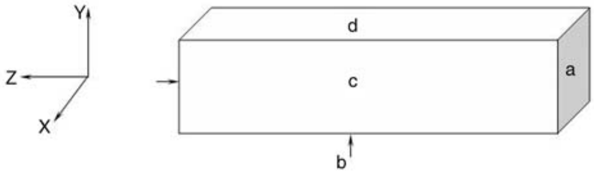

Figure 2. The applied boundary conditions on the surfaces. *a*: Constrained in all directions, *b* and *d*: constrained in *Y* direction, *c*: constrained in *X* direction

3. Results and discussions

Figure 3 illustrates variations of displacement of HDPE along *Z*-direction versus temperature. As it can be seen a raise in temperature corresponds to more displacement along *Z*-direction. The true reason of this variation can be attributed to boundary condition (applied to Figure 2) which can have an effect on chain vibration and free volume of HDPE. Displacement counters along *Z*-direction due to increasing temperature at the several heating rates are shown in Figure 4. As it shows the displacement is distributed uniformly along the specimen (Z direction) except near the surface because of constraint.

Figure 5 shows that the latent thermal strain variation as element vanishes from origin point. This behavior is expected by considering the Equations (1) and (3). Also as seen in Figure 3 and Figure 5 both displacement and ε_{th} along Z-direction raise as heating rate increase at a constant temperature.

To determine the temperature distribution within the specimen, the results of simulation of thermal analysis can be useful. The Results show that the

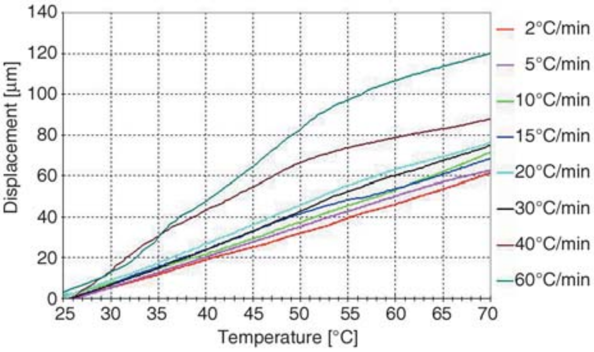

Figure 3. Experimental displacement versus temperature along *Z* direction at different heating rates

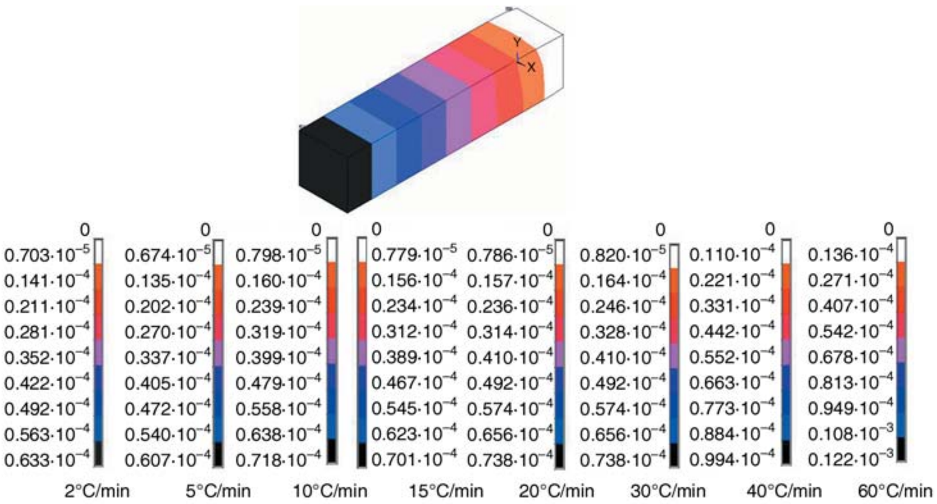

Figure 4. Displacement counters along *z*-direction due to increasing temperature at the several heating rates

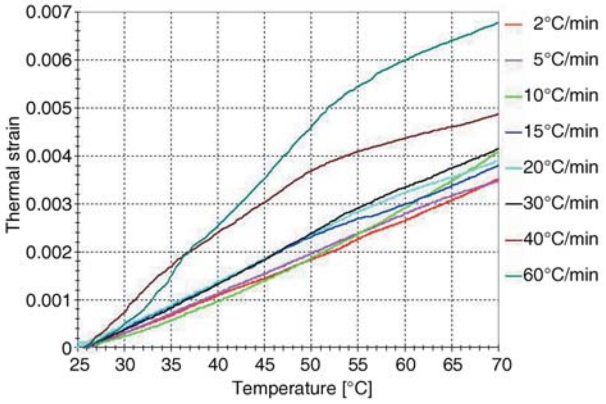

Figure 5. Experimental thermal strains versus temperature along *Z* direction at different heating rates

maximum temperature gradient occurs at the heating rate of 60°C/min and it is about 10% of final temperature approximately, since the sample size is very small. The temperature contours are shown in Figure 6. The result of numerical calculation of SCTE is shown in Figure 7. As it can be observed both thermal strain and SCTE show an increase as temperature increases. At each heating rate, two separated regions can be recognized. At the beginning of test the slope is almost linear but gradually the slope shows a nonlinearity behavior. The reason of linear behavior at the beginning of each curve can be attributed to reaching the sample temperature to the considered temperature. After passing from linear part, nonlinearity behavior of SCTE as a function of both temperature and heating rate appears. Indeed SCTE of HDPE shows a different behavior at low and high temperatures and heating rates. Looking at in more details on Figure 7 shows that there is a critical heating rate i.e. 30°C/min and

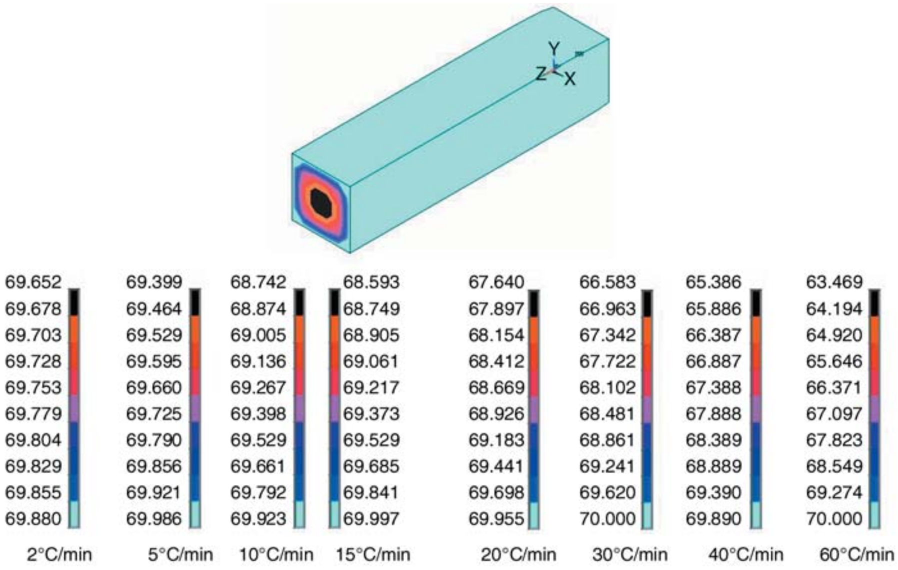

Figure 6. Temperature distribution counters of HDPE specimens at different heating rates

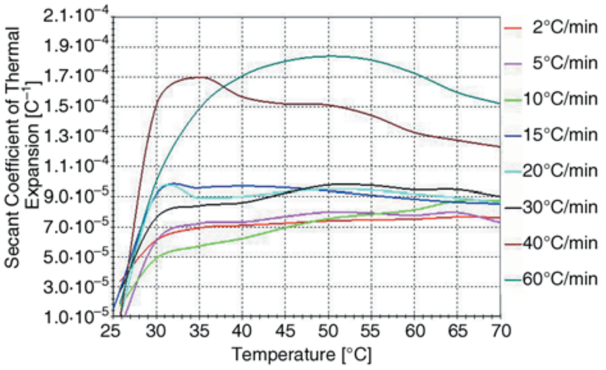

Figure 7. Experimental SCTE versus temperature along *Z* direction at different heating rates

if heating rate becomes greater than the rate SCTE will be shown a nonlinearity behavior other wise it will be changed linearity as temperature increases. The subject should be under attention is post crystallization (recrystallization) of polyethylene during reheating. This is because polyethylene is a semi crystalline polymer and its spherulite size and even its crystallinity can be affected by heating and reheating. To clarify post crystallization looking at in more details on Figure 7 can be useful. The figure shows that at low heating rates (i.e. 2, 5, 10, 20 and 30°C/min) trends of the curves are smooth unlike high heating rate (i.e. 40 and 60°C/min). In fact at high heating rate the spherulites have not enough time to rearrange unlike at low heating rate. This behavior can be a result of more recrystallisation (or post crystallization) of polymer [21–22].

Our results differ from those presented by other investigators is that we take into account the effect of both temperature and heating rate on SCTE. While previous scientists have paid attention just to temperature, the effect of heating rate on SCTE has been neglected. For example, the result of an investigation which was concentrated on SCTE of crystalline polymeric solids showed a linear relationship between SCTE and temperature [13]. The authors believe that the reason of nonlinearity can be influenced by thermal shock and distribution of strain within the HDPE specimen.

Using simulation and computation of SCTE, thermal strains at different heating rate were calculated. The results of the thermal-structural analysis are shown in Figures 8 and 9. Figures 8a and 9a show the simulation results of SCTE as a function of just temperature. Dependency of SCTE on both temper-

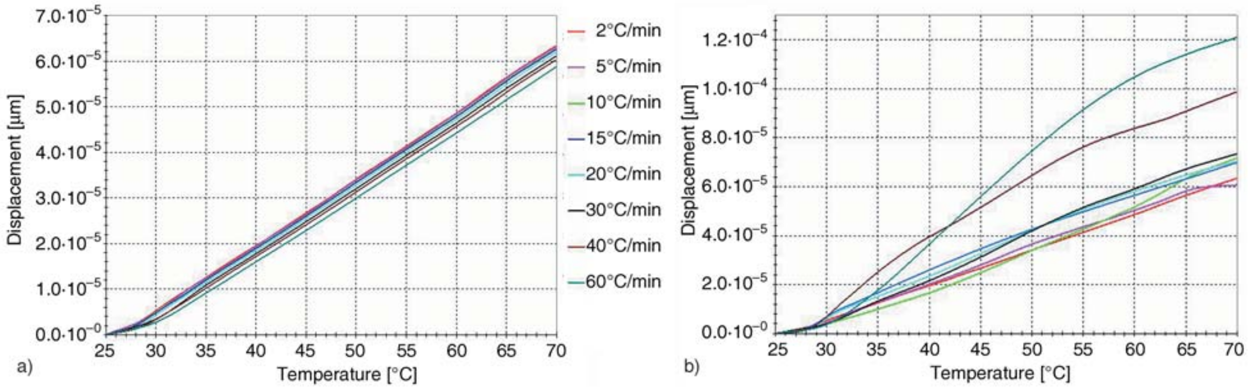

Figure 8. Simulated displacement versus temperature along *Z* direction at different heating rates. a – SCTE is as a function of temperature. b –SCTE is as a function of both temperature and heating rate

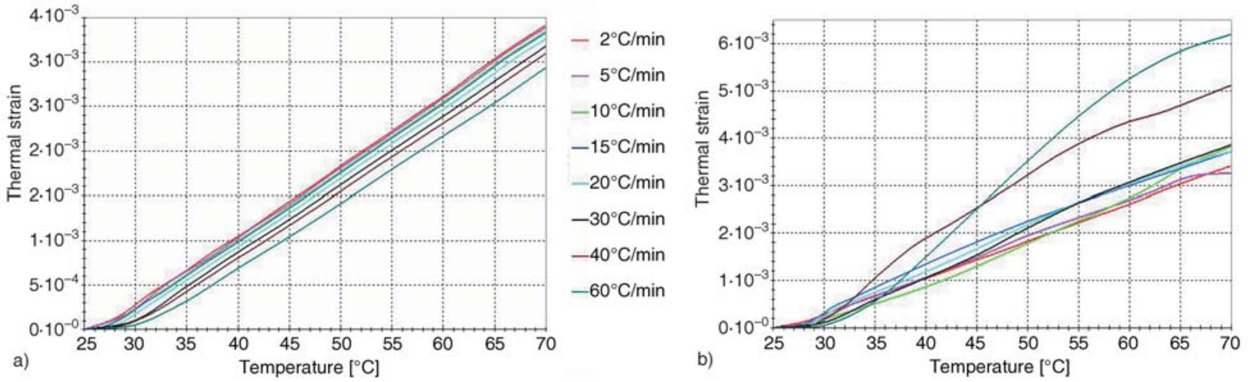

Figure 9. Simulated thermal strain versus temperature along *Z* direction at different heating rates. a – SCTE is as a function of temperature. b – SCTE is as a function of both temperature and heating rate

ature and heating rate are illustrated in Figures 8b and 9b. The simulation results show thermal strain is not in good agreement with experimental data when SCTE is just as a function of temperature while validity of simulation of thermal strain can be achieved if SCTE is as a function of both temperature and heating rate.

4. Conclusions

To investigate the sensitivity of dimensional stability of high density polyethylene on both temperature and heating rate the standard dilatometry test was done on the HDPE specimens. Secant coefficient of linear thermal expansion was computed from the test. Then by considering boundary conditions and material properties, dilatometry test has been simulated at different heating rates and the thermal strain versus temperature was calculated. The results are remarked as bellow.

- Both Thermal strain and SCTE depend on heating rate.
- There is a critical heating rate in which dependency of SCTE on both heating rate and temperature will be changed.
- The results of simulation show a good agreement with experimental data.

References

[1] Dong W. C., Kwang J. K., Byoung C. K.: Effects of silicalite-1 nanoparticles on rheological and physical properties of HDPE. Polymer, **47**, 3609–3615 (2006).

[2] Rajendra K. K.: Analysis of ductile and brittle failures from creep rupture testing of high-density polyethylene (HDPE) pipes. Polymer, **46**, 11664–11672 (2005).

[3] Walker C., Sigbritt K.: Assessment of thermal and thermo-oxidative stability of multiextruded recycled PP, HDPE and a blend thereof. Polymer Degradation and Stability, **78**, 385–391 (2002).

[4] Seong O. H., Dong W. L., Oc H. H.: Thermal degradation of crosslinked high density polyethylene. Degradation and Stability, **63**, 237–243 (1999).

[5] Bernal-Lara T. E., Liu R. Y. F., Hiltner A., Baer E.: Structure and thermal stability of polyethylene nanolayers. Polymer, **46**, 3043–3055 (2005).

[6] Ulas I.: Drawing of high density polyethylene tube Effect of different cooling conditions. Polymer Engineering and Science, **39**, 855–861 (1999).

[7] Bagdade S. D.: ASM Ready Reference: Thermal properties of metals. ASM International, Materials Park, Ohio (2002).

[8] ASTM E228-95. Standard test method for linear thermal expansion of solid materials with a vitreous silica dilatometer (1995).

[9] Zahran R. R., Shenouda S. S., El-Tawil Y. A., El-Kayar A.: Analysis of the thermal expansion behavior of oriented polyoxymethylene sheets. Polymer Engineering and Science, **36**, 1377–1386 (1996).

[10] Kardos J. L., Raisoni J., Piccarolo S., Halpin J. C.: Prediction and measurement of the thermal expansion coefficient of crystalline polymers. Society of Plastics Engineers, **19**, 1000–1009 (1979).

[11] Garai J.: Correlation between thermal expansion and heat capacity. Computer Coupling of Phase Diagrams and Thermochemistry, **30**, 354–356 (2006).

[12] El-Tonsy M. M.: Low cost technique for measuring thermal expansion of thin polymer samples. Polymer Testing, **22**, 57–62 (2003).

[13] Thomas C. H., Sue A. B. A., Paul A. K.: In situ measurement of the thermal expansion behavior of benzocyclobutene films. Journal of Polymer Science Part B: Polymer Physics, **37**, 311–321 (1999).

[14] ASTM E831-93: Standard test method for linear thermal expansion of solid materials by thermomechanical analysis (1993).

[15] ASTM D696-03: Standard test method for coefficient of linear thermal expansion of plastics between –30°C and 30°C (2003).

[16] Zakin J. L., Simha R., Hershey H. C.: Low-temperature thermal expansivities of polyethylene, polypropylene, mixtures of polyethylene and polypropylene, and polystyrene. Journal of Applied Polymer Science, **10**, 1455–1473 (1966).

[17] Brillhart M. V., Cebe P.: Thermal expansion of the crystal lattice of novel thermoplastic polyimides. Journal of Polymer Science Part B: Polymer Physics. **33**, 927–936 (1995).

[18] Jayanna H. S., Subramanyam S. V.: Thermal expansion of irradiated polyethylene from 10 to 340 K. Journal of Polymer Science Part B: Polymer Physics, **31**, 1095–1098 (1993).

[19] Pottiger M. T., Coburn J. C., Edman J. R.: The effect of orientation on thermal expansion behavior in polyimide films. Journal of Polymer Science Part B: Polymer Physics, **32**, 825–837 (1994).

[20] Broer D. J., Mol G. N.: Anisotropic thermal expansion of densely cross-linked oriented polymer networks. Polymer Engineering and Science, **31**, 625–631 (1991).

[21] Wunderlich B.: Thermal Analysis of Polymeric Materials. Springer-Verlag, Berlin (2005).

[22] Zachmann H. G.: Schmelzerscheinungen und Kristallisationserscheinungen bei makromolekularen Substanzen. 6. Ergebnisse der Rontgenkleinuntersuchungen und Weitwinkeluntersuchungen an Polyglykolterephthalat (Terylen). Makromolekulare Chemie, **52**, 23–28 (1962).

eXPRESS Polymer Letters Vol.1, No.2 (2007) 98–103
Available online at www.expresspolymlett.com
DOI: 10.3144/expresspolymlett.2007.17

Preparation of low-molecular-weight polyamide 6/ hydrotalcite intercalated nanocomposites via insitu polymerization

Z. Yan-wu[*], *J. Jun-qing*

College of Chemical Engineering, Zhengzhou University, Zhengzhou, 450000, PR China

Received 19 November 2006; accepted in revised form 17 January 2007

Abstract. Low-molecular-weight PA6 (LMW-PA6)/hydrotalcite intercalated nanocomposites were prepared via insitu polymerization in the presence of organo-hydrotalcite with alanine as an initiator at 150°C. The results indicated that alanine in the interlayer gallery of hydrotalcite doesn't change the interlayer distance of hydrotalcite, while it can initiate the polymerization of ε-caprolactam. There exsists γ crystalloid of LMW-PA6 in LMW-PA6/hydrotalcite intercalated nanocomposites. The molecular weight distribution of LMW-PA6 in the intercalated nanocomposites has two peaks and the added amounts of organo-hydrotalcite hardly influence molecular weight of LMW-PA6.

Keywords: *nanomaterials, low-molecular-weight polyamide 6, hydrotalcite, in situ polymerization, alanine*

1. Introduction

Polyamide 6 (PA6) has been widely used as engineering plastic and fibres and extensively researched since 1930s while low-molecular-weight PA6 (LMW-PA6) is seldom studied though it can be used to improve rheology behavior of coatings and processing behavior of polyamide or as modifiers of fillers in polymer composites. In the past ten years, PA6 nanocomposites were prepared by melt-compounding and in situ polymerization [1–6]. But most research on PA6 nanocomposites focused on the use of silicate clays as nanoparticles due to its commercially availability, high aspect ratio and considerable cation-exchange capacity. Silicate clays can improve the mechanical and gas barrier properties of polymer materials. Compared with silicate clays, hydrotalcite is a synthetic layered inorganic mineral composed of positively charged layers and interlayer-exchangeable anions [7, 8]. It has been widely used as catalyst, ion exchanger, absorbent, ceramic precursor, and in organic-inorganic nanocomposites [9–11].

Among numerous hydrotalcites Mg-Al hydrotalcite is an excellent inorganic flame retardant and smoke suppressant. Although many reports about the intercalation of organic anions into hydrotalcite have been published, relatively few reports have discussed the incorporation of hydrotalcite into polymers. Andrea Sorrentino incorporated Mg-Al hydrotalcite into a biodegradable poly(ε-caprolactone) by high energy ball milling [12]. Wen-Fu Lee prepared nanocomposite superabsorbents containing intercalated hydrotalcite via insitu polymerization [13]. Fabrice L studied the difference of in situ polymerization between hydrotalcite and hydrocalumite host structures [14]. However PA6 or LMW-PA6 nanocomposite containing hydrotalcite is seldom researched.

Usually PA6 is prepared by ring-opening polymerization at high temperature or anion polymerization. Though the rate of anionic polymerization is

---

[*]Corresponding author, e-mail: zhangyanwu@zzu.edu.cn

very rapid, polymerization conditions are rigorous and polymerization procedures are not easily controllable. During preparation of polyamide, other monomers are introduced into the chains of polyamide to endow them with functional properties such as biodegradability or change its crystallization structure [15–17].

Considering application of LMW-PA6, excellent rheology behavior is favored. In this paper DL-alanine was used to initiate ring-opening polymerization and copolymerization of ε-caprolactam. Therefore chain structure of LMW-PA6 was changed to improve its change rheology behavior. LMW-PA6/hydrotalcite nanocomposites were prepared via in situ polymerization in the presence of hydrotalcite at lower temperature. The effect of hydrotalcite on cystalloid of LMW-PA6, molecular weight of polymer and the structure of composites prepared was detailed studied.

2. Experimental

2.1. Materials

ε-caprolactam [$COC_5H_{10}NH$] (CP), DL-alanine [$CH_3CH(NH_2)COOH$] (BR) and Oleic acid [$C_{17}H_{33}COOH$] (AR) were purchased and used as received. N, N-dimethyl formamide (DMF) was of reagent analytical grade and distilled before used. Mg-Al hydrotalcite with high crystallinity was synthesized according to the 'Urea' method [18].

2.2. Intercalation of alanine into hydrotalcite

Because alanine anion exists only in basic solutions, ion-exchange must be carried out in a basic solution. 11.76 g DL-alanine, 20 g Mg-Al hydrotalcite and 5.28 g NaOH was put into 1000 ml de-ionized water. The solution was stirred for 5 hours at 70°C and then filtered. The solid product was washed three times with de-ionized water. At last the obtained powder was dried at 70°C in vacuum for 24 hours. The final product was called as organo-hydrotalcite.

2.3. Insitu polymerization of ε-caprolactam initiated by alanine in the presence of hydrotalcite

A 250 ml four-neck flask, equipped with a reflux condenser, a stirring rod, and a thermometer, was charged with ε-caprolactam [$COC_5H_{10}NH$] (I), alanine [$CH_3CH(NH_2)COOH$] (II), oleic acid [$C_{17}H_{33}COOH$] (III), water and organo-hydrotalcite. To avoid the thermal oxidative degradation of ε-caprolactam and alanine nitrogen purge was used during the procedure. The polymerization temperature was set at 150°C and the polymerization was terminated after 6 hours. The viscous liquid products were washed three times with hot water and dried under vacuum. Amounts of the reagents in each run were listed in Table 1.

2.4. Characterization

The structure of hydrotalcite was characterized with wide angle X-ray diffraction (WAXRD) on a Japan D/max-RB 12-kW diffractometer using CuKα as a radiation source, operated at 40 kV and 100 mA. The scanning rate and the scanning range were 6°C/min and from 2°C to 70°C respectively.

Content of intercalated analine was determined by thermogravimetric analysis (TGA) on Seiko TG/DT 6200 Thermogravimetric analyzer and with absorbance analysis on Shimadazu UV-2450 ultraviolet-visible spectrophotometer. For TGA characterization the samples dried at 100° under vacuum for 12 hours were heated under nitrogen at a heating rate of 10°C/min from 100°C to 700°C. For absorbance analysis samples was washed with deionized water for three times and filtrate was collected to analyze analine content.

Molecular weight of polymer was measured using gel permeation chromatography (GPC) method with Agilent 1100 series (Agilent Technologies). The temperature of columns was set at 50°C. Polystyrene was chosen as standard samples. Samples were dissolved in DMF at 50°C with sonication and those containing hydrotalcite were

Table 1 Amounts of the reagents in each run

Runs	ε-caprolactam (I) [g]	Alanine (II) [g]	oleic acid (III) [g]	water [ml]	organo-hydrotalcite [g]	$–NH_{2(I+II)}/–COOH_{III}$ [mol/mol]
1#	20	3.4	30.3	5	0	2.00
2#	20	3.4	30.3	5	2.7	2.14
3#	20	3.4	30.3	5	5.4	2.28
4#	20	0	30.3	5	5.4	1.92

dipped in hydrochloric acid solution for 24 hours to remove hydrotalcite before dissolved.

3. Results and discussion

3.1. WAXRD patterns of hydrotalcite and organo hydrotalcite

Higher crystallization of Mg-Al hydrotalcite is helpful to elucidate accurately the effect of hydrotalcite on the polymerization and the structure of the products. Figure 1. shows WAXRD patterns of Mg-Al hydrotalcite and organo-hydrotalcite. In WAXRD patterns of Mg-Al hydrotalcite the narrow peaks and smooth base lines show the characteristics of a highly crystalline layered structure of Mg-Al hydrotalcite. After hydrotalcite was intercalated by alanine, the typical peak (003) 2θ of hydrotalcite changes little and still lies at about 11.6°. This is different from other intercalated hydrotalcites. The typical peak (003) 2θ usually shift to smaller angles and the interlayer distance of hydrotalcite increases for other anion intercalated hydrotalcites [9]. The reason may be that molecule size of alanine isn't large enough to increase the interlayer distance. Due to higher alanine adsorption quantity of hydrotalcite determined by TGA in the following section, there should be intercalated alanine in the gallery of hydrotalcite.

3.2. Content of intercalated alanine

In addition to modifying hydrotalcite alanine can initiate the polymerization of ε-caprolactam and may become incorporated into the polymer chains as a co-monomer. So the quantity of alanine between hydrotalcite layers is important for the polymerization of ε-caprolactam and chain structure of copolymer. TGA analysis was used to determine the quantity of alanine between hydrotalcite layers. TGA curves of Mg-Al hydrotalcite and organo-hydrotalcite were shown in Figure 2 and Figure 3 respectively. Both Mg-Al hydrotalcite and organo-hydrotalcite have three weight-loss regions. The detailed data are listed in Table 2. After thermal decomposition the weight of Mg-Al hydrotalcite and organo-hydrotalcite residuals are 70.8 wt% and 55.4 wt% respectively. Because of the presence of water, decomposition products of analine ions and carbonic ions between layers of hydrotalcite released on heating, the content of intercalated alanine was calculated according to the formula

$$\frac{M_w(\text{alanine anion})}{M_w(\text{alanine anion}) - M_w(\text{carbonic anion})}\cdot(Rh - Ro) = 48.4\%)$$

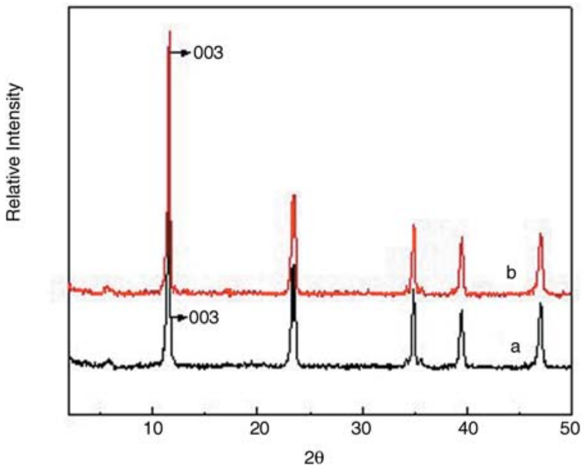

Figure 1. WAXRD patterns for a – Mg-Al hydrotalcite; b – organo-hydrotalcite

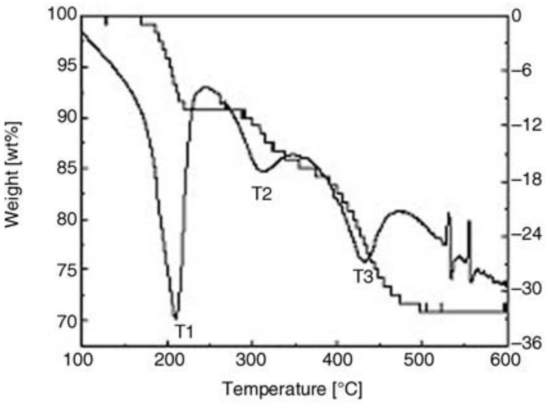

Figure 2. TGA analysis of Mg-Al hydrotalcite

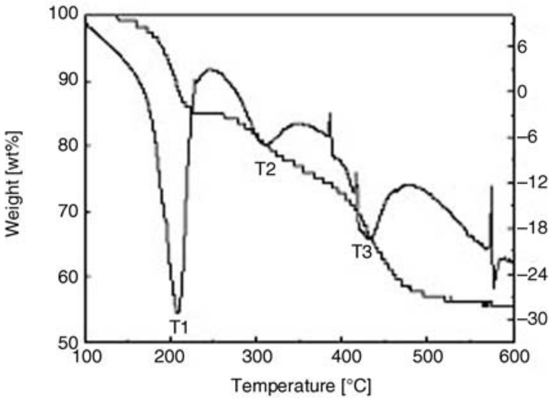

Figure 3. TGA analysis of organo-hydrotalcite

Table 2. Data of TGA analysis

Sample	T_1 [°C]~wt%	T_2 [°C]~wt%	T_3 [°C]~wt%
hydrotalcite	209.9~90.8	313.7~85	433.5~70.8
organo-hydrotalcite	208.5~85.1	310.9~76.0	431.5~55.4

Rh: residual weight [%] of hydrotalcite after thermal decomposition;
Ro: residual weight [%] of organo-hydrotalcite after thermal decomposition.

Through simple mathematical computation, molar content of alanine in each gram of organo-hydrotalcite can be calculated as 5.44 mmol/g.

To validate the result of TGA methods, absorbance analysis was used to determine the content of intercalated alanine. The result of absorbance analysis was 42% and similar to that of TGA methods. This approved that TGA method was a simple and effective method determining the content of intercalated alanine.

There exist two structures for layered minerals/ polymer nanocomposites: intercalated and exfoliated. WAXRD was used to explore the dispersion state of hydrotalcite in the products. The WAXRD patterns was shown in Figure 4. The results showed that the typical peak (003) 2θ of hydrotalcite shift from 11.6° to small angle 2.96° after in situ polymerization. If the thickness of the brucite-like layer is assumed to be 0.48 nm, the interlayer distance calculated according to Bragg formula changes from 0.28 to 2.5 nm. This showed that alanine intercalated in hydrotalcite has initiated ε-caprolactam to polymerize and produced polymer chains enlarge the distance between layers. So the products belong to intercalated nanocomposites.

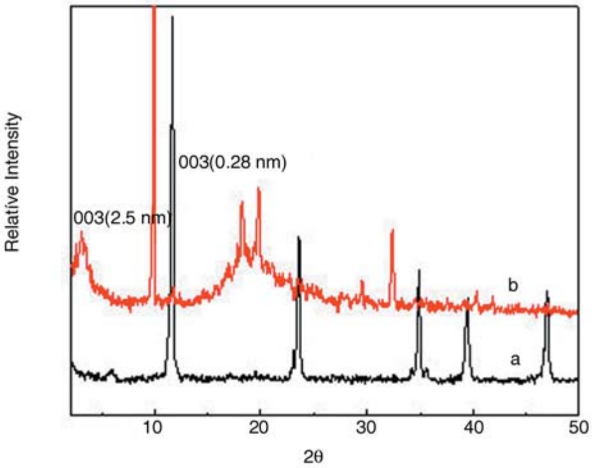

Figure 4. WAXRD patterns of the products containing 10% organo-hydrotalcite

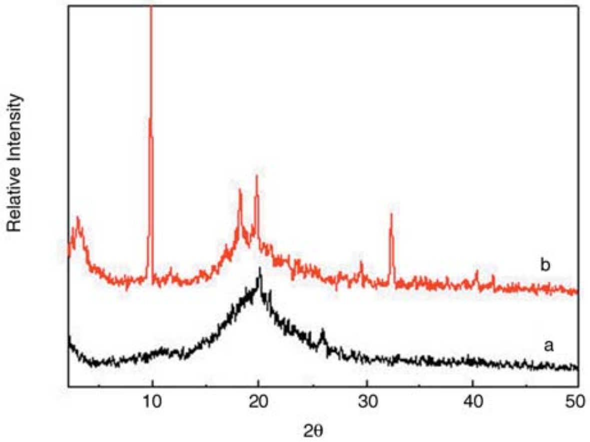

Figure 5. WAXRD patterns for a – LMW-PA6; b – LMW-PA6 containing 10% organo-hydrotalcite

3.3. Effect of hydrotalcite on the crystalloid of low-molecular-weight PA6

PA6 generally has two crystalloids including α and γ and usually exists in the α crystal form. Does hydrotalcite affect the crystal type of LMW-PA6? WAXRD patterns of LMW-PA6 and LMW-PA6/hydrotalcite intercalated nanocomposites were compared (Figure 5.).

The result showed that LMW-PA6 prepared has two typical diffraction peaks of α crystalloid while LMW-PA6/hydrotalcite intercalated nanocomposites has a very obvious diffraction peak of the ? crystalloid (2θ = 19.7°). We thought that limited space between layers of hydrotalcite hindered crystallization of LMW-PA6.

3.4. Effect of hydrotalcite on the molecular weight of LMW-PA6

Molecular weight and its distribution are important factors on property and processing of polymer. Hydrotalcite may affect molecular weight and its distribution of the products. GPC curves and the number average molecular weight (Mn) of the products are shown in Figure 6. and Figure 7. respectively. Molecular weight distribution of the in situ polymerization products in the presence of organo-hydrotalcite has double peaks while that in the absence of organo-hydrotalcite has only one peak. At the same time, Mn of the products of in situ polymerization in the presence of organo-hydrotalcite is higher than that in the absence of organo-hydrotalcite. When organo-hydrotalcite is present, ε-caprolactam can polymerize by itself or may diffuse into interlayer gallery of hydrotalcite and polymerize there. Due to difference of end-cappings oleic acid reaction rate with $-NH_2$ at the end of polymer chains, there existed two molecular-weight polymers. Furthermore, the amount of organo-hydrotalcite didn't influence molecular

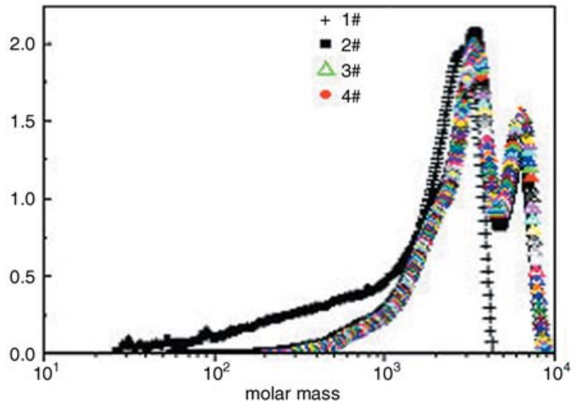

Figure 6. GPC curves of the products 1# – hydrotalcite content 0%; 2# – organo-hydrotalcite content 5%; 3# – organo-hydrotalcite content 10%; 4# –organo-hydrotalcite content 10% without additional alanine

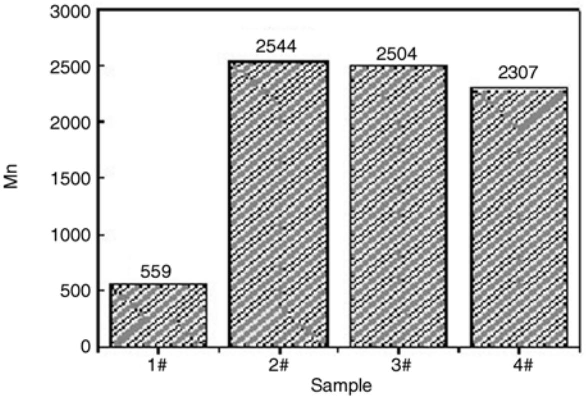

Figure 7. Number average molecular weight (Mn) of the products 1# – hydrotalcite content 0%; 2# – organo-hydrotalcite content 5%; 3# – organo-hydrotalcite content 10%; 4# – organo-hydrotalcite content 10% without additional alanine

weight of the products. If additional alanine was not introduced, Mn of the products decreased slightly. As we know, the ratio between amount of $-NH_2$ in monomer ε-caprolactam and alanine and amount of –COOH in end-cappings oleic acid affected molecular weight of the polymers. This was because the ratio between monomer and end-cappings changes from 2.14 to 1.92.

4. Conclusions

LMW-PA6/hydrotalcite intercalated nanocomposites were prepared via in situ polymerization in the presence of organo-hydrotalcite with alanine as an initiator at 150°C. Though intercalated alanine doesn't change the interlayer distance of hydrotalcite, alanine in the interlayer gallery of hydrotalcite can initiate ε-caprolactam to polymerize and therefore LMW-PA6/hydrotalcite intercalated nanocomposites were prepared. There exsist γ crystalloids of LMW-PA6 in LMW-PA6/hydrotalcite intercalated nanocomposites. The molecular weight distribution of LMW-PA6 in the intercalated nanocomposites has two peaks and added amounts of organo-hydrotalcite hardly influence molecular weight of LMW-PA6. Without additional alanine ε-caprolactam can polymerize in the present of hydrotalcite and Mn of the products decreases slightly.

References

[1] Wu T-M., Liao C-S.: Polymorphism in nylon6/clay nanocomposites. Macromolecular Chemistry and Physics, **201**, 2820–2825 (2000).

[2] Ranade A., D' Souza N. A., Gnade B., Dharia A.: Nylon-6 and montmorillonite-layered nanocomposites. Journal of Plastic Film and Sheeting, **19**, 271–285 (2003).

[3] Rusu G., Rusu E.: Nylon6/SiO_2 nanocomposites synthesized by in situ anionic polymerization. High Performance Polymers, **18**, 355–375 (2006).

[4] Chavarria F., Paul D. R.: Comparison of nanocomposites based on nylon 6 and nylon 66. Polymer, **45**, 8501–8515 (2004).

[5] Rhutesh K., Shah P. K., Paul D. R.: Nylon 6 nanocomposites prepared by a melt mixing masterbatch. Polymer, **45**, 2991–3000 (2004).

[6] Hasegawa N., Okamoto H., Kato M., Usuki A., Sato N.: Nylon 6/Na-montmorilllonite nanocomposites prepared by compounding nylon 6 with Na-montmorillonite slurry. Polymer, **44**, 2933–2937 (2003).

[7] Miyata S.: Synthesis of hydrotalcite-like compounds and their structures and physico-chemical properties the systems $MgAlNO_3$, MgAlCl, $MgAlClO_4$, NiAlCl, ZnAlCl. Clays and Clay Minerals, **23**, 369–372 (1975).

[8] Ulibarri M. A., Pavlovic I., Barriga C., Hermosín M. C., Cornejo J.: Adsorption of anion species on hydrotalcite-like compounds: effect of interlayer anion and crystallinity. Applied Clay Science, **18**, 17–27 (2001).

[9] Li F., Duan X.: Applications of Layered Double Hydroxides. Springer, Berlin (2006).

[10] Vaccari A. Yamaoka T.: Preparation and catalytic properties of cationic and anionic clays. Catalysis Today, **41**, 53–71 (1998).

[11] Coudray B. M., Lakshmi K. M., Kavita B., Venkat R. C., Koteswara R. K., Figueras F.: Aldol condensations catalysed by novel Mg-Al-O-t-Bu hydrotalcite. Tetrahedron Letters, **39**, 3555–3558 (1998).

[12] Sorrentino A., Gorrasi G., Tortora M., Vittoria V., Constantino U., Marmottini F., Padella F.: Incorporation of Mg-Al hydrotalcite into a biodegrad-

able Poly(ε-caprolactone) by high energy ball milling. Polymer, **46**, 1601–1608 (2005).

[13] Lee W. F., Chen Y. C.: Superabsorbent Polymeric Materials. XIV. Preparation and water absorbency of nanocomposite superabsorbents containing intercalated hydrotalcite. Journal of Applied Polymer Science, **94**, 2417–2424 (2004).

[14] Vieille L., Moujahid E., Taviot-Gueho G., Cellier J., Besse J. P., Leroux F.: In situ polymerization of interleaved monomers: a comparative study between hydrotalcite and hydrocalumite host structures. Journal of Physics and Chemistry of Solids, **65**, 385–393 (2004).

[15] Okamura A., Hirai T., Tanihara M.: Synthesis and properties of novel biodegradable polyamides containing α-amino acids. Polymer, **43**, 3549–3554 (2002).

[16] Marek M. J., Stehlícek J., Doskocilová D.: Synthesis and properties of copolymers consisting of aramide and poly(6-hexanelactam) blocks. European Polymer Journal, **31**, 363–368 (1995).

[17] Franco L., Navarro E., Subirana J. A., Puiggali J.: Incorporation of glycine residues in even-even nylons disrupts their characteristic all-trans conformation. Polymer, **39**, 5553–5560 (1998).

[18] Yang P. P., Su M. P., Yang X. W., Liu G. Z., Yu J. F., Wu T. H., Cho D. H., Chang T. S., Lee D. K.: Synthesis of high crystallinity hydrotalcite-like compounds with urea method. Chinese Journal of Inorganic Chemistry, **19**, 485–490 (2003).

eXPRESS Polymer Letters Vol.1, No.2 (2007) 104–108
Available online at www.expresspolymlett.com
DOI: 10.3144/expresspolymlett.2007.18

Water absorption of epoxy/glass fiber/organo-montmorillonite nanocomposites

W. S. Chow[*]

School of Materials and Mineral Resources Engineering, Engineering Campus, Universiti Sains Malaysia, Nibong Tebal
14300 Pulau Pinang, Malaysia

Received 28 November 2006; accepted in revised form 2 January 2007

Abstract. The epoxy/glass fiber/organo-montmorillonite (OMMT) nanocomposites were prepared by hand lay up method. In the previous work, the flexural and morphological properties of the epoxy/glass fiber/OMMT were studied. In this work, the epoxy nanocomposites were characterized by X-ray diffraction (XRD), differential scanning calorimetry (DSC) and water absorption tests. The exfoliation of OMMT in epoxy/glass fiber nanocomposites was detected by XRD. DSC results showed that the glass transition temperature (T_g) of epoxy was increased slightly in the presence of OMMT. Water uptake of epoxy was reduced by the addition of glass fiber and OMMT. The decrease of water absorption in epoxy is attributed to the increasing of tortuosity path for water penetration in the epoxy composites by the hybrid of glass fiber and OMMT.

Keywords: *polymer composites, epoxy, glass fiber, organo-montmorillonite, water absorption*

1. Introduction

Epoxy resin represents some of the highest performance resin due to the mechanical properties and resistance to environmental degradation, which leads to their almost exclusive use in aircraft components. Epoxies are defined as cross-linked polymers in which the cross-linking is derived from reactions of the epoxy group. Epoxy resin usually used in coating industry as surface coating materials which combine toughness, flexibility, adhesion and chemical resistance. In addition, epoxy resin can also be used in both laminating and molding techniques to make fiber reinforcement with better mechanical strength, chemical resistance and electrical insulating properties [1]. Epoxy resin also used with reinforcing fibers for advanced composites application. This is due to the capability of epoxy resin that showed good adhesion to the embedded fiber [2].

Clays have received much attention as reinforcing materials for polymers because of their potentially high aspect ratio and unique intercalation/exfoliation characteristics. Montmorillonite (MMT) frequently exhibit unexpected properties including reducing gas permeability, improved solvent resistance, and superior mechanical and enhance flame-retardant properties [2]. Typically, clay minerals have a layered silicate structure about 1 nm in thickness and a high aspect ratio ranging from 100 to 1500 [3]. Naturally occurring montmorillonite is incompatible with most polymers because of its hydrophilic nature. Ion exchange is widely practiced to modify the montmorillonite's surface to increase its compatibility with mostly hydrophobic polymers. Introduction of organic ions may decrease the Van der Waals interactions between the silicate layers and hence increase the interlamellar spacing [4].

Glass fiber is a part of reinforcing materials for reinforced plastics based on single filaments of

---

[*] Corresponding author, e-mail: shyang@eng.usm.my

glass ranging in diameter from 3 to 19 micrometers. Glass fibers show good performance and play a main function in playground equipment, recreational items, piping for corrosive chemicals, and many other common applications. The cost of the glass fiber is considerably lower than the cost of carbon-based fibers [5]. Fiber reinforced composites can be explained as the strength of fibers in fibrous composites exceeds considerably the strength of the matrix. Fibers such as short aramid (AF), glass (GF) or carbon (CF) fibers are used in order to increase the creep resistance and the compressive strength of the polymer matrix system used [6]. The addition of fibers is to ensure the strength of the material while the matrix helps to keep the shape of the composite.

Thermoset layered silicate nanocomposite may synthesize as intercalated/exfoliated structure. It is depending on stacked layer structure of the clay is maintained after processing with the polymer matrix. Although thermoset nanocomposite often prepared by swelling organically modified clay with a monomer precursor, it may be advantageous if intercalation and/or exfoliation can be achieved by combining suitable functionalized monomer/pre-polymers with a native layered silicate such as sodium montmorillonite [7]. The ideal case in order to maximize the stiffness and thermal properties of the epoxy-clay nanocomposite is through full exfoliation and well dispersed of clay platelets in the composites [8].

The preparation method used for mixing the epoxy resin with clay is in situ intercalative polymerization method. In this method, the layered silicate is swollen within the monomer solution so the polymer formation can occur between the intercalated sheets. Polymerization can be initiated either by heat or by diffusion of a suitable initiator or by an organic initiator or catalyst fixed through cation exchange the interlayer before the swelling start to occur [9]. The most important manufacturing process of composites applied to aerospace industry is the hand lay-up of prepregs and autoclave cure. The hand lay-up still persists as the method in use for more than half of all advanced aerospace composites structures attributed to the flexibility of this technique which allows the manufacturing of varieties shapes. Additionally hand lay-up does not require large capital investment [10].

Epoxy resins are very attractive due to high strength and stiffness, high temperature resistance, low shrinkage, low volatility and etc. However, the epoxy resin absorbs high degree of moisture which in turn degrades the functional, structural and mechanical properties of the composites [11]. In our previous studies, it was found that the optimum loading of OMMT in epoxy/glass fiber nanocomposites is attained at 3 wt% [12]. The combination of glass fiber and organo-montmorillonite could give a synergistic effect on the improvement of mechanical properties for epoxy through hand-lay up technique. Consequently, the objective of this continuous research work is to enhance the water resistance of epoxy by the combination of glass fiber and organo-montmorillonite.

2. Experimental

2.1. Materials

Epoxy resin used in this study was diglycidyl ether bisphenol A [(DGEBA) DER 331] provided by Dow Chemical. It was used in combination with cycloaliphatic amine hardener (HY 2964) supplied by Ciba Geigy. The glass fiber used was in the form of chopped strand mat (CSM). The organo-montmorillonite (OMMT) used in this study was commercially available modified montmorillonite layered silicate (Nanomer I.30E) from Nanocor, USA.

2.2. Sample preparation

2.2.1. Epoxy/OMMT mixture preparation

The ratio between epoxy and hardener was 10:6 wt/wt. Then, 3 wt% of OMMT was added to the DGEBA resin. The mixture was then stirred using a mechanical stirrer at 100 rpm. The stirring process was continued until all the OMMT powder was well dispersed in the epoxy resin system in about 10 minutes. Next, hardener was added into the mixture and the stirring process continued for about 5 min.

2.2.2. Hand lay-up method

Four plies (17×17 cm^2) of CSM were cut. The first ply of CSM was placed on an aluminium plate which had been covered with a polypropylene (PP) film. Next, epoxy resin was applied on the glass fiber mat. It is important to ensure that the resin wets the entire surface of glass fiber. Then, additional resin was applied and the second ply was laminated until complete wetting. This procedure was repeated until all the plies were superimposed, and a PP film was applied on top of the laminate glass fiber. Then, the sample was pressed with a metal roller from one side to the other. The purpose of pressing is to attain the desired thicknesses of approximately 3.2 mm. Then, an aluminium plate was placed on the top of the sample. The laminated samples were placed in an oven for complete curing process at 100°C for 60 min.

2.3. Sample characterization

X-ray Diffraction (XRD) was performed with a Diffraktometer D5000 Siemens (Kristaloflex) Model. The X-ray beam was equipped with a CuKα ($\lambda = 0.1504$ nm) radiation operated at 40 kV and 30 mA. The scanning speed and step size were 1°/min and 0.02°, respectively. The diffraction patterns were collected between 1° and 10°. The interlayer spacing of the OMMT was derived from the peak position (d_{001}-reflection) in the XRD diffractograms according to the Bragg equation ($\lambda = 2d\sin\theta$).

The glass transition temperature (T_g) of epoxy/glass fiber/OMMT nanocomposites was determined by a Perkin Elmer (DSC 6). The test was performed at a heating and cooling rate of 10°C/min in nitrogen (N_2) atmosphere. The samples were heated from 30–160°C, and held at 160°C for 1 min. Then, the samples were cooled from 160–30°C.

Water absorption of epoxy composites was performed according to ASTM D570. Specimens were dried at 80°C in a vacuum oven until a constant weight was attained. Then, they were immersed in water in a thermostated stainless steel water bath at 30°C. Weight gains were recorded by periodic removal of the specimens from the water bath and weighing on a balance with a precision of 1 mg. The percentage gain at any time t (M_t) as a result of moisture absorption was determined by Equation (1):

$$M_t = \frac{W_w - W_d}{W_d} \cdot 100 \quad [\%] \qquad (1)$$

where W_d and W_w denote the weight of dry material (the initial weight of materials prior to exposure to the water absorption) and weight of materials after exposure to water absorption, respectively.

3. Results and discussion

Figure 1 shows the X-ray diffractogram of OMMT powder and epoxy/glass fiber/OMMT nanocomposites. The corresponding pattern of the epoxy nanocomposites is in the range of the diffraction angle $2\theta = 1$–$10°$. The basal spacing for OMMT powder is 2.03 nm. An almost complete disappearance of the characterization peak of OMMT in epoxy/glass fiber/OMMT was detected. This indicates that the silicate platelets in the epoxy matrix were exfoliated. The absence of basal reflection in nanocomposites indicates good exfoliation of silicate platelets in epoxy matrix. The formation of exfoliation or intercalation of silicate platelets is due to the reaction of OMMT with amine hardener [13]. Ratna *et al.* [14] also reported that the absence of d_{100} peak in the X-ray spectrum of all binary and ternary epoxy/layered silicate systems indicates exfoliation of clay.

Figure 2 shows the DSC thermograms of epoxy/glass fiber and epoxy/glass fiber/OMMT nanocomposites. The glass transition temperature (T_g) value

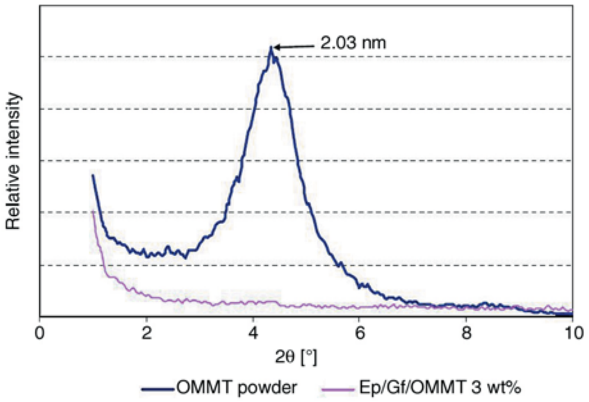

Figure 1. X-ray diffractograms patterns of the OMMT and epoxy/glass fiber/OMMT nanocomposites

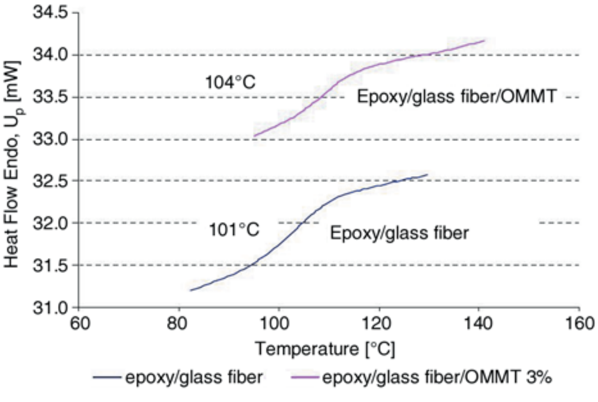

Figure 2. DSC thermograms of epoxy/glass fiber composites and epoxy/glass fiber/OMMT nanocomposites

of epoxy/glass fiber and epoxy/glass fiber/OMMT is 101°C and 104°C, respectively. Epoxy/glass fiber/OMMT nanocomposite recorded slightly higher T_g value than that of epoxy/glass fiber composite. The presence of the alkyl ammonium ions in OMMT might catalyzes the polymerization within the clay galleries, which could further promote the inter-gallery polymerization. This could leads to a better OMMT dispersion and exfoliation. The slightly higher T_g value maybe correlate to the exfoliation of OMMT in the epoxy/glass fiber composites. The slightly increment of T_g value of epoxy/glass fiber/OMMT nanocomposites also maybe due to the interaction of OMMT and glass fiber in the epoxy network which could restrict the chain mobility. This can be attributed to confinement of polymer chain as a result of intercalation into the interlayer gallery of the clay [14].

Figure 3 shows water uptake of epoxy, epoxy/glass fiber composites and epoxy/glass fiber/OMMT nanocomposites. The water absorption of all epoxy samples was reached saturation after 35 days. This indicates that the absorption reaches quasi-equilibrium condition. The water absorption will recommence after quasi-equilibrium [15]. However, water molecules can only stay in micro-voids and form clusters. The water cluster might be bound due to the large form of cluster. Only external water molecules of clusters may interact with the polymer. The water molecules might be free molecules which have diffused initially during immersion. Water absorption will reach a real equilibrium when all micro-voids are filled.

It can be seen that the water absorption of epoxy is relatively higher compared to epoxy/glass fiber composites and epoxy/glass fiber/OMMT nanocomposites. The water uptake of epoxy is approximately 2.3% upon subjected to water absorption test for 40 days. The water sorption behavior is considered to depend on free volume properties, type and concentration of polar groups in the epoxy system [16]. According to Becker *et al.* [16], the equilibrium water uptake of the epoxy/layered silicate nanocomposites was reduced compared to the neat epoxy system. Water uptake may be due to the capability of the water molecules to penetrate through the epoxy network. The diffusion of water occurs in epoxy resin is attributed to the nature of the polymer which shows strong interaction with water. In epoxy matrices, water molecules couple strongly with hydrophilic functional groups such as hydroxyl or amine in epoxy resin. The water molecules might interact with epoxy molecules by forming hydrogen bonding with hydrophilic groups [17]. The absorption of water can be attributed to the affinity of the functional groups of the epoxies which having high polarity towards water molecules [18]. Water can be existence in two forms (i) free water which will fill the micro-cavities of the network structure in the composites, and (ii) strong interactions occur within the water molecules and polar group of epoxy resin [19].

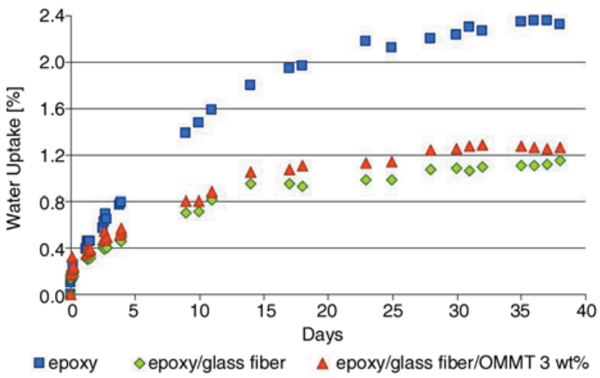

Figure 3. Water uptake on epoxy, epoxy/glass fiber composites, and epoxy/glass fiber/OMMT nanocomposites

From Figure 3, it can be seen that the water uptake of epoxy/glass fiber composites is about 1.1% after subjected to water absorption for 40 days. Fiber reinforcement in epoxy matrix could reduce the penetration of water in composites. However, the incorporation of OMMT in the epoxy/glass fiber composite slightly increases the water uptake. The epoxy/glass fiber/OMMT nanocomposites specimens recorded water absorption value at 1.25% upon 40 days. This might be due to the octadecyl onium ion on OMMT surface which could react with water. The N–H$^+$ groups of alkylammonium ions are hydrogen-bonded to water molecules by donating protons to the water-oxygen atoms. The ammonium group may form up to three hydrogen bonds with water molecules. Induction of ammonium group may increase the acid strength of the hydrating water molecules and latter may donate protons to additional water molecules [20].

4. Conclusions

Epoxy/glass fiber/OMMT hybrid nanocomposites prepared by hand-lay up technique showed exfoliation characteristics and slightly enhancement in glass transition temperature. The water resistance properties of epoxy were improved by the addition of both glass fiber and OMMT, which is maybe attributed to the increasing of the tortuosity path for water penetration.

References

[1] Wilkinson S. B., White J. R.: Thermosetting short fibre reinforced composites. in 'Short fibre-polymer composites' (eds.: De S. K. and White J. R.), Woodhead Publishing Limited, Cambridge, 54–81 (1996).

[2] Zhou Y., Pervin F., Biswas M. A., Rangari V. K., Jeelani S.: Fabrication and characterization of montmorillonite clay-filled SC-15 epoxy. Materials Letters, **60**, 869–873 (2006).

[3] Guo B., Jia D., Cai C.: Effects of organo-montmorillonite dispersion on thermal stability of epoxy resin nanocomposites. European Polymer Journal, **40**, 1743–1748 (2004).

[4] Kornmann X., Rees M., Thomann Y., Necola A., Barbezat M., Thomann R.: Epoxy-layered silicate nanocomposites as matrix in glass fiber-reinforced composites. Composites Science and Technology, **65**, 2259–2268 (2005).

[5] Hyer M. W.: Stress analysis of fiber-reinforced composite materials. McGraw-Hill, USA, 578–699 (1998).

[6] Friedrich K., Zhang Z., Schlarb A. K.: Effects of various fillers on the sliding wear of polymer composites. Composites Science and Technology, **65**, 2329–2343 (2005).

[7] Rodlert M., Plummer C. J. G., Garamszegi L., Leterrier Y., Grünbauer H. J. M., Manson J.-A. E.: Hyperbranched polymer/montmorillonite clay nanocomposites. Polymer, **45**, 949–960 (2004).

[8] Jordan J., Jacob K. I., Tannenbaum R., Sharaf M. A., Jasiuk I.: Experimental trends in polymer nanocomposites – a review. Materials Science and Engineering, A **393**, 1–11 (2005).

[9] Ray S. S., Okamoto M.: Polymer/layered silicate nanocomposites: a review from preparation to processing. Progress in Polymer Science, **28**, 1539–1641 (2003).

[10] Jones F. R.: Matrices: Epoxy resins. in 'Handbook of polymer-fibre composites' (eds.: Jones F. R.) Polymer Science & Technology Series, Longman Scientific & Technical, England, 69–129 (1994).

[11] Kim J-K., Hu C., Woo R. S. C., Sham M-L.: Moisture barrier characteristics of organoclay-epoxy nanocomposites. Composites Science and Technology, **65**, 805–813 (2005).

[12] Mazlan N., Abu Bakar A., Chow W. S.: Effects of organo-montmorillonite on the mechanical and morphological properties of epoxy/glass fiber composites. Polymer International, DOI: 10.1002/PI.2146, article in press (2007).

[13] Siddiqui N. A., Woo R. S. C., Kim J-K., Leung C. C. K., Munir A.: Mode I interlaminar fracture behaviour and mechanical properties of CFRPs with nanoclay-filled epoxy matrix. Composites: Part A, **38**, 449–460 (2007).

[14] Ratna D., Becker O., Krishnamurthy R., Simon G. P., Varley R. J.: Nanocomposites based on a combination of epoxy resin, hyperbranched epoxy and a layered silicate. Polymer, **44**, 7449–7457 (2003).

[15] Popineau S., Rondeau-Mouro C., Sulpice-Gaillet C., Shanahan M. E. R.: Free/bound water absorption in an epoxy adhesive. Polymer, **46**, 10733–10740 (2005).

[16] Becker O., Varley R. J., Simon G. P.: Thermal stability and water uptake of high performance epoxy layered silicate nanocomposites. European Polymer Journal, **40**, 187–195 (2004).

[17] Zhou J., Lucas J. P.: Hygrothermal effects of epoxy resin. Part 1: The nature of water in epoxy. Polymer, **40**, 5505–5512 (1999).

[18] Karad S. K., Attwood D., Jones F. R.: Moisture absorption by cyanate ester modified epoxy resin matrices, Part V: Effect of resin structure. Composites: Part A, **36**, 764–771 (2005).

[19] Han S. O., Dzarl L. T.: Water absorption effects in hydrophilic polymer matrix of carboxyl functionalized glucose resin and epoxy resin. European Polymer Journal, **39**, 1791–1799 (2003).

[20] Yariv S.: Introduction to organo-clay complexes and interactions. in 'Organo-clay complexes and interactions' (eds.: Yariv S. and Cross H.) Marcel Dekker, New York, 40–112 (2002).

eXPRESS Polymer Letters Vol.1, No.2 (2007) 109–121
Available online at www.expresspolymlett.com
DOI: 10.3144/expresspolymlett.2007.19

Theoretical and experimental study of the effect of fiber heads on the mechanical properties of non-continuous basalt fiber reinforced composites

L. M. Vas[1], *K. Pölöskei*[1], *D. Felhős*[2], *T. Deák*[1], *T. Czigány*[1,3*]

[1]Department of Polymer Engineering, Faculty of Mechanical Engineering, Budapest University of Technology and Economics, H-1111 Budapest, Műegyetem rkp. 3., Hungary
[2]Institute of Machine Design, Faculty of Mechanical Engineering, Budapest University of Technology and Economics, H-1111 Budapest, Műegyetem rkp. 3., Hungary
[3]Research Group for Metals Technology, Hungarian Academy of Sciences, H-1111 Budapest, Goldmann tér 3., Hungary

Received 27 November 2006; accepted in revised form 26 January 2007

Abstract. The effect of basalt fibers, produced by the Junkers technology and used as reinforcement in polymer composites, was modeled on the properties of composites, adapting the statistical fiber mat model of Poisson type. The random distribution was approximated by so-called effective spheres that act as defect sites in composites, reducing their strength. The role of fiber heads in strength reduction and the corresponding failure modes were analyzed theoretically using a model and by experiments performed on specimens containing a single fiber head located at different distances from the crack initiation. The applicability of the model was proven both experimentally and by finite element analysis. Based on all these investigations, the effective cross section reduction, and hence the strength reduction (predicted by the model) caused by the presence of fiber heads was proven.

Keywords: *polymer composites, basalt fiber, modeling and simulation, fiber head, finite element model*

1. Introduction

Nowadays the most popular reinforcement in polymer composites is glass fiber, which combines high strength and relatively good interfacial adhesion to the polymer matrix with a low price. Recently increasing attention has been paid to fibers of natural origin, among them to basalt fibers [1, 2], produced from volcanic basalt rock by melting. Due to its excellent reinforcing properties – both alone and in combination with other reinforcements – it spread rapidly, together with other natural fibers [3, 4]. Cheap, non-continuous basalt fibers produced by the Junkers technology are brittle, which has to be considered when producing composites form them. Simple adaptation of processes used for thermoplastic or thermosetting matrix composites may result in a significant decrease of the average fiber length and in the deterioration of mechanical properties [5–7]. The essence of the Junkers technology is that the basalt melt flows from the gas fired tank furnace into a fiber-forming device with horizontal axis, consisting of an accelerator cylinder and two fiber-forming cylinders. The fibers formed by centrifugal force are blown away by high pressure air. This way of fiber spinning is especially productive and cheap, but its disadvantage is that smaller or larger ‘heads’ remain at the end of the fibers.

The aim of this publication is to analyze the influence of these fiber heads formed on basalt fibers produced by the Junkers technology, gaining popu-

---

*Corresponding author, e-mail: czigany@eik.bme.hu larity as a reinforcement in polymer composites, on the mechanical properties of composites [8, 9].

2. Materials used

For the experimental tests basalt fibers produced by the TOPLAN Ltd. (Hungary) were used. The matrix material used for polymer/basalt fiber composites (with or without fiber heads), was H 384 F polypropylene produced by TVK Co. (Hungary), while for the single fiber head composites R 359 PP grade was used. The former composite samples were produced by melt mixing and hot pressing at 200°C, while the latter ones by extrusion at 205°C mold temperature followed by cold pressing.

3. Finite element and analytical modeling, measurement methods

The presence of fiber heads may affect the mechanical properties of composites in various ways. On the one hand they may improve toughness by anchoring the fiber, and on the other hand they serve as defect sites and reduce the strength properties. Based on our experience, the latter aspect seems to be dominant. First finite element modeling was used to determine the characteristics of the stress zones around the fiber head, and then the consequences of this phenomenon on the strength properties of composites were described by an analytical model. DEN-T specimens manufactured from PP and single fiber head PP sheets were used to determine the model parameters, while the real strength reduction caused by the fiber heads was determined by tensile tests on conventional dumbbell shape specimens. Afterwards the results calculated by the model were compared to the measured ones.

3.1. Basic experiments needed for the analytical model

Tensile specimens were manufactured from the pressed composite sheets according to standard ISO 527-1:1993 (E), and tensile strength was calculated from the test carried out on these pieces with a universal tensile tester of Zwick Z020 type, at a tensile rate of $v = 2$ mm/min, as suggested by the standard.

The tensile tests of single fiber head composites were carried out on 20×50 mm size DEN-T specimens widely used for measuring EWF (essential work of fracture), machined from 1 mm thick sheets, and a 1-mm wide and 7 mm deep notch was prepared on these specimens, later sharpened by a blade. Tensile tests were carried out on a universal tensile tester of Zwick Z005 type at a tensile rate of $v = 0.5$ mm/min. The schematic sketch of the specimens can be seen in Figure 1.

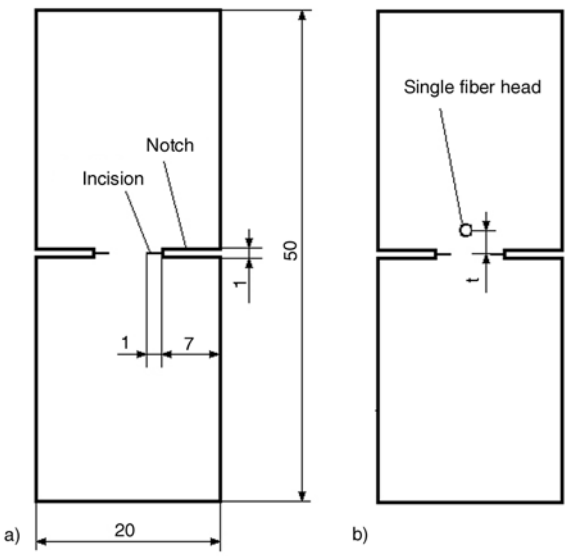

Figure 1. DEN-T specimens notched and cut on both sides, made of unmodified PP (a) and single fiber head PP (b)

3.2. Finite element modeling

Finite element program Cosmos/M was used in our work. An axisymmetric finite element grid made up of Plane2D elements was prepared. The material characteristics were considered constant as a function of temperature. The boundary condition assumed during the analysis was that the bottom plate of the model was fixed in direction Y, and the upper plate was loaded with an evenly distributed force. A boundary layer was applied between the fiber heads and the matrix. The material properties of the thin boundary layer between the matrix and the fibre-head were calculated as the averages of the corresponding material properties of the fibre and the matrix material. This thin layer constitutes a transition zone between the rigid fibres and the soft matrix. The nodes of the finite element mesh at the border of the different materials are common, so the properties of these different materials are matched with each other. The model was cooled down from 160°C to 25°C in one step. Force con-

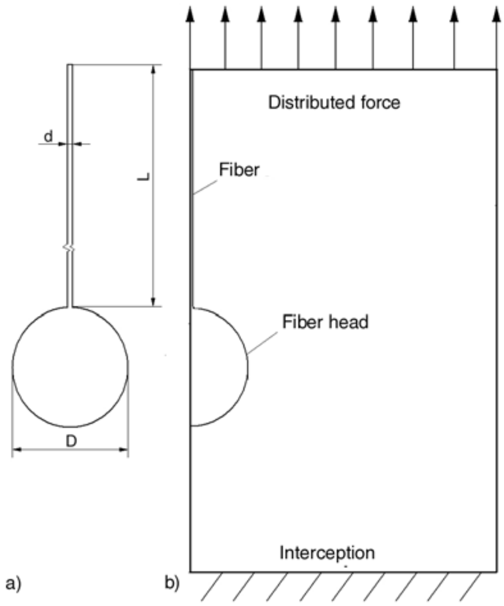

Figure 2. Approximation of the applied fiber head with a sphere (a), and the schematic sketch of the axisymmetrical finite element model (b)

trol and Newton-Raphson method were used in the simulation of the tensile process.

The characteristic size of fiber heads is in the order of tens to hundreds of µm, their shape is ellipsoidal or sometimes conical, but they can be well approximated by an equivalent sphere. Figure 2a shows the model of a spherical fiber head, while Figure 2b includes the schematic sketch of the axisymmetric finite element model.

Table 1. The values of the geometrical parameters of fiber heads

Fiber head shape	d [µm]	D [µm]	L [mm]
Sphere	10	100	1
Half sphere + truncated cone	10	100	1

Table 2. The mechanical properties of materials used in the finite element model

	PP	Interface	Basalt fiber
Tensile strength [MPa]	30	315	600
Yield strength [MPa]	22	311	–
Tensile mod. of elast [GPa]	1	40.5	80

Table 3. The thermal properties of materials used in the finite element model

	PP	Interface	Basalt fiber
Coefficient of thermal conductivity [W/(mK)]	0.22	0.51	0.8
Specific heat [kJ/(kgK)]	1.7	1.27	0.84
Density [kg/m³]	910	1705	2500
Linear coefficient of thermal expansion [1/K]	$1.8\cdot10^{-5}$	$1.25\cdot10^{-5}$	$7\cdot10^{-6}$

Table 1 includes the values of the geometrical parameters shown in Figure 2.

The strength data of the fiber and the matrix based on the literature are shown in Table 2 [4, 10].

The values used in the modeling of thermal effects are listed in Table 3 [11].

3.3. Analytical model

Our aim was to model the random distribution of fiber heads and the random fiber head sizes, as well as their stress concentration zones. The fiber heads are approximated by equivalent spheres having the same volume as those of the fiber heads. The so-called 'effect zones' – drawn around the equivalent spheres –, are considered as 100% defect sites. The effect zones include the fiber head, the weak adhesion sites between the fiber head and the matrix, as well as the stress concentration zone around the fiber head (Figure 3.). The volume ratio between the fiber heads and the other parts of the composite (containing no such kind of defect site) is assumed to determine the decrease in strength.

In order to handle this problem, a statistical fiber mat model of Poisson type [12, 13] used also for describing the so called fiber flows [12–16] was adapted by substituting the fibers by spheres where a sphere $G(r,P)$ (1) was defined as a spherical volume around point P with r radius in the three dimensional real space (R^3):

$$G(r,P) = \{Q \in R^3 : d(P,Q) \le r\} \qquad (1)$$

where $d(P,Q)$ is the Euclidean distance of $P(x_P, y_P, z_P)$ and $Q(x_Q, y_Q, z_Q)$ (2):

$$d(P,Q) = \sqrt{(x_Q - x_P)^2 + (y_Q - y_P)^2 + (z_Q - z_P)^2} \qquad (2)$$

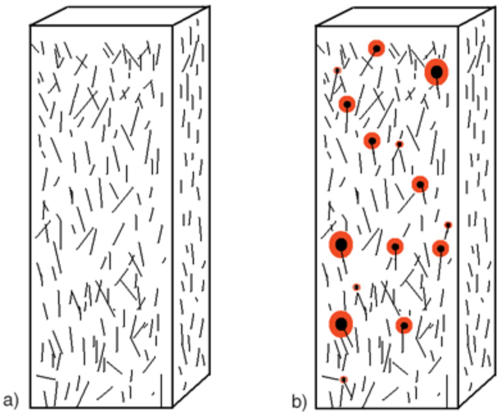

Figure 3. Short fiber reinforced composite body without fiber heads (a) and with fiber heads (b)

Accordingly, the fiber heads of different shapes and V_0 volume can be substituted by equivalent spheres of identical volume. The radius of this sphere, ρ_0 (3) is the following:

$$\rho_0 = \sqrt[3]{\frac{3V_0}{4\pi}} \tag{3}$$

ρ_0 is a stochastic variable, the distribution function of which is $Q_{\rho_0}(r)$, with finite expected value and standard deviation ($E\rho_0 = \bar{\rho}_0$, $D\rho_0 = \sigma_{\rho_0}$). The centre of the equivalent sphere is point C, it can be described by $G_0 = G(\rho_0,C)$.

The so called 'effect zone' around the equivalent sphere can be described by $G(\rho,C)$ (4) (radius: $\rho>\rho_0$), and is defined as a volume, wherein the stress is significantly larger than in the other parts of the composite. This spherical shell of thickness r_e around the equivalent sphere can be expressed by a sphere of radius ρ (Figure 4).

$$G(\rho,C) = G(r_e,G_0) = G(r_e,G(\rho_0,C)) = \bigcup_{P\in G_0} G(r_e,P) \tag{4}$$

In general the radius of the effect zone around the effective sphere depends on the radius of the equivalent sphere (5):

$$\rho = \rho_0 + r_e(\rho_0) \tag{5}$$

If simple special cases are considered, r_e may be constant and independent of ρ_0 or may be proportional to it. In the latter case their ratio can be characterized by a constant (α_e) (6):

$$r_e = \alpha_e\rho_0 \tag{6}$$

the resultant radius (7):

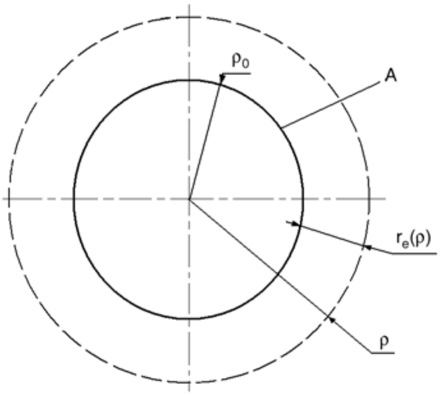

Figure 4. Effective sphere equivalent with a fiber head

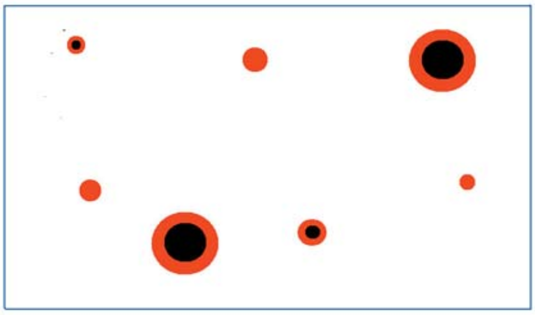

Figure 5. Spheres equivalent with fiber heads and their surrounding effective spheres in the cross section of the composite

$$\rho = (1 + \alpha_e)\rho_0 = a_e\rho_0 \tag{7}$$

where a_e (8) is a constant and based on Equation (7):

$$a_e = 1 + \alpha_e \tag{8}$$

The distribution of these effect zones (and that of the equivalent speheres) in a composite is random (Figure 5). Consequently, the distribution of the effective spheres can be described by a random sphere set (a set of defect sites or heterogeneities), in which the center point of the sphere is an element of a random point set (named point process in the theory of stochastic processes [13]) and its radius is a random variable.

It has been proven by several experiments that the distribution of different flaws in various materials can be described by the Poisson distribution [13, 17]. Based on this fact – assuming that the spatial distribution of spheres is homogeneous – the centers of these spheres can be characterized by a Poisson point process (X^*) [12, 13] in the three dimensional real space. If $B\subset R^3$ is a closed convex set, and the number of sphere center points that fall into B is $\chi_B = \#(B\cap X^*)$, then the probability that χ_B is exactly $k = 1, 2, \ldots, \infty$ can be given by a Poisson distribution according to (9).

$$P(\chi_B = k) = \frac{(KV_B)^k}{k!}\mathrm{e}^{-KV_B} \tag{9}$$

where K is the density of center points and $V_B = V(B)$ is the volume of B. Consequently, the expected value and square deviation of χ_B in this case can be obtained according to (10):

$$E\chi_B = KV_B = D^2\chi_B \tag{10}$$

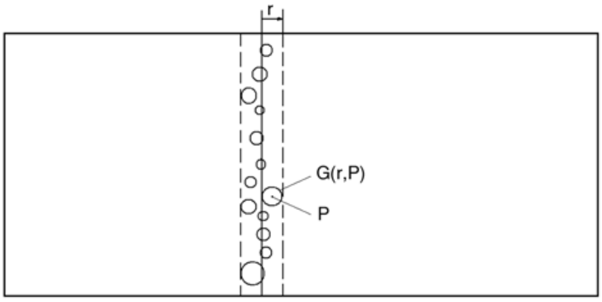

Figure 6. Effect zone of cross section B and the effective spheres within

Since the size of the fiber heads is independent of their position, (o is a variable independent from X^* and consequently from χ_B.

The fiber heads serve as defect sites in the composite, hence the effective cross section decreases, and the risk of failure increases. Let $B \subset R^3$ be a cross section of the composite body. In this case B is a two dimensional rectangle. The intersection of the effective spheres with this cross section can be seen in Figure 6.

If the properties of the number of intersections (ξ_B) of the spheres and B are analyzed, the distribution of ξ_B can be determined. Obviously, the spherical vicinity of point C of radius r intersects B if C falls within the r radius $G(r,B)$ spherical vicinity of B [12, 13]. This event of intersection can be characterized by relation (11):

$$\{B \cap G(r,C) \neq \emptyset\} = \{C \in G(r,B)\} \tag{11}$$

where the vicinity of B within the specimen (the intersection of the r radius vicinity of B and the specimen) is a prism of base A and width of $2r$.

It can be proven that ξ_B is of Poisson distribution with the parameters expressed by (12):

$$N_B = E(\xi_B) = E[KV(G(\rho,B))] = KE[2A\rho] = 2KAE(\rho) \tag{12}$$

since the volume of the vicinity of B in the specimen is $2A\rho$. This way the expected effective volume can be given by the expected value of the effective volume of B according to (13).

$$V_{BE} = E[V(G(\rho,B))] = 2AE(\rho) \tag{13}$$

The total volume of spheres intersecting B is given by (14):

$$\Phi_{Be} = \sum_{i=1}^{\xi_B} V(G(\rho_i,C_i)) = \frac{4}{3}\pi\sum_{i=1}^{\xi_B}\rho_i^3 \tag{14}$$

Equation (14) is a sum containing a random number of terms where ξ_B and ρ are not independent of each other since the vicinity of B – once ξ_B is known – depends on ρ (15).

$$E(\Phi_{Be}) = E[E(\Phi_{Be}|\rho)] = \frac{4}{3}\pi E\left[E\left(\sum_{i=1}^{\xi_B}\rho_i^3\middle|\rho\right)\right] \tag{15}$$

The conditional expected value [13] in (15) is valid for a fixed ρ if $\rho_i = \rho$ and ξ_B is the number of intersections of similar spheres with B. When calculating this conditional expected value, Eqution (16) is obtained:

$$E\left(\sum_{i=1}^{\xi_B}\rho_i^3\middle|\rho\right) = E(\xi_B|\rho)\rho^3 = KA2\rho\cdot\rho^3 = 2KA\rho^4 \tag{16}$$

wherein Equation (13) was also used. With the help of relation (16), the expected value can be calculated based on (15), according to (17):

$$V_{Be} = E(\Phi_{Be}) = \frac{8}{3}\pi KAE(\rho^4) \tag{17}$$

Knowing V_{Be}, the volume ratio that compares the volume outside the effective sphere to the total inspected volume (18) can be determined:

$$0 < \Phi_B = \frac{V_{BE} - V_{Be}}{V_{BE}} = 1 - \frac{8\pi KAE(\rho^4)}{3\cdot 2AE(\rho)} =$$
$$1 - \frac{4\pi K}{3}\frac{E(\rho^4)}{E(\rho)} < 1 \tag{18}$$

Based on the results, the fraction of the residual intact area of B can be determined, and this way the extent of strength reduction can be estimated.

Another possibility to characterize the effect of fiber heads is to determine the volume sum of all the effective spheres in the effect zone of cross section B, the radius of which is $\bar{\rho} = E(\rho)$. The number of these spheres can be estimated by (19) from the average number of the center points that fall into the effect zone of B:

$$N_{BV} = E\left(\chi_{G(\bar{\rho},B)}\right) = KE(2A\bar{\rho}) = 2KAE(\rho) \tag{19}$$

From Equations (12) and (19) it is visible that $N_{BV} = N_B$, that is the number of spheres intersecting B (type IS) is equal to that of spheres the center point of which falls into the effect zone of B (type CF). Let the set of sphere center points of those spheres, which do not intersect B be NIS and the set

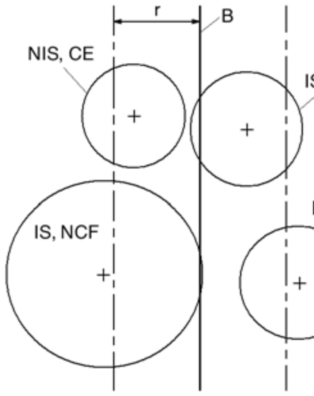

Figure 7. Relative position of center point *C* of effective spheres relative to the r radius vicinity of cross section *B*

of center points that do not fall into the effect zone *B* be NCF (Figure 7).

Let V_{BV} be the expected value of the volume sum in question that can be calculated by the following sum with a constant number of terms (20):

$$V_{BV} = E\left[\sum_{i=1}^{N_{BV}} \frac{4\pi\rho^3}{3}\right] = \sum_{i=1}^{N_{BV}} \frac{4\pi\rho_i^3}{3} = N_B \frac{4\pi}{3} E(\rho^3) = \frac{8}{3}\pi KAE(\rho)E(\rho^3) \tag{20}$$

A ratio (21) – similar to (18) – can also be determined using Equation (17):

$$\Phi_{BV} = \frac{V_{BE} - V_{BV}}{V_{BE}} = 1 - \frac{8\pi KAE(\rho)E(\rho^3)}{3{\cdot}2AE(\rho)} = 1 - \frac{4\pi K}{3}E(\rho^3) \tag{21}$$

N_B contains effective spheres of type (IS, CF) as well as spheres of (IS, NCF) type, while N_{BV} contains (IS, CF) and (NIS, CF) types, considering an average radius vicinity of *B*. Consequently, the expected values of the numbers of types (IS, NCF) and (NIS, CF) are the same.

The ratio between the volume of spheres that intersect *B* (V_{Be}) and the volume of those that fall into the effect zone of *B* (V_{BV}) can be determined based on (22):

$$\frac{V_{Be}}{V_{BV}} = \frac{E(\rho^4)}{E(\rho)E(\rho^3)} \tag{22}$$

Hence, in case of $\rho > 0$, the ratio becomes larger than 1 according to Equation (22). The reason for this is that the IS type spheres that are not of type CF (IS, NCF) are larger than those of CF type but do not belong to type IS (NIS, CF). Consequently, V_{Be} gives a better base to model the effect of fiber heads on the composite behavior.

Knowing the values of V_{Be} the effective cross section area (A_{eff}) can be estimated (23) supposing that the thickness of the effect zone remains $2E(\rho)$:

$$A_{eff} = \frac{V_{BE} - V_{Be}}{2E(\rho)} = \frac{2AE(\rho) - \frac{8}{3}\pi KAE(\rho^4)}{2E(\rho)} = A\Phi_B \tag{23}$$

This equation remains valid if ρ is substituted by ρ_0.

The main dimensions of the geometrical shapes of the fiber heads found in the basalt fiber set produced under ‘normal’ operation conditions were determined, and this way their volume could be calculated, and this distribution is shown in Figure 8.

It can be seen that frequency decreases steeply as the volume increases; this behavior can be approximated by an exponential curve that can be described by the general formula of Equation (24):

$$y = \frac{1}{\lambda} e^{-\frac{V_0}{\lambda}} \tag{24}$$

where V_0 is the fiber head volume and $\lambda = 17.94{\cdot}10^{-3}$ mm³.

Since the distribution function of the volume of fiber heads – consequently the volume of the equivalent spheres – is of exponential characteristic [13, 17], its parameter, λ is the reciprocal of the average

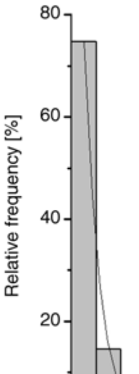

Figure 8. Characteristic fiber head volume distribution of basalt fibers (based on 226 samples)

volume of the fiber heads. Accordingly, using Equations (3), (12) and (17) the volume of equivalent spheres can be calculated easily. With the help of Equation (3), the equivalent radius (ρ_0) (25) can be calculated using the fiber head distribution found to be exponential:

$$E(\rho_0^n)=\int_0^\infty r^n \mathrm{d}Q_{\rho_0}(r)=\int_0^\infty\left(\frac{3x}{4\pi}\right)^{\frac{n}{3}}\mathrm{d}Q_{V_0}(x)=$$

$$\int_0^\infty\left(\frac{3x}{4\pi}\right)^{\frac{n}{3}}\lambda\,\mathrm{e}^{-\lambda x}\,\mathrm{d}x=\left(\frac{3}{4\pi\lambda}\right)^{\frac{n}{3}}\int_0^\infty z^{\frac{n}{3}}\,\mathrm{e}^{-z}\,\mathrm{d}z=$$

$$\left(\frac{3}{4\pi\lambda}\right)^{\frac{n}{3}}\Gamma\left(\frac{n}{3}+1\right) \tag{25}$$

where $\Gamma(p)$ is the gamma function [13, 17] ($p > 0$ real value), the values of which in case $n = 1$, 3 and 4 are $\Gamma(4/3) = 0.89298$, $\Gamma(2) = 1$ and $\Gamma(7/3) = 1.19069$, respectively. On the basis of these results, the quantities according to Equations (17) and (21) can be rewritten in the following way ((26), (27) and (28)):

$$\frac{V_{Be_0}}{V_{BS_0}}=\frac{E(\rho_0^4)}{E(\rho_0)E(\rho_0^3)}=\frac{\Gamma(7/3)}{\Gamma(4/3)}=1.3333=\frac{4}{3} \tag{26}$$

$$\Phi_{B_0}=1-\frac{4\pi K}{3}\frac{E(\rho_0^4)}{E(\rho_0)}=1-\frac{K}{\lambda}\frac{\Gamma(7/3)}{\Gamma(4/3)}=1-\frac{4}{3}\frac{\mathrm{K}}{\lambda} \tag{27}$$

$$\Phi_{B_0}=1-\frac{4\pi K}{3}E(\rho_0^3)=1-\frac{K}{\lambda} \tag{28}$$

Consequently, the volume of spheres intersecting B is 1.33 times larger than that of spheres with centers falling within the effect zone of B. The former method was used in our calculations. Since $\Phi_{B_0} < 1$, the relation is valid if $K < 3\lambda/4$. This way the fourth moment of the radius (ρ) of the effective spheres (29) corresponding to (25) can be calculated by Equation (5) or (7). Using Equation (5) leads to a complicated expression:

$$E(\rho^n)=\int_0^\infty r^n \mathrm{d}Q_\rho(r)=\int_0^\infty r^n \mathrm{d}Q_{\rho_0}(r-r_e)=$$

$$\int_0^\infty (r_0+r_e)^n \mathrm{d}Q_{\rho_0}(r_0) \tag{29}$$

In case of Equation (7) the result differs from Equation (25) only in a constant factor according to (30):

$$E(\rho^n)=\int_0^\infty r^n \mathrm{d}Q_\rho(r)=\int_0^\infty r^n \mathrm{d}Q_{\rho_0}\left(\frac{r}{a_e}\right)=$$

$$a_e^n\int_0^\infty r_0^n \mathrm{d}Q_{\rho_0}(r_0)=a_e^n\int_0^\infty\left(\frac{3x}{4\pi}\right)^{\frac{n}{3}}\mathrm{d}Q_{V_0}(x)=$$

$$a_e^n\int_0^\infty\left(\frac{3x}{4\pi}\right)^{\frac{n}{3}}\lambda\,\mathrm{e}^{-\lambda x}\,\mathrm{d}x=a_e^n\left(\frac{3}{4\pi\lambda}\right)^{\frac{n}{3}}\int_0^\infty z^{\frac{n}{3}}\mathrm{e}^{-z}\mathrm{d}z=$$

$$a_e^n\left(\frac{3}{4\pi\lambda}\right)^{\frac{n}{3}}\Gamma\left(\frac{n}{3}+1\right) \tag{30}$$

Using these formulae, the volume ratios according to (18), (21) and (22) as well as the effective cross section (23) can be calculated.

4. Results and discussion

4.1. Finite element results

The tensile test of basalt fibers with fiber heads embedded into PP matrix was modeled in the finite element simulations. Simple tensile tests were carried out on the model, and calculations were completed in order to determine the thermal stresses that arise when the unloaded model is cooled down from 160°C to 25°C, and finally the tensile test of the model loaded with thermal stresses was simulated. Figure 9 shows the results of the finite element simulation of the simple tensile test, including the von Mises type equivalent stress and equivalent strain that arise if an interface is applied in the vicinity of the fiber head.

Figure 9a reveals that the stress zones are elongated in the direction of loading (Y) and have a shape of a deformed ellipse. The stress zone below the fiber head is more significant than the one above it. Based on all these it can be stated that the separation of the fiber head/matrix is likely, hence the additional stresses in the direction of loading are significant, and have to be taken into consideration during strength dimensioning. The equivalent strain introduced in Figure 9b reaches the peak value at the border of the fiber head.

Figure 10a shows the calculated results of the finite element simulation of cooling down from 160°C to 25°C. The detailed part reveals that additional stress arises evenly around the fiber head. This stress is large close to the surface of the fiber head but decreases quickly if the distance increases. The

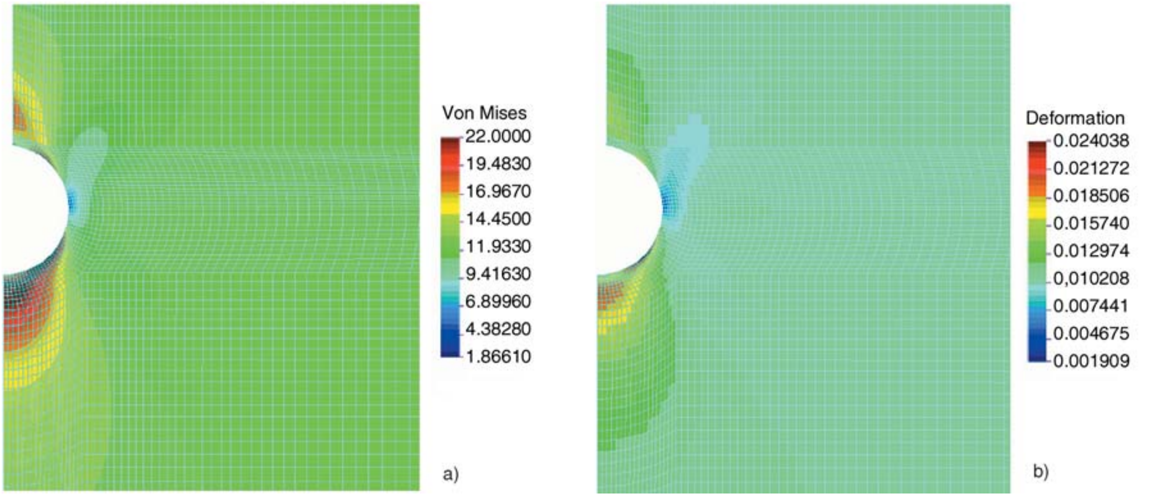

Figure 9. In case of spherical fiber head evolving von Mises stress (a) and equivalent strain (b) in the vicinity of the fiber head when interface owing to tensile loading (F_e = 11.6 N) is applied

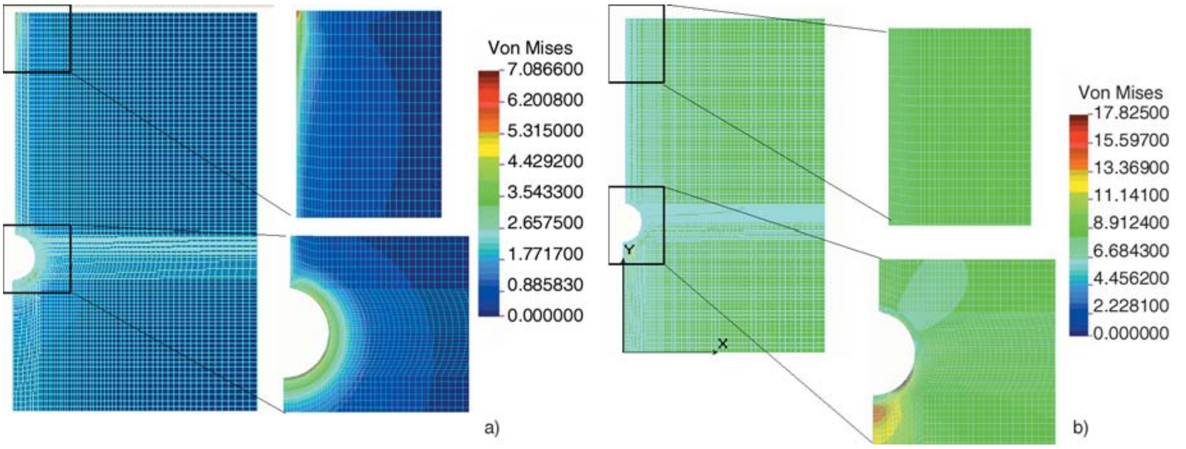

Figure 10. The effect of shrinkage stress (a), and the simultaneous effect of tensile loading (F_e = 11.6 N) and shrinkage stress during cooling down from 160°C to 25°C (b) in case of spherical fiber heads

effect zone is much smaller than that experienced in case of tensile strength. Accordingly, it is expected to be of greater importance in case of interfacial layer separation and the yielding of the matrix material around the fiber head.

Figure 10b illustrates the calculated finite element results of the combined stress of cooling down from 160°C to 25°C and the simple loading. These values differ from the stress distribution that forms on samples exposed to tensile tests without cooling. The stresses around the fiber head embedded in PP that arise due to the increased tensile loading can be found in Figure 11. The tensile strength is increased to a three times higher value in order to be able to study the yielding phenomenon of the matrix material around the fiber head. The yielding zones can be observed well at this level of loading. Based on Figure 11 it can be stated that the stress map obtained agrees well with the data found in the

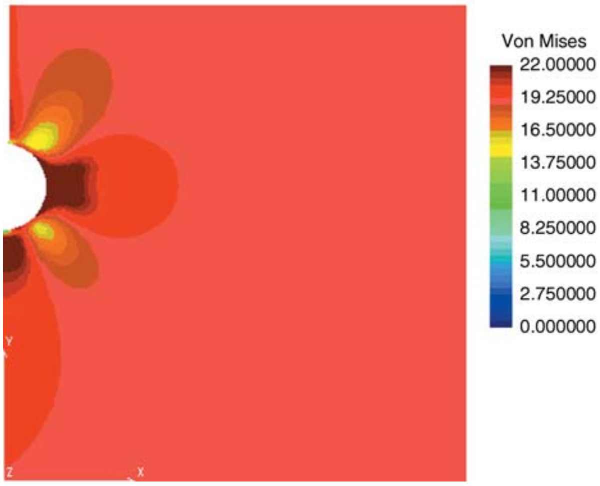

Figure 11. The simultaneous effect of tensile loading (F_e = 34.8 N) and shrinkage stress during cooling down from 160°C to 25°C in the non-linear loading stage in case of spherical fiber heads

literature [18]. Since the yield point of the matrix is 22 MPa, the von Mises stress does not exceed this value if loading is increased. However, the size of yielded areas increases if loading is increased. This larger area characterizes the yielding zones. The largest yielding occurred at the meridian of the fiber head due to the changed interfacial relations, and this differs from that Figure 9 shows. The size of the stress concentration zone, oriented in the direction of the fiber, decreased significantly.

4.2. Experimental determination of the parameters of the analytical model

The verification of the processes and their parameters is essential before the described theoretical model can be applied. Hence specimens containing PP matrix, single fibers and single fiber heads were manufactured, i.e. pressed from an extruded melt. Single fiber and single fiber head composite tensile tests were carried out on these specimens.

In case of the pressed samples it has been found that the results for single fiber head differed from the PP type R359 in the shape of the tensile curve and in the failure mode as a function of the t fiber head distance defined in Figure 1b. If t was small enough (ca. < 0.5 mm), the line of the crack diverged from the straight line that connects the two notches, and went through the fiber head (Figures 12a and b). If the distance was somewhat larger, the line of the crack did not go through the fiber head, and the cracks, initiated around the fiber head, slightly changed the crack path (Figures 12c and d). Finally, if the fiber head was far enough from the tensile cross section, additional stresses were formed but had no influence on the crack propagation (Figures 12e and f).

A strong inter-relation was found between the fiber head-matrix interaction and the state of stress during the tensile tests, and the tensile curve was divided into the following stages accordingly:

I. The fiber and the matrix are deformed simultaneously
II. Yielding around the fiber head
III. Propagation of cracks initiating from the fiber head

Furthermore, zones *a* and *b* were also defined that include the events separating the various stages:

a. Complete separation of the interface between the fiber head and the matrix, ceasing of adhesion
b. Crack formation perpendicular to the direction of loading on the meridian of fiber heads.

These stages can be evaluated since the size of fiber heads, as well as the adhesion between the fiber heads and the matrix correspond to the real values. This way calculations modeling the role of fiber heads played in the strength reduction could be made relatively simply. Firstly pure PP was examined, and its tensile strength was compared to the result of PP containing fiber heads as well. If the

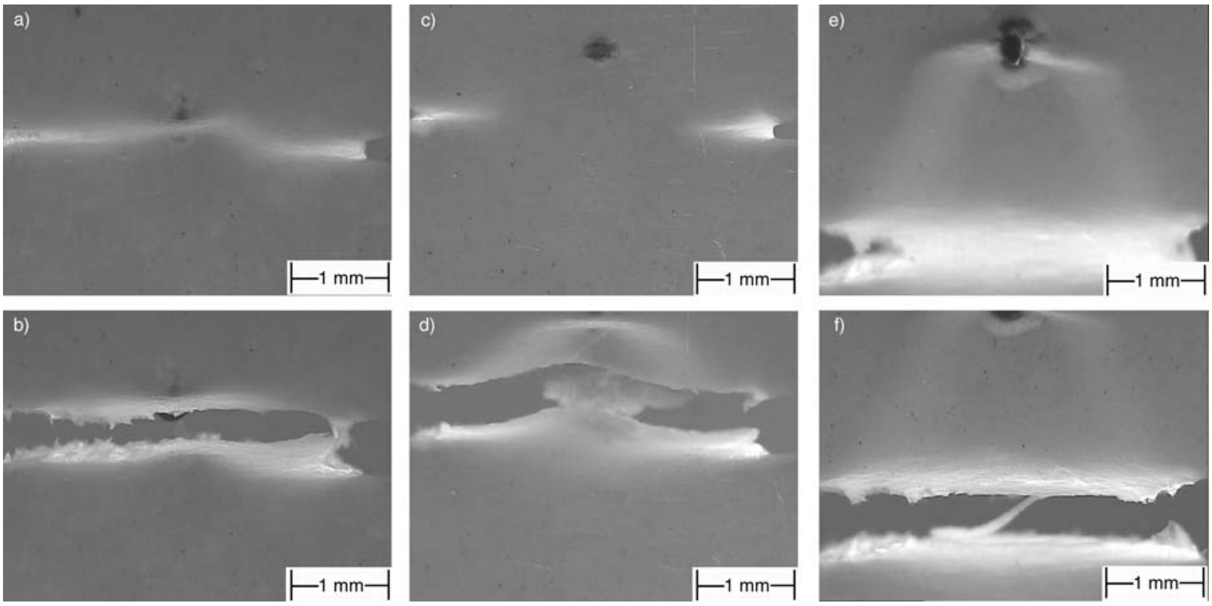

Figure 12. The effect of the distance of fiber heads from the theoretical failure cross section: the fiber head falls into the failure cross section (a) (b), the line of crack propagation inclines in the direction of the fiber head (c) (d), the fiber head has no significant influence on crack propagation (e) (f)

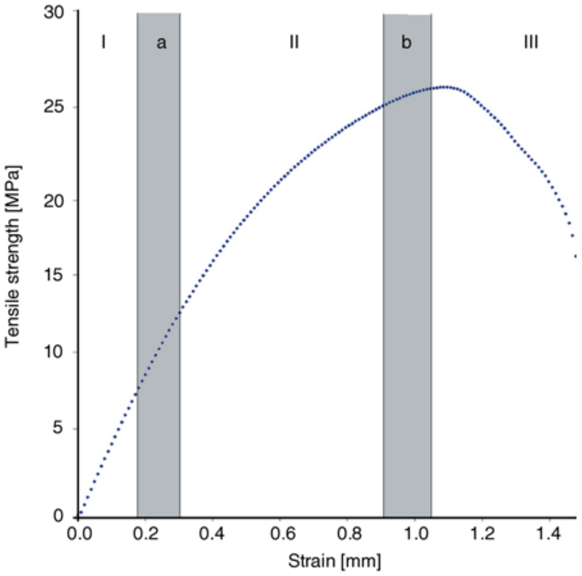

Figure 13. Characteristic single fiber head PP tensile curve: I the fiber and the matrix are deformed simultaneously, II yielding around the fiber head, III propagation of cracks initiating from the fiber head, a complete separation of the interface between the fiber head and the matrix, ceasing of adhesion, b crack formation perpendicular to the direction of loading on the meridian of fiber heads

latter value is divided by the former one, an effective flaw area (assumed to be circular), i.e. a decrease in the cross section, was calculated. Based on the ratio of this circle and the radius of the fiber head, an effective sphere radius could be calculated. A characteristic tensile curve and its stages are illustrated in Figure 13.

Based on the aforementioned facts the process of the tensile test was as follows. In stage *I* no change occurred in the structure of the sample, the deformation was totally reversible. In zone a the interfacial separation of the fiber head and the matrix occurred, and in stage *II* it was surrounded by an increasing yield vicinity (characteristically spherical) (Figure 12e). In zone b cracks formed on the meridian of the fiber head – depending on the distance from the theoretical tensile cross section – and at the same time the cracks initiated from the notches, and finally total failure occurred (Figures 12a and b). If the propagation direction of cracks initiating from around the fiber head differed from those starting from the notches, then their size was limited by the failure of the cross section (i.e. when loading stopped).

The influence of the distance of the fiber heads from the theoretical failure cross section on the tensile strength was analyzed during the above mentioned investigations (Figure 14).

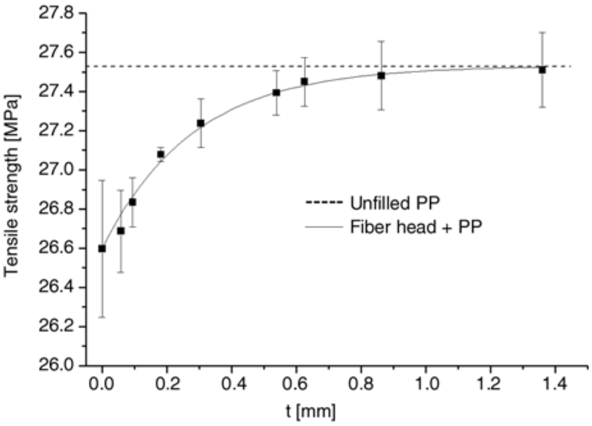

Figure 14. The influence of fiber heads on the tensile strength as a function of distance t from the theoretical failure cross section

A dotted horizontal line shows the tensile strength of the matrix in Figure 14. The measurement points approach the strength of pure PP (containing no additives) asymptotically as distance *t* increases. An exponential curve was fitted on the points, and its general equation is the following (31):

$$\sigma_c = \sigma_{c0} + A_1\left(1 - e^{-\frac{t}{t_1}}\right) \tag{31}$$

at $R = 0.990$ correlation factor, where: $\sigma_{c0} = 26.60$ MPa, $A_1 = 0.934$ MPa, $t_1 = 0.280$ mm, and t_1 is the constant of the exponential part.

Based on the above mentioned facts it could be stated that if the distance between the fracture cross section and the fiber head is larger than $(3–4)\cdot t_1 = 0.84 \ldots 1.12$, the fiber heads had no significant influence on the measured strength. The shape of the curve corresponds to the assumptions of the theoretical model (*r* radius vicinity of *B*). In case of 0.5 mm distance, the decrease in strength occurred more definitely. In case of 0 distance, the decrease in strength reached 0.92 MPa (3.34%). If the asymptotic character of the curve is neglected, and linear extrapolation is calculated from the first seven measurement points, then this influence ceases at $t = 0.62$ mm. For the sake of simplicity, this range was considered to be the r radius vicinity of cross section *B* in the model ($r = t_0 = 0.62$ mm). Accordingly, within this range the strength was handled as an average constant, as the half of the total difference ($\Delta\sigma$) (32):

$$\Delta\sigma = \sigma_m - \sigma_{fh} \tag{32}$$

where σ_m is the tensile strength of the PP without fiber heads, σ_{fh} is the tensile strength of PP containing one fiber head – in the effective vicinity of the tensile cross section.

Hence, if the effective spheres are handled as 100% defect sites, and are assumed to be exactly symmetrical to the plane of the failure cross section, A_{eff} introduced in (23) can be determined with the help of (33), (34) and (35). From A_{eff} the area of the meridian of the effective sphere (A_{fh}) can be determined simply based on (36).

$$\sigma_m = \frac{F_0}{A_0} \tag{33}$$

$$\sigma_{fh} = \frac{F_{fh}}{A_0} \tag{34}$$

$$\sigma_m = \frac{F_{fh}}{A_{eff}} \tag{35}$$

$$A_{eff} = A_0 - A_{fh} \tag{36}$$

where F_0 is the tensile strength of PP without fiber head, F_{fh} is the tensile strength of PP with one fiber head, while A_0 is the area of the failure cross section.

Knowing A_{fh}, the diameter (d) of the – supposedly circular – area can be determined:

$$d = \sqrt{\frac{4A_{fh}}{\pi}} \tag{37}$$

Knowing the diameter of the fiber heads used in the measurements, the value of a_e introduced in (8) can be determined (38) with the help of (37).

$$a_e = \frac{d}{d_{fiber\ head}} \tag{38}$$

Based on Figure 14, $\sigma_m = 27.52$ MPa and $\Delta\sigma = 0.46$ MPa, and considering that during the measurement $A_0 = 4.88$ mm^2, $d_{fiber\ head} = 223$ µm, the ratio between the diameter of the effective sphere and that of the equivalent spheres turned out to be $a_e = 1.81$.

Figure 15 reveals the influence of fiber head volume on the tensile strength.

The relation of fiber head volume and tensile strength is linear and can also be characterized by the general formula of (39):

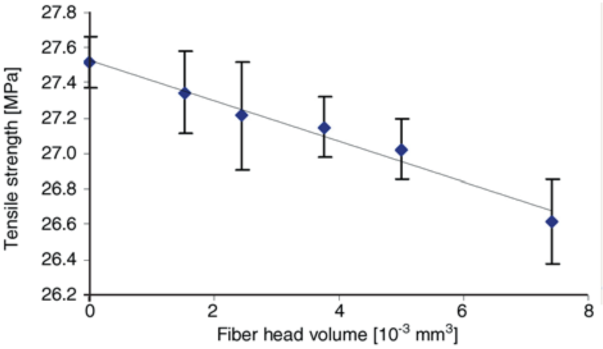

Figure 15. The influence of fiber head volume on the tensile strength

$$\sigma_c = a_c V_{fh} + b_c \tag{39}$$

at $R = 0.986$ correlation, where V_{fh} is the fiber head volume, $a_c = -11.6\cdot10^{-3}$ MPa/mm^3 and $b_c = 27.54$ MPa. Furthermore, the linear relation verifies the correctness of the method of considering the effective spheres based on the ratio of their volume (Equation (21)).

4.3. Application of the model

The test results obtained on composites produced by melt mixing were supplemented by measurements carried out on specimens produced in the same way but using basalt fibers containing fiber heads. Figure 16 shows the tensile strength of composites with and without fiber heads as a function of fiber content. A polynomial curve of the fifth order was fitted on the measurement points showed in Figure 16 [12]. Differences appear between the strength values in the fiber content interval between 8.5 and 20 vol%. In case of lower fiber contents, the effect of fiber head presence or absence is negligible. If the fiber content exceeds the upper value of the interval, the role of fiber heads is again less significant due to the discontinuities in the composite structure (the matrix does not fill the voids

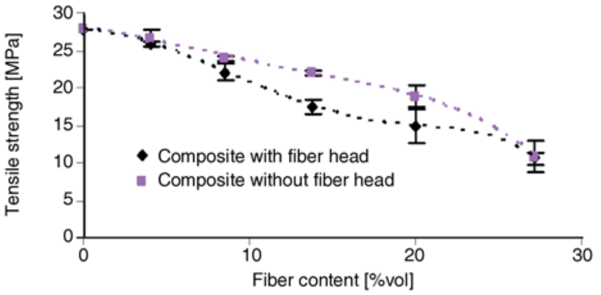

Figure 16. The influence of fiber heads on the tensile strength as a function of fiber content

among the fibers sufficiently). Hence the model was examined only in the middle range (8.5–20 vol%). The expected values of the composites containing fiber heads were calculated from the strength values of the coresponding material without fiber heads using the proposed model. The most important variable of the model is a_e, determined by finite element modeling and by investigating single fiber head composites. The aim of the finite element modeling was to obtain information on the size of the stress collection zones. If the stress collection zones exceeding the 0.92 MPa difference relative to the far vicinity of the fiber head are considered, $a_e = 1.67$ was obtained.

The Φ_{BV} values calculated from these results based on (21) provide the extent of strength reduction directly. The Φ_{BV} obtained in cases of different values (finite element modeling and tensile testing of PP specimens with single fiber head) are summarized in Table 4.

The results revealed in Table 4 are more illustrative in graphics. Hence the values measured in tensile tests on basalt fiber associated composites with and without fiber heads (Figure 16) and the results calculated based on the models are shown together in Figure 17.

Linear approximation was applied in the described stage. The uppermost line corresponds to composites without fiber heads, and the lowest one to the measured tensile strength of composites containing fiber heads. The line in the middle represents the calculations with the parameter values determined by finite element modeling. In this case the extent of strength reduction did not approach the real one.

Table 4. The values of Φ_{BV} as function of fiber content

Fiber content [vol%]	8.5	13.8	20.0
Φ_{BV} finite element ($a_e = 1.67$)	0.942	0.907	0.865
Φ_{BV} tensile ($a_e = 1.81$)	0.898	0.836	0.763

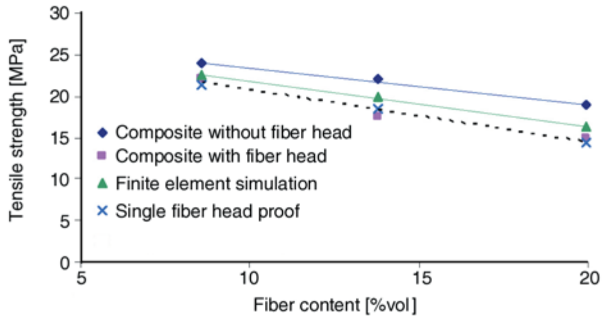

Figure 17. Comparison of the model and measured tensile strength values as a function fiber content

The reason is that although the model was developed further, in addition to interfacial processes relaxation phenomena could also take place, hence further refinement may be necessary to describe processes accurately.

The results obtained from single fiber head measurements correspond to the measurements carried out on composites with fiber heads. This is probably accidental, since the strength values of the composites with and without fiber heads deviate around the regression line in both directions and to different extents. Considering all the statements made, it was found that the model approximates the real processes well using parameter ae, hence the initial conditions and the principle turned out to be correct.

5. Conclusions

The influence of fiber heads, formed during the production of basalt fibers was studied in this article on the mechanical properties of composites. The fiber heads are of large size and number due to the characteristics of the technology. From the two main aspects related to the presence of these inclusions in the matrix, that is the improvement of toughness and defect site formation, the latter one turned out to be dominant. Firstly, the problem was analyzed by finite element simulations, in order to determine the intrinsic failure mode of the material. Afterwards, a theoretical model was created in characterizing the fiber head by an equivalent sphere, while its surroundings, the stress collection zone were described by another concentric sphere called effective sphere. The distribution of these effective spheres was described by a Poisson model. The main parameters of the model were determined with tensile tests on composites with a single fiber head embedded in PP. During these tests the influence of its size and the distance from the theoretical failure cross section on the tensile strength was analyzed. This way the effective cross section reduction, hence the role of fiber heads as volumetric defect sites in reducing the tensile strength were verified. The correctness of the model was verified by tensile tests made on composites made of basalt fibers with and without fiber heads.

Acknowledgements

This work was supported by the Hungarian Scientific Research Fund (T049069 and NI62729) and the Hungarian-Ukrainian Intergovernmental Science and Technology Program (TéT UKR-9/04). T. Czigány thanks the Öveges József Scholarship for the support of his personal research.

References

[1] Goldsworthy W. B.: New basalt fiber increases composite potential. Composites Technology, **8**, 15 (2000).

[2] Kurkov V., Labok V.: Fibres from stone. International Textile Bulletin, **49**, 48–52 (2003).

[3] Czigány T.: Basalt fiber reinforced hybrid polymer composites. Materials Science Forum, **473–474**, 59–66 (2005).

[4] Gur'ev V. V., Neproshin E. I., Mostovoi G. E.: The effect of basalt fibre production technology on mechanical properties of fibre. Glass and Ceramics, **58**, 24–27 (2001).

[5] Militky J., Kovacic V.: Influence of thermal treatment on tensile failure of basalt fibers. Engineering Fracture Mechanics, **69**, 1025–1033 (2002).

[6] Czigány T.: Special manufacturing and characteristics of basalt fiber reinforced polypropylene composites: Mechanical properties and acoustic emission study. Composites Science and Technology, **66**, 3210–3220 (2006).

[7] Czigány T., Pölöskei K., Karger-Kocsis J.: Fracture and failure behavior of basalt fiber mat-reinforced vinylester/epoxy hybrid resins as a function of resin composition and fiber surface treatment. Journal of Materials Science, **40**, 5609–5618 (2005).

[8] Thomason J. L.: The influence of fiber length and concentration on the properties of glass fiber reinforced polypropylene: 5. Injection moulded long and short fiber PP. Composites Part A, **33**, 1641–1652 (2002).

[9] Ségard E., Benmedahene S., Liksimi A., Lai D.: Influence of the fiber-matrix interface on the behaviour of polypropylene reinforced by short glass fiber above glass transition temperature. Composites Science and Technology, **62**, 2029–2036 (2002).

[10] Matkó Sz., Anna P., Marosi Gy., Szép A., Keszei S., Czigány T., Pölöskei K.: Use of reactive surfactants in basalt fiber reinforced polypropylene composites. Macromolecular Symposia, **202**, 255–267 (2003).

[11] Dmininghaus H.: Die Kunststoffe und ihre Eigenschaften. Springer-Verlag, Berlin (1998).

[12] Vas L. M., Balogh K.: Testing fiber orientation and its effect on glass mats by using image processing system. in 'Proceeding of VI. International Conference IMTEX'2000. Lodz, Poland', 69–78 (2000).

[13] Karlin S., Taylor H. M.: Stochastic Processes (in Hungarian). Gondolat Publisher, Budapest (1985).

[14] Vas L. M.: Statistical modeling of unidirectional fibrous structures. Macromolecular Symposia, **239**, 159–175 (2006).

[15] Vas L. M.: Strength of unidirectional short fibre structures as a function of fibre length. Journal of Composite Materials, **40**, 1695–1734 (2006).

[16] Vas L. M., Czigány T.: Strength modeling of two-component hybrid fiber composites in case of simultaneous fiber failures. Journal of Composite Materials, **40**, 1735–1762 (2006).

[17] Sachs L.: Applied statistics. Springer-Verlag, Berlin (1978).

[18] Szabó J. S., Czigány T.: Static fracture and failure behavior of aligned discontinuous mineral fiber reinforced polypropylene composites, Polymer Testing, **22**, 711–719 (2003).